COMPUTATIONAL MODELING OF COUPLED OXYGEN TRANSPORT AND MECHANICAL DEFORMATION IN TITANIUM STRUCTURES SUBJECTED TO EXTREME ENVIRONMENTS

By

Hao Yan

Dissertation

Submitted to the Faculty of the

Graduate School of Vanderbilt University

in partial fulfillment of the requirements

for the degree of

DOCTOR OF PHILOSOPHY

in

Civil Engineering

May, 2015

Nashville, Tennessee

Approved:

Caglar Oskay, Ph.D

Prodyot Basu, Ph.D

Ravindra Duddu, Ph.D

Ravi Penmetsa, Ph.D

James Wittig, Ph.D

For my mother Jing Chen and my father Zhicai Yan

ACKNOWLEDGMENTS

I would like to express my greatest gratitude to my advisor Dr. Caglar Oskay. Lacking of the background of computer modeling and programming, it would be impossible for me to accomplish the research without his help. The knowledge I have learned from him during my Ph.D study will be very beneficial in my life.

I would like to thank my Ph.D. committee members Dr. Prodyot Basu, Dr. Ravindra Duddu, Dr. Ravi Penmetsa and Dr. James Wittig, for their support, encouragement and advice.

I also want to thank my research group members Rudraprasad Bhattacharyya, Michael Bogdanor, Ruize Hu, Matthew Pike, Paul Sparks, Scott Williams, Shuhai Zhang and Xiang Zhang, for their help and friendship.

Most importantly, I would like to thank my wonderful parents for their eternal love and support.

Finally, I acknowledge the financial and technical support from the Air Force Research Laboratory, Structural Sciences Center (Contract No: GS04T09DBC0017 through High Performance Technologies, Inc.) and the Air Force Office of Scientific Research Multi-Scale Structural Mechanics and Prognosis Program (Grant No: FA9550-13-1-0104. Program Manager: Dr. David Stargel).

TABLE OF CONTENTS

Page

DEDICATION ii

ACKNOWLEDGMENTS iii

LIST OF TABLES vii

LIST OF FIGURES viii

1 INTRODUCTION 1

1.1 Motivation 1

1.2 Background 3

1.3 Research Objectives & Tasks 4

1.4 Material System 5

1.5 Dissertation Organization 6

2 A THREE-FIELD (DISPLACEMENT-PRESSURE-CONCENTRATION) FORMULATION FOR COUPLED TRANSPORT-DEFORMATION PROBLEMS . . . 8

2.1 Introduction 8

2.2 Problem Statement 10

2.2.1 Transport Model 10

2.2.2 Deformation Model 14

2.3 Finite Element Formulation 18

2.3.1 Weak forms 18

2.3.2 Discretization 22

2.3.3 Numerical implementation 24

2.3.3.1 Deformation model 25

2.4 Numerical Verification 29

2.5 Conclusion 37

3 A VISCOELASTIC-VISCOPLASTIC MODEL OF TITANIUM STRUCTURES SUBJECTED TO THERMO-CHEMO-MECHANICAL ENVIRONMENT 40
3.1 Introduction 40
3.2 Problem Statement 42
3.2.1 Deformation Model 43
3.2.2 Transport Model 50
3.3 Numerical Implementation of the Deformation Model 52
3.3.1 Recurrence formula for deviatoric stress tensor 53
3.3.2 Mixed FEM formulation of the viscoelastic-viscoplastic deformation model 55
3.4 Numerical Investigation of Ti-6242S Response in Combined Environment . . 60
3.4.1 Model calibration 61
3.4.2 Response under combined thermo-mechanical environment 64
3.4.2.1 Relaxation and oxygen ingress under high temperature exposure 69
3.4.2.2 Three-Point Bend Response of Exposed Specimens 71
3.5 Conclusion 76
4 MULTI-YIELD SURFACE MODELING OF VISCOPLASTIC MATERIALS . . 78
4.1 Introduction 78
4.2 Overview of multi-yield surface plasticity 80
4.3 Multi-yield surface viscoplasticity 84
4.4 Viscoelastic-viscoplastic model for cyclic deformation at high temperature . . 86
4.5 Numerical Implementation of the Multi-yield Surface Deformation Model . . 91
4.5.1 Mixed FEM formulation of the multi-yield surface deformation model . 92
4.5.2 Implementation algorithm of the multi-yield surface deformation model 98
4.6 Numerical Investigations 99
4.6.1 Multi-yield surface viscoplasticity verification 100
4.6.2 Cyclic response of Ti-6242S alloy 103

5 CONCLUSION AND FUTURE WORK 109
5.1 Conclusion 109
5.2 Future work 110
BIBLIOGRAPHY 112

LIST OF TABLES

Table Page

1.1 Chemistry of Ti-6Al-2Sn-4Zr-2Mo-0.1Si[1]. 6

2.1 Material parameters for viscoplastic deformation of Ti-6Al-2Sn-4Zr-2Mo-0.1Si. . . 29

2.2 Material parameters for oxygen transport in Ti-6Al-2Sn-4Zr-2Mo-0.1Si. 36

3.1 Material parameters for oxygen transport in Ti-6Al-2Sn-4Zr-2Mo-0.1Si. 61

3.2 Material parameters for viscoplastic deformation of Ti-6Al-2Sn-4Zr-2Mo-0.1Si. . . 62

3.3 Influence of oxidation on cracking at room temperature in 3-P bending. 71

LIST OF FIGURES

Figure Page

1.1 Aircraft operating at hypersonic speeds "reproduced from [2]". 2

1.2 Multi-physics process[3]. 3

1.3 Multiscale problem[3]. 4

1.4 Microstructure of Ti-6-2-4-2-S. 7

2.1 Coupled transport-deformation processes defined on the problem domain, Ω. . . . 11

2.2 The solution strategy for coupled transport and deformation problems. 25

2.3 Geometry, boundary conditions and the finite element mesh of the notched specimen. 30

2.4 The nodal positions in the mixed finite elements: (a) u4p4; (b) u4p1; (c) u9p4 and (d) u6p3. 31

2.5 Pressure distribution along the notch tip: $\theta = 0$. 32

2.6 Pressure distribution along the notch tip: $\theta = 70$. 33

2.7 The area of plastic deformation at applied displacement: (a) 4.32e^{-4}mm ; (b) 6.32e^{-4}mm computed using the u9p4 model. 33

2.8 The pressure field at applied displacement: (a) 4.32e^{-4}mm ; (b) 6.32e^{-4}mm computed using the u4p4 model. 33

2.9 The pressure distributions along the notch tip ($\theta = 0$ direction) computed using the u6p3 elements with element edge lengths of 2μm, 1μm and 0.5μm. 34

2.10 Pressure distribution along the notch tip: $\theta = 45$. 35

2.11 Concentration distribution along the notch tip: $\theta = 0$. 36

2.12 Normalized concentration distribution along the notch tip: $\theta = 0$ computed using the $P_e = 1.52 \times 10^{-4} \| p_{,i} \| h_e$. 38

2.13 Normalized concentration distribution along the notch tip: $\theta = 0$ computed using the $P_e = 1.52 \times 10^{-2} \| p_{,i} \| h_e$. 38

2.14 Normalized concentration distribution along the notch tip: $\theta = 0$ computed using the $P_e = 6.08 \times 10^{-2} \| p_{,i} \| h_e$. 39

3.1 Structural component subjected to coupled transport-deformation processes. . . . 43

3.2 One dimensional rheological representation of the viscoelastic-viscoplastic model. 44

3.3 The stress-strain response of Ti-6Al-2Sn-4Zr-2Mo-0.1Si at room and elevated temperatures. 63

3.4 The stress-strain response of Ti-6Al-2Sn-4Zr-2Mo-0.1Si with varying oxygen content at room temperature. 64

3.5 The stress-strain response of Ti-6Al-2Sn-4Zr-2Mo-0.1Si with varying oxygen content at 593 ^{0}C. 65

3.6 The stress relaxation test of Ti-6Al-2Sn-4Zr-2Mo-0.1Si at 593^{0}C and 650^{0}C for 40 seconds. 65

3.7 The stress relaxation test of Ti-6Al-2Sn-4Zr-2Mo-0.1Si at 593^{0}C for 100 hrs. . . . 66

3.8 The stress relaxation test of Ti-6Al-2Sn-4Zr-2Mo-0.1Si at 650^{0}C for 100 hrs. . . . 66

3.9 Coupled transport- deformation experiments procedure 67

3.10 Geometry, boundary condition and finite element mesh of the 4 point bend and the 3 point bend configurations. 67

3.11 Oxygen concentration along the depth from the tensile surface. 68

3.12 Equivalent stress variation in 4 point bending tests for 100 h at the center of the tensile surface. 69

3.13 Equivalent stress along the depth from the tensile surface: (a) 0.75 mm loading at 550^{0}C; (b) 0.75 mm loading at 450^{0}C; (c) 1.5 mm loading at 550^{0}C; and (d) 1.5 mm loading at 450^{0}C. 71

3.14 Equivalent stress contour of 4 point bending specimen at 550^0C with: (a) 1.50 mm midspan deflection at 0.03 hr; (b) 1.50 mm midspan deflection at 10 hrs; c) 1.50 mm midspan deflection at 2000 hrs; (d) 0.75 mm midspan deflection at 0.015 hr; (e) 0.75 mm midspan deflection at 10 hrs; f) 0.75 mm midspan deflection at 2000 hrs; 72

3.15 Three point bending damage at applied displacement of: (a) 2.4 mm; (b) 2.9 mm; c) 3.3 mm; (d) 3.7 mm of the specimen oxidized with 0.75 mm deflection at 450^0C. 72

3.16 Three point bending damage at applied displacement of 3.6 mm of the specimen oxidized at 550^0C with deflection: (a) 0.75 mm; (b) 1.50 mm. 74

3.17 3 point bending damage profile of the specimen oxidized at 450^0C along tensile surface at applied displacement of: (a) 1.4 mm; (b) 2.1 mm; (c) 3.7 mm; at 550^0C along tensile surface at applied displacement of (d) 1.35 mm; (e) 1.875 mm; (f) 2.475 mm. 75

4.1 Yield surfaces of multi-yield-surface J2 plasticity model in (a) deviatoric space; (b) principal space. 81

4.2 Mroz deviatoric hardening rule. 81

4.3 Inner yield surface translation process at (a) time t1; (b) time t2; (c) time t3; (d) time t4. 87

4.4 Stress relaxation test. 100

4.5 Time history input of stress tensor. 101

4.6 Yield surface translation process of no corrected translation direction at time (a) 0; (b) 40 s; (c) 72 s; of corrected translation direction at time (d) 0; (e) 40 s; (f) 72 s. . 102

4.7 Strain controlled low cycle fatigue test at 450 ^{0}C of (a) simulation and experiment strain input history comparison; (b) simulation and experiment stress history comparison; (c) simulation viscoplastic strainrate history; (d) simulation stress vs. strain and stress vs. plastic strain comparison. 104

4.8 Strain controlled low cycle fatigue test at 450 ^{0}C of simulation and experiment stress vs. strain comparison. 106

4.9 Strain controlled low cycle fatigue test at 550 ^{0}C of (a) simulation and experiment strain input history comparison; (b) simulation and experiment stress history comparison; (c) simulation viscoplastic strainrate history; (d) simulation stress vs. strain and stress vs. plastic strain comparison. 107

4.10 Strain controlled low cycle fatigue test at 550 ^{0}C of simulation and experiment stress vs. strain comparison. 108

Chapter 1

INTRODUCTION

1.1 Motivation

Structural systems operating in extreme thermo-mechanical conditions undergo significant deterioration induced by aggressive environmental agents. Numerous engineering problems display this environment effect, such as tritium ingress into concrete and steel in nuclear waste containment structures [4], calcium, sulfate and other aggressive agents ingress into concrete [5], moisture absorption of naval composites [6], and hydrogen diffuse into energy storage and transportation systems [7]. This dissertation focus on the environmental-mechanical response coupling observed in hypersonic aircraft applications: oxygen transport into titanium at high temperature environment [3]. In each of these application the environment-exposed material usually exhibits significantly weakened mechanical properties. In this dissertation, a multi-physics computational model was developed to simulate the coupled processes of oxygen ingress transport into a titanium alloy, as well as the mechanical response of the alloy at the high temperatures.

As the air vehicle operating at hypersonic speeds, a very thin layer of high temperature atmosphere is generated surrounding the surface of the aircraft, as shown in Fig. 1.1, within this hot region oxygen ingress into the surface of the structure in the form of diffusion, advection or reaction processes, causing the material to undergo changes in the material microstructure, including possible phase transformation, or elevated concentrations of oxygen within the substrate lattice [8, 9]. Experiments show that as the aircraft operates under the aerodynamic service loads, surface cracks are likely to initiate from the oxygen enriched zone, and act as potential sites for nucleation and growth of more microcracks and voids, eventually forming deep crack that fails the structure.

Figure 1.1: Aircraft operating at hypersonic speeds "reproduced from [2]".

The near α titanium alloy Ti-6Al-2Sn-4Zr-2Mo-0.1Si (Ti-6-2-4-2-S) is a candidate structural material for various components of concept hypersonic air vehicles [10] [11]. The material degradation process of Ti-6-2-4-2-S in the extreme environment associated with the hypersonic aircraft operational conditions involves complicated multiple physical processes, as depicted in Fig. 1.2. The temperature of oxygen abundant environment could be as high as 650^0C, which can significantly affect the mechanical performance of the material such as reducing the Young's modulus, increasing the ductility, plastic strain softening, reduction of viscosity. In contrast, oxygen ingress also is accelerated at high temperatures by increasing the diffusivity of the titanium alloy significantly and accelerating both the advection and reaction processes which also depend on diffusivity. The growing oxygen concentration results in strain hardening, embrittlement and loss of fatigue life, which plays the opposite effect upon the mechanical attributes; Furthermore mechanical damage, which is a manifestation of increasing crystalline defects, provides favorable conditions for further transport of oxygen.

In addition, phenomena that span multiple spatial scales contribute to the overall degradation in the mechanical response of the structure. During the operational environment, the aerodynamic mechanical loading and the thermal effects on the material are measured

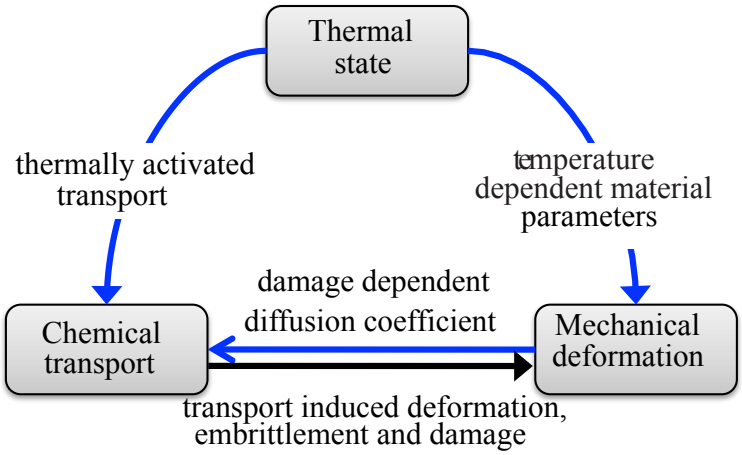

Figure 1.2: Multi-physics process[3].

in the scale of millimeters, whereas the oxygen ingress affected areas usually only have a thickness of several microns even after hundreds of hours of high temperature exposure, as illustrated in Fig. 1.3. This heterogeneity of the characteristic scales of different physical processes coupling with each other makes the response of the titanium structures subjected to thermo-chemo-mechanical loading and environmental conditions an extremely complicated problem to solve.

1.2 Background

Extensive research exists on experimental and modeling based investigations of oxygen ingress into titanium alloys (e.g., [12, 13, 14, 15]). The seminal work of Sofronis and McMeeking [16] provided the first finite element model for the coupled hydrogen transport - deformation response that can describe the hydrogen transport into a metal substrate around crack tips. This model has been extended to properly account for transport between trap and lattice sites by Krom *et al.* [17]. Oskay and Haney [3] proposed a coupled transport-deformation formulation to simulate the oxygen-induced embrittlement of titanium structures. Peters *et al.* [18] experimentally investigated the effect of mechanical loading on the oxygen transport rates and pointed to the effect of very significant relaxation that dominates the response under sustained deformations, which complicates the

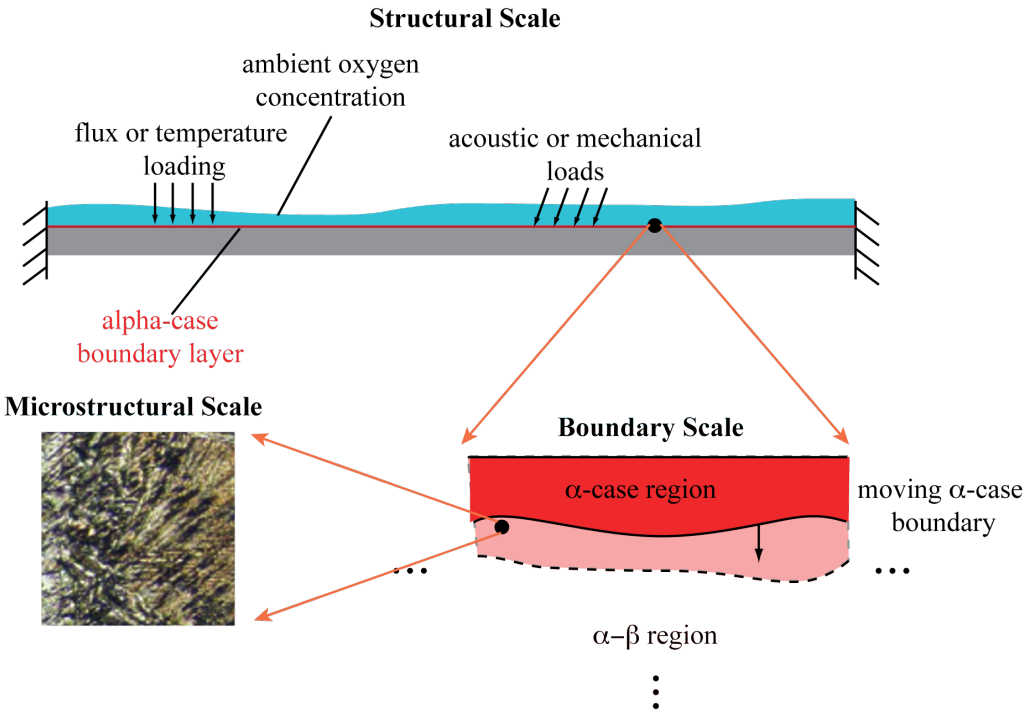

Figure 1.3: Multiscale problem[3].

coupling between the transport and mechanical processes. Parthasarathy *et al.* [19] proposed a fatigue life prediction methodology for oxygen exposed Titanium alloys subjected to uniaxial tension loads. Pilchak *et al.* [20] provided experimental and fractographic investigation of the effect of high temperature exposure of a near-α titanium alloy undergoing oxygen ingress. A comprehensive review of earlier diffusivity characterization of titanium and titanium alloys is provided by Liu and Welsch [21].

1.3 Research Objectives & Tasks

This dissertation presents a multiphysics multiscale methodology to simulate and predict the material failure mechanism of Ti-6-2-4-2-S in extreme conditions. In order to formulate a computational model to characterize and to predict the transport and deformation response of the titanium alloy Ti-6-2-4-2-S in extreme conditions, all three physical processes: the thermal state, the chemical transport and the mechanical deformation are

simulated individually. The key effort of the proposed model is to identify all the physical processes and their coupling mechanisms. More specifically, transport model is constructed and mixed finite element approach is implemented to enhance the coupling mechanism between oxygen transport and mechanical deformation processes. Viscoelastic-viscoplastic deformation model are formulated to realize the loss of ductility, viscoplastic stress hardening, stress relaxation and change of cyclic response in extreme temperature. The simulated results were calibrated and matched with the experiments, which makes this proposed model excellent in modeling the α case formation and mechanical response of titanium structure in its one unique way.

The primary research objective of this dissertation is to understand the transport and deformation process as well as their coupling mechanism of the titanium alloy Ti-6-2-4-2-S in extreme conditions associated with hypersonic flight. The following tasks were performed to achieve this research objective:

1. Establish and model the coupling mechanisms between the oxygen transport and mechanical deformation process.

2. Devise a mixed finite element model to accurately evaluate the coupled system of equations.

3. Exercise the proposed computational model along with available experimental data to understand the interaction between the deformation and environment-induced degradation.

4. Formulate, implement and verify a multi-yield surface viscoplastic model to capture the cyclic response in the high temperature environment.

1.4 Material System

Ti-6-2-4-2-S is lightweight, high in tensile strength and toughness, and has good corrosion and heat resistance. 0.1% β stabilizer silicon is added to improve the creep resistance and ductility of the material. The substrate chemical composition of Ti-6-2-4-2-S is shown

Table 1.1: Chemistry of Ti-6Al-2Sn-4Zr-2Mo-0.1Si[1].

	Si	Al	Sn	Zr	Mo	O	C	N	Fe	Y	Ti
Max weight%	0.13	6.5	2.2	4.4	2.2	0.15	0.08	0.05	0.1	0.005	
Min weight%	0.06	5.5	1.8	3.6	1.8	-	-	-	-	-	

in Table 1.1. Ti-6-2-4-2-S consists of two phases: brittle α phase and ductile β phase, which is HCP and BCC crystal structure respectively. α phase is stable up to the β transus temperature around 1000 ^{0}C; while β phase is more stable at temperature beyond 1000 ^{0}C. When exposed to temperature above 500 ^{0}C in oxygen enriched environment, Ti-6-2-4-2-S will generate an oxide layer on the top and a brittle oxygen enriched layer beneath it. It was found that the scales of the oxide and α case layer thickness are functions of temperature and exposure time. The formation and effect of the oxide layer of Ti-6-2-4-2-S is trivial compared to other titanium alloys, therefore only α case layer formation will be considered in this dissertation, as shown in Fig. 1.4. The white colored region of the polycrystal represent the α phase titanium, and the dark colored polycrystal is the β phase titanium.

Transport of oxygen into Ti-6-2-4-2-S usually takes place through vacancies and interstitial sites (lattice diffusion), as well as grain boundaries and dislocations (short-circuit diffusion)[22]. The transport of oxygen takes place through vacancy mechanism when an atom moves to another vacant lattice site. The interstitial diffusion involves transport of atoms from one interstitial position to another in the crystal lattice, which is more typical for diffusion of small atoms such as oxygen. The ingressed oxygen stabilize the HCP crystal structure of titanium by occupying the free interstitial lattice positions. Consequently, the material exhibits significantly different mechanical and chemical properties, including the reduction of ductility, increase of hardness and loss of fatigue life [18].

1.5 Dissertation Organization

The dissertation is organized to tackle each step listed in the research objectives. Steps 1, 2 and 3 were addressed by the construction of coupled transport and elasto-viscoplastic

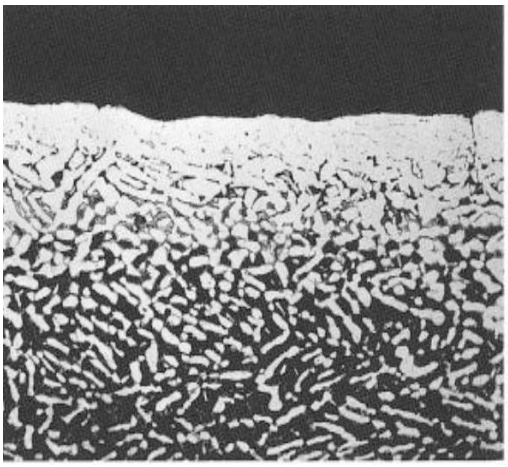

Figure 1.4: Microstructure of Ti-6-2-4-2-S.

mixed finite element model, as discussed in Chapter 2, where the transport model was proposed to incorporate the coupling variable of damage and pressure, followed by the stabilization of the reaction dominated flow. Finally the mixed finite element formulation of the deformation problem was established and the model was calibrated, validated and tested together with the stabilized transport model. The step 4 was tackled in Chapter 3, where the elasto-viscoplastic model was upgraded to include the viscoelastic property with the transport model inherited from Chapter 2 without modifications. The proposed multiphysics model was calibrated and the performance of the modified component was tested with a numerical example. In Chapter 4, a multi-yield surface viscoplastic model was proposed to capture the cyclic response characterization of alloys at high temperatures. The model is an extension of multi-yield surface plastic model; by incorporate the rate dependent effect on the back stress evolution and the Mroz collinearity rule of yield surface translation. At last, Chapter 5 provides the conclusion and future works.

Chapter 2

A THREE-FIELD (DISPLACEMENT-PRESSURE-CONCENTRATION) FORMULATION FOR COUPLED TRANSPORT-DEFORMATION PROBLEMS

2.1 Introduction

Aggressive environmental elements deteriorate the mechanical performance of material and structural systems subjected to combined loading and environmental conditions. Examples of engineering problems that display environmental-deformation response coupling are manifold. Two problems that have received significant attention, among others, are hydrogen- and oxygen-induced embrittlement in metals [8, 9].

Predictive computational modeling of the deformation response of such materials and structures subjected to aggressive environmental agents remains to be a significant challenge. The first difficulty is accurately modeling the coupling mechanisms between the inelastic deformation process and the mass transport of the aggressive agent into the structural material. The second difficulty is the development of a computational solution method to accurately evaluate the response in the presence of the coupling mechanisms. An extensive literature exists in characterization and modeling of metals subjected to hydrogen; and to a lesser extent, oxygen. The mass transport of the aggressive agent into the solid substrate is often modeled as a diffusion-advection-reaction problem [16], whereas the mechanical response involves inelastic deformations induced by the mechanical and thermal loads, as well as the environmental effects. Time-dependent deterioration of the mechanical properties is marked by the coupling between the transport process of the aggressive agent and the deformation under mechanical and thermal loads. The transport process typically results in volumetric expansion, hardening, embrittlement, loss of fatigue life and strength [23, 24]. On the other hand, the chemical potential that drives the kinetics of the aggressive agent

ingress is a function of the state of stress and deformation through formation of trap sites (e.g., dislocations) and microcracks that enhance the rate of mass transport.

Computational modeling of this phenomenon requires accurate capturing of the coupling effects between the transport and deformation mechanisms. Oskay and Haney [3] proposed a coupled transport-deformation formulation to simulate the oxygen-induced embrittlement of titanium structures. This formulation does not account for the advection-reaction terms that become significant at high stress gradient zones. The seminal work of Sofronis and McMeeking [16] provided the first finite element model for the coupled hydrogen transport - deformation response that can describe the hydrogen transport into a metal substrate around crack tips. This model has been extended to properly account for transport between trap and lattice sites by Krom *et al.* [17]. Ndong-Mefane *et al.* [25] addressed the potential instability problems in advection-dominated transport around crack and notch tips by employing a stabilized finite element approach. The advection coefficient, which depend on the pressure gradient, is typically approximated a-posteriori through discrete differentiation of the pressure estimates at the integration points in a displacement-based finite element solution of the deformation problem. This leads to significant approximation errors at regions of high stress gradients such as notch and crack tips.

In this chapter, a three-field computational model was proposed for the evaluation of coupled transport-deformation problems. The displacement, pressure and concentration fields are evaluated as independent unknowns. The key novel contribution of the present chapter is the demonstration that the mixed finite element method, in which the pressure is treated as an independent unknown in addition to the displacement degrees of freedom, can be employed to accurately compute the pressure gradient in the deformation problem. The pressure gradient information, in turn, is employed to accurately calculate the instantaneous coefficients of the advection-reaction terms of the mass transport problem. In addition, the computational model has the following properties: (a) the mass transport problem is stabilized to accurately describe the advection-dominated transport in the presence of high

stress gradients (e.g., crack and notch tips); (b) the deformation problem is evaluated using a tight-coupled two-field (displacement-pressure) formulation, whereas the transport and deformation processes are evaluated based on a staggered approach to efficiently address problems where the time scales associated with the transport and deformation processes are disparate.

The remainder of the chapter is organized as follows: Section 2.2 provides the mass transport model with diffusion-advection-reaction terms coupled to a viscoplasticity model. In Section 2.3, the finite element model of the coupled physics problems based on the three-field (displacement-pressure-concentration) modeling is described, including the stabilization of the mass transport problem for advection-dominated problems. The details of the implementation of the proposed approach is included. Numerical verification studies to assess the performance of the model in the context of the oxygen ingress problem in titanium alloys are discussed in Section 2.4.

2.2 Problem Statement

Consider the domain of an arbitrary solid body, $\Omega \subset \mathbb{R}^{n_{\text{sd}}}$, subjected to an aggressive agent along a part of the domain boundary, $\Gamma = \partial\Omega$, as illustrated in Fig. 2.1 (n_{sd}: number of space dimensions). When subjected to elevated boundary concentration, fluxes applied on the domain boundary or stress gradient fields, the aggressive agent tends to diffuse into the body. Concurrently, the solid body is subjected to time varying mechanical loading. In this section, the governing equations of the aggressive agent transport and deformation processes are provided, and the coupling mechanisms between the two physical processes are described.

2.2.1 Transport Model

I adopt Oriani's equilibrium theory to describe the diffusion of the aggressive agent into the stressed solid [26]. According to this theory, the driving force for diffusion is due to the

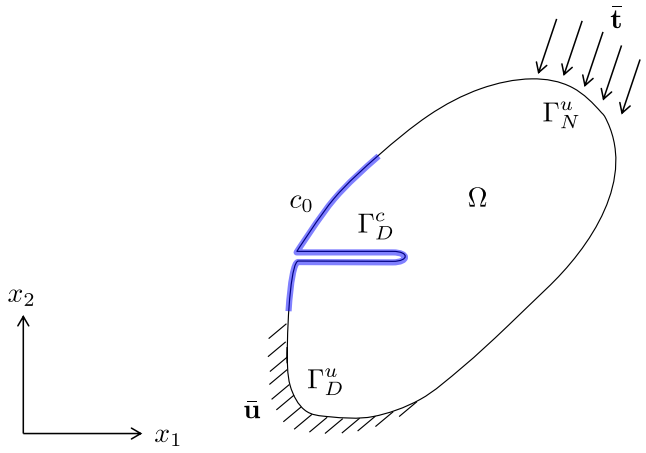

Figure 2.1: Coupled transport-deformation processes defined on the problem domain, Ω.

chemical potential of the aggressive agent:

$$q_i(\mathbf{x},t) = -\frac{D(T(\mathbf{x},t))}{RT(\mathbf{x},t)} c(\mathbf{x},t)\,\mu_{,i}(\mathbf{x},t) \tag{2.1}$$

in which, q_i denotes the components of the mass flux; D the diffusivity of the aggressive agent within the solid; T the temperature; R the universal gas constant; μ the chemical potential; and c the concentration of aggressive agent, given as weight ratio of the diffusing agent and the solid substrate within an infinitesimal control volume. I adopt the index notation in the problem formulation (i.e., $i = 1,...,n_{\text{sd}}$). Repeated indices of the spatial dimensions indicate summation unless otherwise stated. A subscript followed by a comma indicates partial derivative (i.e., $f_{,i} = \partial f/\partial x_i$). $\mathbf{x}$ and t parameterize the spatial and temporal dimensions, respectively. Bold symbol indicates vector notation (i.e., $\mathbf{x} = [x_1, x_2, x_3]$ for $n_{\text{sd}} = 3$). The chemical potential is a function of the concentration and the state of stress:

$$\mu(\mathbf{x},t) = \mu_0 + RT\ln(c) - \bar{V}_c p(\mathbf{x},t) \tag{2.2}$$

where, μ_0 denotes the chemical potential at the stress free state and at equilibrium concentration; $p = -\sigma_{ii}/3$ denotes the pressure; $\bar{V}_c$ the partial molar volume of the ingressed gas in the substrate solid; and σ_i the components of the stress tensor. Using Eqs. 2.1 and 2.2,

the transport equation of the stressed solid is given as:

$$\dot{c} - \left(Dc_{,i}\right)_{,i} - \left(\frac{Dc\bar{V}_c}{RT} p_{,i}\right)_{,i} = 0 \tag{2.3}$$

with superscribed dot indicates differentiation with respect to time. The initial and boundary conditions for the transport problem are expressed as:

$$c\left(\mathbf{x}, t=0\right) = c_\infty\left(\mathbf{x}\right); \qquad \mathbf{x} \in \Omega \tag{2.4}$$

$$c\left(\mathbf{x}, t\right) = c_0\left(\mathbf{x}, t\right); \qquad \mathbf{x} \in \Gamma_D^c \tag{2.5}$$

$$q_i n_i\left(\mathbf{x}, t\right) = 0; \qquad \mathbf{x} \in \Gamma_N^c \tag{2.6}$$

in which, c_∞ is the concentration of the aggressive agent at the natural state of the solid; c_0 the boundary concentration prescribed along $\Gamma_D^c \subset \Gamma$; $\Gamma_D^c \cap \Gamma_N^c = \emptyset$ and $\Gamma_D^c \cup \Gamma_N^c = \Gamma$; and, n_i the components of the unit normal vector. Only homogeneous type Neumann boundary condition is considered for simplicity of the ensuing formulation, but the formulation can be extended to arbitrary Neumann or Robin conditions.

The transport process is coupled to the mechanical deformation through two mechanisms. The first is the stress dependent chemical potential of the aggressive agent, which leads to the third term in the transport equation (Eq. 2.3). The second is by linking the diffusivity to the state of damage within the solid. The effect of microcracking and damage on diffusivity has been recognized in geological materials, concrete and metals (e.g., [27, 28, 29]). The diffusivity is assumed to be enhanced as a function of the defect density (e.g. microcrack) as proposed by Krajcinovic [29]. The effect of evolving defect density on diffusivity is modeled based on the percolation theory [3] as:

$$D\left(\omega, T\right) = D_0\left(1 + \mathscr{D}\left(\omega\right)\right) \exp\left(-\frac{Q}{RT}\right) \tag{2.7}$$

where, D_0 is the pre-exponential constant; Q is the activation energy; and, $\mathscr{D}\left(\omega\right)$ the effect

of mechanical damage on diffusivity:

$$\mathscr{D}(\omega) = \begin{cases} a\omega; & \omega < \omega_c \\ a\omega - \dfrac{(\omega - \omega_c)^2}{\omega - \omega_{ec}}; & \omega_c \leqslant \omega < \omega_{ec} \\ \infty; & \omega \geqslant \omega_{ec} \end{cases} \tag{2.8}$$

in which, $\omega \in [0,1)$ denotes the state of damage at a material point, with ω=0 indicating undamaged state of the material, and, ω=1 corresponds to loss of load carrying capacity at the material point. ω evolves as a function of mechanical loading as described below. ω_c and ω_{ec} denote the conduction and elastic percolation thresholds respectively; and, a is a material parameter.

In the absence of loading induced defect formation, Eq. 2.7 reduces to the classical Arrhenius form, where the diffusivity varies as a function of temperature only. At low levels of damage $(\omega < \omega_c)$, the diffusivity is linearly proportional to the damage variable [28]. When damage exceeds the elastic percolation threshold, a continuous path forms across the material point, permitting free flow of the aggressive agent. At intermediate values of the damage state, the rate of change of diffusivity progressively increases as a function of damage. The idea of using percolation thresholds to relate microcrack networks to transport properties in metals have been previously proposed [30]. In contrast, detailed experimental investigations of damage dependent change in diffusivity in metals has been relatively scarce. Additional experimental investigations would shed further light on the effect of this coupling mechanism.

When the body is subjected to a uniform stress field, the transport process (Eq. 2.3) reduces to the Fick's law of diffusion, and the state of mechanical deformation affects the diffusion of the aggressive agent through the damage dependent diffusivity only. In the presence of stress gradients induced by crack tips, notches and thermal gradients, pressure significantly affects transport.

2.2.2 Deformation Model

The governing equilibrium equations describing the mechanical response are:

$$\sigma_{ij,j}(\mathbf{x},t) + b_i(\mathbf{x},t) = 0 \tag{2.9}$$

where, b_i is the body force per unit volume. The constitutive response of the body is modeled in the rate form based on the assumption of additive split of the strain field:

$$\dot{\sigma}_{ij} = L_{ijkl}\dot{\varepsilon}^e_{kl}(\mathbf{x},t) = L_{ijkl}\left(\dot{\varepsilon}_{kl}(\mathbf{x},t) - \dot{\mu}_{kl}(\mathbf{x},t)\right) \tag{2.10}$$

in which, ε_{ij}, ε^e_{ij} and μ_{ij} denote the components of total, elastic and inelastic strain tensors, respectively. Assuming small strain kinematics:

$$\varepsilon_{ij} = \frac{1}{2}\left(u_{i,j}(\mathbf{x},t) + u_{j,i}(\mathbf{x},t)\right) \tag{2.11}$$

where, u_i denote the components of the displacement field. L_{ijkl} is the fourth order tensor of elastic moduli taken to be symmetric and strongly elliptic:

$$L_{ijkl} = L_{klij} = L_{jikl} = L_{ijlk} \tag{2.12}$$

$$\zeta_{ij}L_{ijkl}\zeta_{kl} \geq \eta\,\zeta_{ij}\zeta_{ij}; \quad \forall\zeta_{ij} = \zeta_{ji}; \quad \eta > 0 \tag{2.13}$$

The inelastic strains, μ_{ij}, is due to the viscoplastic deformation, as well as the lattice strains induced by elevated temperature and aggressive agent content within the lattice:

$$\mu_{ij} = \varepsilon^{vp}_{ij} + \varepsilon^T_{ij} + \varepsilon^c_{ij} \tag{2.14}$$

where, ε^{vp}_{ij} , ε^T_{ij} and ε^c_{ij} are the viscoplastic, thermal and concentration strains, respectively.

Thermal and concentration strains are taken to be volumetric:

$$\varepsilon_{ij}^{T} = \alpha\,(T - T_0)\,\delta_{ij} \tag{2.15}$$

$$\varepsilon_{ij}^{c} = \vartheta\,(c - c_\infty)\,\delta_{ij} \tag{2.16}$$

where, $\boldsymbol{\delta}$ is second order identity tensor; T_0 is the reference (i.e., room) temperature; α the thermal expansion coefficient; and, ϑ the concentration induced volumetric expansion coefficient. The viscoplastic strain is taken to remain in the deviatoric strain space $\left(\text{i.e.}, \varepsilon_{ii}^{vp} = 0\right)$.

Splitting the stress tensor into hydrostatic and deviatoric components and considering the constitutive equations yield:

$$\dot{p} = -\frac{1}{3}\dot{\sigma}_{ii} = -\frac{1}{3}L_{iikl}\left(\dot{\varepsilon}_{kl} - \dot{\mu}_{kl}\right) \tag{2.17}$$

$$\dot{s}_{ij} = \dot{\sigma}_{ij} + p\delta_{ij} = L'_{ijkl}\left(\dot{\varepsilon}_{kl} - \dot{\mu}_{kl}\right) \tag{2.18}$$

where,

$$L'_{ijkl} = L_{ijkl} - \frac{1}{3}L_{nnkl}\delta_{ij} \tag{2.19}$$

Remark: In this chapter, the focus is on the response of an isotropic solid. The tensor of elastic moduli then takes the form:

$$L_{ijkl} = k\delta_{ij}\delta_{kl} + 2G\left(\delta_{ik}\delta_{jl} - \frac{1}{3}\delta_{ij}\delta_{kl}\right) \tag{2.20}$$

where, k and G are bulk and shear moduli, respectively. The pressure is expressed as:

$$p = -ku_{i,i} + 3k\left[\alpha\,(T - T_0) + \vartheta\,(c - c_\infty)\right] \tag{2.21}$$

Equation (2.21) is provided in the total form, since the pressure is independent of viscous

and history-dependent effects. The deviatoric part of the elastic moduli is expressed as:

$$L'_{ijkl} = 2G\left(\delta_{ik}\delta_{jl} - \frac{1}{3}\delta_{ij}\delta_{kl}\right) \tag{2.22}$$

Applying the stress decomposition to the governing equation yields:

$$s_{ij,j}(\mathbf{x},t) - p_{,i}(\mathbf{x},t) + b_i(\mathbf{x},t) = 0 \tag{2.23}$$

The following boundary conditions are prescribed to evaluate the mechanical problem:

$$u_i(\mathbf{x},t) = \bar{u}_i(\mathbf{x},t) \qquad \mathbf{x} \in \Gamma_D^u \tag{2.24}$$

$$\sigma_{ij}n_j = \bar{t}_i(\mathbf{x},t) \qquad \mathbf{x} \in \Gamma_N^u \tag{2.25}$$

where, $\bar{u}_i$ is the prescribed displacement along the Dirichlet boundary Γ_D^u, $\bar{t}_i$ is the prescribed traction along the Neumann boundary Γ_N^u, such that $\Gamma_D^u \cap \Gamma_N^u = \emptyset$ and $\Gamma_D^u \cup \Gamma_N^u = \Gamma$.

The evolution of the viscoplastic strain is modeled by a generalization of the Johnson-Cook plasticity model. The viscoplastic model employed in this study accounts for the effects of embrittlement and hardening as a function of the aggressive agent concentration [3]. The flow of the viscoplastic strain is expressed in terms of a power law:

$$\dot{\varepsilon}_{ij}^{vp} = \gamma\left\langle\frac{f}{\sigma_Y}\right\rangle^q \frac{\partial f}{\partial \sigma_{ij}} \tag{2.26}$$

where, γ and q denote fluidity and viscoplastic hardening parameters, respectively; $\langle\cdot\rangle$ denotes Macaulay brackets (i.e., $\langle\cdot\rangle = ((\cdot) + |\cdot|)/2$); σ_Y the flow stress; and, $f(\boldsymbol{\sigma}, \sigma_Y)$ the yield function. The Von-Mises yield function is adopted in this study:

$$f\left(\sigma_{ij}, \sigma_Y\right) = \sqrt{3}\bar{s} - \sigma_Y \tag{2.27}$$

where, $\bar{s}$ is the second invariant of the deviatoric stress, $\mathbf{s}$. The generalized Johnson-Cook flow stress provides a functional relationship between yielding and the strain, temperature and concentration:

$$\sigma_Y = [A + B(\bar{\varepsilon}^{vp})^n + F(c - c_\infty)][1 - (T^\star)^m] \tag{2.28}$$

in which A, B, F, m and n are material parameters. The effective viscoplastic strain $\bar{\varepsilon}^{vp}$ and the non-dimensional temperature $T^\star$ are defined as:

$$\bar{\varepsilon}^{vp} = \sqrt{\frac{2}{3}\varepsilon_{ij}^{vp} : \varepsilon_{ij}^{vp}} \tag{2.29}$$

$$T^\star = \frac{T - T_0}{T_{\text{melt}} - T_0} \tag{2.30}$$

where, T_{melt} denotes melting temperature of the solid.

The damage progression within the material is modeled as a function of temperature and concentration. Let the damage parameter, ω, be the ratio between the equivalent strain, $\bar{\varepsilon}^{vp}$ and the failure strain, ε_f:

$$\omega = \frac{\bar{\varepsilon}^{vp}}{\varepsilon_f} \tag{2.31}$$

where, the failure strain is described as:

$$\varepsilon_f = D_1(c)(1 + D_5 T^\star) \tag{2.32}$$

in which, D_5 parameterizes the effect of temperature on the failure strain. D_1 varies as a function of concentration and idealize the progressive embrittlement due to aggressive

agent ingress:

$$D_1(c) = \begin{cases} D_1^{\infty} & \text{if} \quad c \leqslant c_{\infty} \\ \frac{1}{c_{\infty} - c_{\text{crit}}} \left(\left(D_1^{\infty} - D_1^{\alpha} \right) c + D_1^{\alpha} c_{\infty} - D_1^{\infty} c_{\text{crit}} \right) & \text{if} \quad c_{\infty} < c < c_{\text{crit}} \\ D_1^{\alpha} & \text{if} \quad c \geqslant c_{\text{crit}} \end{cases} \tag{2.33}$$

D_1^{∞} denotes the failure strain at room temperature in the absence of elevated concentration; D_1^{α} denotes failure strain beyond a critical concentration, c_{crit}; and the embrittlement is assumed to be linear at intermediate concentration values. The effect of aggressive agent ingress on the mechanical response is modeled based on the concentration dependent terms in Eq. 2.28 and Eq. 2.33. In Eq. 2.28, the flow stress is affected by the concentration. Elevated concentration tends to harden the material. In addition to hardening, the elevated concentration embrittles the response by reducing the failure strain in Eq. 2.32.

2.3 Finite Element Formulation

In this section, I provide the finite element formulation of the coupled transport and deformation problems. The formulation of the transport process includes the stabilization for the advection dominated flow, whereas the formulation of the deformation is conducted using a mixed (pressure-deformation) approach.

2.3.1 Weak forms

The governing equation of the aggressive agent transport is viewed as an advection-reaction-diffusion problem of the form:

$$\dot{c} - \left(D c_{,i} \right)_{,i} + \alpha_i c_{,i} + \beta c = 0 \tag{2.34}$$

in which, α_i and β are coefficients of advection and reaction, respectively:

$$\alpha_i = -\frac{D\bar{V}_c}{RT} p_{,i} \tag{2.35}$$

$$\beta = \left(\frac{D\bar{V}_c T_{,i}}{RT^2} - \frac{D_{,i}\bar{V}_c}{RT} \right) p_{,i} - \frac{D\bar{V}_c}{RT} p_{,ii} \tag{2.36}$$

It is well known that the numerical evaluation of the advection-reaction-diffusion problem using standard low-order finite elements leads to poor approximation and instability when the flow is dominated by advection or reaction. Considerable literature exists on stabilization approaches for this problem, as explained in [31] and references therein. In this study, I employ the Stabilized Finite Element Method (SFEM) proposed by Franca *et al.* [32] to eliminate potential instabilities. The transport response may be dominated by the advection term around notches and crack tips where high stress gradients are present. In contrast, the amplitude of the pressure Laplacian around the notch tips is typically smaller in magnitude. When the temperature and concentration gradients can be taken to be small (e.g., isothermal conditions and mild variation of diffusivity with respect to concentration), the reaction component is not dominant and stabilization is applied to the advection term only.

Let $v \in H_0^1(\Omega)$ be a test function; $H^1(\Omega)$ the Sobolev space of functions with square integrable values and derivatives defined on Ω; and, $H_0^1(\Omega)$ the subspace of functions in $H^1(\Omega)$ that are homogeneous along the domain boundary, Γ_D^c. The weak form of the transport problem is expressed as:

$$\int_\Omega v\dot{c}d\Omega + \int_\Omega v_{,i} D c_{,i} d\Omega + \int_\Omega v\alpha_i c_{,i} d\Omega + \int_\Omega v\beta c d\Omega = 0; \quad \forall v \in H_0^1(\Omega) \tag{2.37}$$

in which, the solution is sought within the solution space: $c \in \mathscr{W}$

$$\mathscr{W} := \left\{ \hat{c} \in H^1(\Omega) \mid \hat{c} = c_0 \text{ on } \mathbf{x} \in \Gamma_D^c \right\} \tag{2.38}$$

with sufficient continuity and smoothness assumed for the functions. Restricting the search for the solution within a finite dimensional subspace based on the Bubnov-Galerkin method, the stabilized finite element formulation is expressed as:

$$\int_\Omega v^h \dot{c}^h d\Omega + \int_\Omega v^h_{,i} D c^h_{,i} d\Omega + \int_\Omega v^h \alpha_i c^h_{,i} d\Omega + \int_\Omega v^h \beta c^h d\Omega \\ - \sum_{e=1}^{n_{el}} \left[\int_{\Omega_e} \left\{ \dot{c}^h - \left(D c^h_{,i} \right)_{,i} + \alpha_i c^h_{,i} \right\} \tau_e \left\{ - \left(D v^h_{,i} \right)_{,i} + \alpha_i v^h_{,i} \right\} d\Omega \right] = 0 \quad (2.39)$$

in which, $v^h \in \mathcal{V}^h \subset H^1_0(\Omega)$ and $c^h \in \mathcal{W}^h \subset \mathcal{W}$ are the test and trial functions belonging to the pertinent finite dimensional subspaces, Ω_e is the domain of the element, e, in a finite element discretization of the problem domain; n_{el} the total number of elements, and τ_e is a stability parameter which varies from element to element. At each element, τ_e is computed based on the following equations:

$$\tau_e = \frac{h_e^2}{\frac{2D}{m_e}\left[1 + \xi\left(P_e(x)\right)\right]} \quad (2.40)$$

$$P_e(x) = \frac{m_e ||\alpha||_p h_e}{D} \quad (2.41)$$

$$\xi(x) = \begin{cases} 1; & 0 \le x < 1 \\ x; & 1 \le x \end{cases} \quad (2.42)$$

where, m_e=1/3 and m_e=1/24 for linear and quadratic elements, respectively; h_e is the average nodal distance in element, e; and P_e the Peclet number. Substituting the coefficient of reaction and advection (Eqs. 2.35 and 2.36) into Eq. 2.39 yields:

$$\int_\Omega v^h \dot{c}^h d\Omega + \int_\Omega v^h_{,i} D c^h_{,i} d\Omega - \int_\Omega v^h \left[\frac{D\bar{V}_c}{RT} p_{,ii} + \left(\frac{D\bar{V}_c}{RT} \right)_{,i} p_{,i} \right] c^h d\Omega - \int_\Omega v^h \frac{D\bar{V}_c}{RT} p_{,i} c^h_{,i} d\Omega \\ - \sum_{e=1}^{n_{el}} \int_{\Omega_e} \left\{ \dot{c}^h - \left(D c^h_{,i} \right)_{,i} - \frac{D\bar{V}_c}{RT} p_{,i} c^h_{,i} \right\} \tau_e \left\{ - \left(D v^h_{,i} \right)_{,i} - \frac{D\bar{V}_c}{RT} p_{,i} v^h_{,i} \right\} d\Omega = 0 \quad (2.43)$$

In the current study, I employ first order (i.e., bilinear for 2-D and trilinear for 3-D)

finite elements to discretize the concentration field. The second derivative terms of the concentration field and the test functions in Eq. 2.43, therefore, vanish. I further assume that the intra-element variation in the coefficients remains small. The pressure field is evaluated as a solution to the deformation problem as defined below and itself is approximated using low-order finite elements. However, assuming vanishing of the term that involve the second derivatives of pressure leads to the partial loss of the reaction component, and the resulting formulation cannot adequately predict self-equilibration of concentrations induced by the pressure gradients. To alleviate this problem, I apply the divergence theorem to the pressure-dependent terms in Eq. 2.43:

$$\int_\Omega \nu^h \left[\frac{D\bar{V}_c}{RT} p_{,ii} + \left(\frac{D\bar{V}_c}{RT} \right)_{,i} p_{,i} \right] c^h d\Omega + \int_\Omega \nu^h \frac{D\bar{V}_c}{RT} p_{,i} c^h_{,i} d\Omega \\ = \int_{\Gamma^c_N} \nu^h \frac{D\bar{V}_c}{RT} p_{,i} c^h n_i d\Gamma - \int_\Omega \nu^h_{,i} \frac{D\bar{V}_c}{RT} p_{,i} c^h d\Omega \quad (2.44)$$

Substituting Eq. 2.44 to Eq. 2.43, the following weak form is obtained for the transport problem:

$$\int_\Omega \nu^h \dot{c}^h d\Omega + \int_\Omega \nu^h_{,i} D c^h_{,i} d\Omega + \int_\Omega \nu^h_{,i} \frac{D\bar{V}_c}{RT} p_{,i} c^h d\Omega - \int_{\Gamma^c_N} \nu^h \frac{D\bar{V}_c}{RT} p_{,i} c^h n_i d\Gamma \\ + \sum_{e=1}^{n_{el}} \left[\int_{\Omega_e} \nu^h_{,i} \left(\dot{c}^h - D_{,j} c^h_{,j} - \frac{D\bar{V}_c}{RT} p_{,j} c^h_{,j} \right) \tau_e \left(D_{,i} + \frac{D\bar{V}_c}{RT} p_{,i} \right) d\Omega \right] = 0 \quad (2.45)$$

The components of Eq. 2.43 that contains the concentration Laplacian is not included above since for low order finite elements, the concentration Laplacian vanishes. The evaluation of the transport problem clearly requires the computation of the pressure gradient fields. To provide consistent and accurate pressure distribution, the deformation problem is evaluated using a mixed formulation, where the cardinal unknowns are the displacements and the pressure. In this chapter, the formulation for the mixed finite element approach is presented for an isotropic solid.

Let v_i and q be the test functions for displacement and pressure in the appropriate

Sobolev spaces and with sufficient smoothness, and v_i^h and q^h belong to the corresponding finite dimensional subspaces of the test functions v_i and q, respectively. Starting from Eqs. 2.23 and 2.21, the weak form of the governing equations of equilibrium are: Find $\mathbf{u}^h \in \mathscr{H}^h \subset \mathscr{H}$ and $p^h \in \mathscr{P}^h \subset H^0(\Omega)$ such that for all $\boldsymbol{\nu}^h$ and q^h:

$$\int_\Omega \nu_{i,j}^h s_{ij} d\Omega - \int_\Omega \nu_{i,i}^h p d\Omega - \int_{\Gamma_N^u} \nu_i^h \bar{t}_i d\Gamma - \int_\Omega \nu_i^h b_i d\Omega = 0 \tag{2.46}$$

$$\int_\Omega \frac{1}{k} q^h p^h d\Omega + \int_\Omega q^h u_{i,i}^h d\Omega - \int_\Omega 3q^h [\alpha (T - T_0) + \vartheta (c - c_\infty)] d\Omega = 0 \tag{2.47}$$

in which,

$$\mathscr{H} := \left\{ \hat{\mathbf{u}} \in [H^1(\Omega)]^{n_{\text{sd}}} \mid \hat{\mathbf{u}} = \bar{\mathbf{u}} \text{ on } \mathbf{x} \in \Gamma_D^u \right\} \tag{2.48}$$

and, $H^0(\Omega)$ is the space of functions with square integrable values defined on Ω.

2.3.2 Discretization

Consider a Galerkin discretization of the concentration, displacement and pressure fields:

$$c^h(\mathbf{x},t) = \sum_{a=1}^{n_c} N_a^c(\mathbf{x}) \hat{c}_a(t) \tag{2.49}$$

$$u_i^h(\mathbf{x},t) = \sum_{a=1}^{n_u} N_a^u(\mathbf{x}) \hat{u}_{ai}(t) \tag{2.50}$$

$$p^h(\mathbf{x},t) = \sum_{a=1}^{n_p} N_a^p(\mathbf{x}) \hat{p}_a(t) \tag{2.51}$$

where N_a^c, N_a^u and N_a^p are the basis functions of the concentration, displacement and pressure fields, respectively; $\hat{(\cdot)}$ denotes the nodal coefficients of the corresponding field; and, the discretization of the test functions follow the Galerkin method. Substituting the concentration discretization (Eq. 2.49) into the weak form of the transport equation (i.e., Eq. 2.45),

yields:

$$F_b = \sum_{a=1}^{n_c} \left[\int_\Omega N_b^c N_a^c d\Omega \dot{\hat{c}}_a + \int_\Omega N_{b,i}^c D N_{a,i}^c d\Omega \hat{c}_a + \int_\Omega N_{b,i}^c \frac{D\bar{V}_c}{RT} N_a^c p_{,i} d\Omega \hat{c}_a - \right.$$
$$\int_{\Gamma_N^c} N_b^c \frac{D\bar{V}_c}{RT} N_a^c p_{,i} n_i d\Gamma \hat{c}_a + \sum_{e=1}^{n_{el}} \int_{\Omega_e} N_{b,i}^c \left(N_a^c \dot{\hat{c}}_a(t) - D_{,j} N_{a,j}^c \hat{c}_a - \frac{D\bar{V}_c}{RT} p_{,j} N_{a,j}^c \hat{c}_a \right) \times$$
$$\left. \times \tau_e \left(D_{,i} + \frac{D\bar{V}_c}{RT} p_{,i} \right) d\Omega \right] = 0; \quad b = 1, ..., n_c \quad (2.52)$$

in which, the pressure gradient term is approximated by the discretization of the pressure field:

$$p_{,i} = \sum_{a=1}^{n_p} N_{a,i}^p(\mathbf{x}) \hat{p}_a(t) \quad (2.53)$$

Substituting Eqs. 2.49 and 2.50 into Eqs. 2.46 and 2.47 respectively, the equilibrium equations yield:

$$\Psi_{bi} := \int_\Omega N_{b,j}^u s_{ij} d\Omega - \sum_{c=1}^{n_p} \int_\Omega N_{b,i}^u N_c^p d\Omega \hat{p}_c - \int_{\Gamma_N^u} N_b^u \bar{t}_i d\Gamma$$
$$- \int_\Omega N_b^u b_i d\Omega = 0; \quad b = 1, ..., n_u \text{ and } i = 1, .., n_{\text{sd}} \quad (2.54)$$

$$\Theta_c := \sum_{a=1}^{n_p} \int_\Omega \frac{1}{k} N_c^p N_a^p d\Omega \hat{p}_a + \sum_{b=1}^{n_u} \int_\Omega N_c^p N_{b,i}^u d\Omega \hat{u}_{bi}$$
$$- \int_\Omega 3 N_c^p [\alpha (T - T_0) + \vartheta (c - c_\infty)] d\Omega = 0; \quad c = 1, ..., n_p \quad (2.55)$$

where, the concentration field is computed using Eq. 2.49. Combining Eqs. 2.18 and 2.50 yields:

$$R_{ij} := \dot{s}_{ij} - L'_{ijkl} \left(\sum_{a=1}^{n_u} N_{a,l}^u \dot{\hat{u}}_{ak} \right) + 2G \dot{\varepsilon}_{ij}^{vp} = 0 \quad (2.56)$$

2.3.3 Numerical implementation

Equations 2.52, 2.54-2.56 constitute a coupled system of nonlinear equations, which are evaluated using the commercial computer program, Diffpack. Diffpack is an object oriented development framework with a library of C++ classes for solution of partial differential equations [33]. It is possible to solve this system of equations such that the unknown coefficients of concentration, displacement and pressure are evaluated simultaneously, or based on the staggered solution approach, in which the evolution of transport and deformation problems are evaluated separately but in a staggered manner. In this study, I consider the physical problems, where the characteristic time scales associated with the transport and mechanical processes are disparate. Typically, the ingress of the aggressive agent is a long-time phenomenon, whereas the mechanical loading is applied in a shorter time scale. Conversely, it is also of interest to investigate the transport response under constant amplitude loading, where the transport is regarded as the fast time scale phenomena. The staggered solution strategy (of isothermal type) is appropriate for such problems that involve disparate time scales, and is adopted in this study. The solution strategy is schematically illustrated in Fig. 2.2. A manager class controls the execution of the algorithm. At each time step, the mechanical and transport solver classes are invoked to solve the problems in turn until convergence is achieved between the solutions of both problems. The thermal state of the system is provided as an input to both transport and mechanical solvers. In the evaluation of the transport problem, the pressure and the pressure gradients are treated as known fields. The pressure and pressure gradients are computed in the deformation problem as described below. It is well known that the staggered solution algorithm is linearly convergent and unstable for systems with comparable characteristic times. In this study, the investigations are limited to temporally disparate problems only and no instabilities were observed. The transport problem is linear and the numerical implementation is standard. In the remainder of this section, the nonlinear solution procedure for the deformation problem is provided.

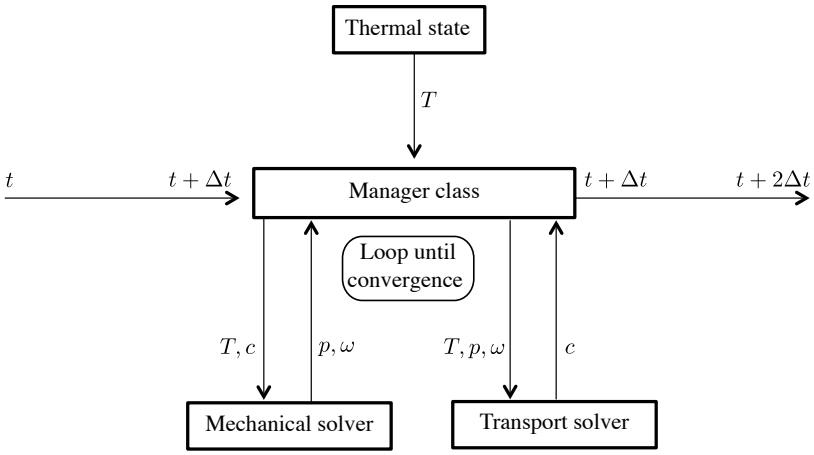

Figure 2.2: The solution strategy for coupled transport and deformation problems.

2.3.3.1 Deformation model

The deformation response is evaluated by simultaneously solving Eqs. 2.54-2.56. I start by discretizing the evolution equation of the deviatoric stress, which is an ordinary differential equation, using the θ-method:

$$R_{ij} = \Delta s_{ij} - L'_{ijkl}\left(\sum_{a=1}^{n_u} N^u_{a,l}\Delta\hat{u}_{ak}\right) + 2G_{t+\Delta t}\dot{\varepsilon}^{vp}_{ij}\theta\Delta t + 2G_t\dot{\varepsilon}^{vp}_{ij}(1-\theta)\Delta t = 0 \tag{2.57}$$

where $\Delta(\cdot)$=$_{t+\Delta t}(\cdot)$-$_t(\cdot)$, and $\theta \in [0,1)$ is an algorithmic parameter. θ=0, 0.5 and 1 correspond to forward Euler, midpoint and backward Euler algorithms, respectively. By employing the first order Taylor series expansion of Eqs. 2.54, 2.55 and 2.57 and using the Newton-Raphson method yields:

$$\begin{aligned} {}^{k+1}\Psi_{bi} &\approx {}^{k}\Psi_{bi} + {}^{k}\left(\frac{\partial\Psi_{bi}}{\partial s_{kl}}\right)^{k+1}\delta s_{kl} + \sum_{c=1}^{n_p}{}^{k}\left(\frac{\partial\Psi_{bi}}{\partial\hat{p}_c}\right)^{k+1}\delta\hat{p}_c \\ &= {}^{k}\Psi_{bi} + \int_\Omega N^u_{b,j}{}^{k+1}\delta s_{ij}d\Omega - \sum_{c=1}^{n_p}\int_\Omega N^u_{b,i}N^p_c d\Omega{}^{k+1}\delta\hat{p}_c = 0 \end{aligned} \tag{2.58}$$

$$
\begin{aligned}
{}^{k+1}\Theta_c &\approx {}^{k}\Theta_c + \sum_{b=1}^{n_u} {}^{k}\left(\frac{\partial \Theta_c}{\partial \hat{u}_{bk}}\right)^{k+1}\delta\hat{u}_{bk} + \sum_{a=1}^{n_p} {}^{k}\left(\frac{\partial \Theta_c}{\partial \hat{p}_a}\right)^{k+1}\delta\hat{p}_a \\
&= {}^{k}\Theta_c + \sum_{b=1}^{n_u}\int_\Omega N_c^p N_{b,i}^u d\Omega^{k+1}\delta\hat{u}_{bi} + \sum_{a=1}^{n_p}\int_\Omega \frac{1}{k} N_c^p N_a^p d\Omega^{k+1}\delta\hat{p}_a = 0
\end{aligned}
\tag{2.59}
$$

and,

$$
\begin{aligned}
{}^{k+1}R_{ij} &\approx {}^{k}R_{ij} + {}^{k}\left(\frac{\partial R_{ij}}{\partial s_{kl}}\right)^{k+1}\delta s_{kl} + \sum_{a=1}^{n_u} {}^{k}\left(\frac{\partial R_{ij}}{\partial \hat{u}_{ak}}\right)^{k+1}\delta\hat{u}_{ak} \\
&= {}^{k}R_{ij} - L'_{ijkl}\sum_{a=1}^{n_u} N_{a,l}^u {}^{k+1}\delta\hat{u}_{ak} + \left(I_{ijkl} + 2G\theta\Delta t\, {}^{k}C_{ijkl}\right)^{k+1}\delta s_{kl} = 0
\end{aligned}
\tag{2.60}
$$

in which,

$$
{}^{k}C_{ijkl} = {}^{k}\left(\frac{\partial \dot{\varepsilon}_{ij}^{vp}}{\partial s_{kl}}\right) \tag{2.61}
$$

The increment of deviatoric stress, ${}^{k+1}\delta s_{ij}$ is evaluated using Eq. 2.60 as:

$$
{}^{k+1}\delta s_{ij} = {}^{k}Q_{ijkl}\left(L'_{klmn}\sum_{a=1}^{n_u} N_{a,n}^u {}^{k+1}\delta\hat{u}_{am} - {}^{k}R_{kl}\right) \tag{2.62}
$$

where, the modulus ${}^{k}Q_{ijkl}$ is defined as:

$$
{}^{k}Q_{ijkl} = \left(I_{ijkl} + 2G\theta\Delta t\, {}^{k}C_{ijkl}\right)^{-1} \tag{2.63}
$$

Substituting Eq. 2.62 into Eqs. 2.58 and 2.59 yields:

$$
\begin{aligned}
\int_\Omega {}^{k}Q_{ijkl} N_{b,j}^u L'_{klmn}\sum_{a=1}^{n_u} N_{a,n}^u d\Omega^{k+1}\delta\hat{u}_{am} - \sum_{c=1}^{n_p}\int_\Omega N_{b,i}^u N_c^p d\Omega^{k+1}\delta\hat{p}_c \\
= \int_\Omega {}^{k}Q_{ijkl} N_{b,j}^u {}^{k}R_{kl} d\Omega - {}^{k}\Psi_{bi}
\end{aligned}
\tag{2.64}
$$

$$
-\sum_{b=1}^{n_u}\int_\Omega N_c^p N_{b,i}^u d\Omega^{k+1}\delta\hat{u}_{bi} - \sum_{a=1}^{n_p}\int_\Omega \frac{1}{k} N_c^p N_a^p d\Omega^{k+1}\delta\hat{p}_a = {}^{k}\Theta_c \tag{2.65}
$$

When expressed in the matrix form, Eqs. 2.64 and 2.65 yield:

$$\begin{bmatrix} {}^{k}\mathbf{K}^{uu} & \mathbf{K}^{up} \\ (\mathbf{K}^{up})^{T} & \mathbf{K}^{pp} \end{bmatrix} \begin{Bmatrix} {}^{k+1}\delta\hat{\mathbf{u}} \\ {}^{k+1}\delta\hat{\mathbf{p}} \end{Bmatrix} = \begin{Bmatrix} {}^{k}\mathbf{f}^{u} \\ {}^{k}\mathbf{f}^{p} \end{Bmatrix} \tag{2.66}$$

in which,

$$\begin{aligned} {}^{k}K^{uu}_{\alpha\beta} &= \int_{\Omega} N^{u}_{b,j}\, {}^{k}Q_{ijkl} L^{'}_{klmn} N^{u}_{a,n} d\Omega; \quad \alpha = b + (i-1)\, n_u; \;\; \beta = a + (m-1)\, n_u & (2.67)\\ K^{up}_{\alpha c} &= -\int_{\Omega} N^{u}_{b,i} N^{p}_{c} d\Omega; \quad \alpha = a + (i-1)\, n_u; \quad 1 \le c \le n_p & (2.68)\\ K^{pp}_{ab} &= -\int_{\Omega} \frac{1}{k} N^{p}_{a} N^{p}_{b} d\Omega; \quad 1 \le a, b \le n_p & (2.69) \end{aligned}$$

The force vectors are expressed as

$$\begin{aligned} {}^{k}\mathbf{f}^{u} &= \{{}^{k}f^{u}_{1}, ..., {}^{k}f^{u}_{n_{\mathrm{sd}} \times n_{\mathrm{u}}}\}^{T} & (2.70)\\ {}^{k}\mathbf{f}^{p} &= \{{}^{k}f^{p}_{1}, ..., {}^{k}f^{p}_{n_p}\}^{T} & (2.71) \end{aligned}$$

and the components of the force vector are given as:

$$\begin{aligned} {}^{k}f^{u}_{\alpha} &= \int_{\Omega} {}^{k}Q_{ijkl} N^{u}_{b,j}\, {}^{k}R_{kl} d\Omega - {}^{k}\Psi_{bi}; \quad \alpha = b + (i-1)\, n_u & (2.72)\\ {}^{k}f^{p}_{a} &= {}^{k}\Theta_{a}; \quad 1 \le a \le n_p & (2.73) \end{aligned}$$

Based on the definitions above, I employ the following algorithm to compute the pressure and displacement fields:

At $t = 0$, the initial condition of the viscoplastic strain rate is taken as zero, leading to a linear system of the form:

$$\begin{bmatrix} {}_{0}\mathbf{K}^{uu} & \mathbf{K}^{up} \\ (\mathbf{K}^{up})^{T} & \mathbf{K}^{pp} \end{bmatrix} \begin{Bmatrix} {}_{0}\hat{\mathbf{u}} \\ {}_{0}\hat{\mathbf{p}} \end{Bmatrix} = \begin{Bmatrix} {}_{0}\mathbf{f}^{u} \\ {}_{0}\mathbf{f}^{p} \end{Bmatrix} \tag{2.74}$$

where,

$$ {}_0K^{uu}_{\alpha\beta} = \int_\Omega N^u_{b,j} L'_{ijmn} N^u_{a,n} d\Omega \tag{2.75} $$

$$ {}_0f^u_\alpha = \int_{\Gamma^u_N} N^u_b \bar{t}_i d\Gamma + \int_\Omega N^u_b b_i d\Omega \tag{2.76} $$

$$ {}_0f^p_a = -\int_\Omega 3N^p_a [\alpha (T - T_0) + \vartheta (c - c_\infty)] d\Omega \tag{2.77} $$

The linear system (Eq. 2.74) is evaluated for the initial state of deformation and pressure coefficients.

At arbitrary time $t + \Delta t$; Given: ${}_t\hat{\mathbf{u}}$, ${}_t\hat{\mathbf{p}}$, ${}_t s_{ij}$ and ${}_t\dot{\varepsilon}^{vp}_{ij}$; Find: ${}_{t+\Delta t}\hat{\mathbf{u}}$, ${}_{t+\Delta t}\hat{\mathbf{p}}$.

1. Initiate the algorithm: $k = 0$.

2. Set the initial guesses of the pressure and deformation coefficients at the current increment:

$$ {}^0\hat{\mathbf{u}} = {}_t\hat{\mathbf{u}}; \quad {}^0\hat{\mathbf{p}} = {}_t\hat{\mathbf{p}}; \quad {}^0 s_{ij} = {}_t s_{ij}; \quad {}^0\dot{\varepsilon}^{vp}_{ij} = {}_t\dot{\varepsilon}^{vp}_{ij} \tag{2.78} $$

3. Loop until convergence:

   (a) Compute the moduli: ${}^k C_{ijkl}$, ${}^k Q_{ijkl}$ using Eqs. 2.61 and 2.63, respectively.

   (b) Calculate ${}^k\Psi_{bi}$, ${}^k R_{ij}$, ${}^k\Theta_b$ using Eqs. 2.54, 2.57 and 2.55, respectively.

   (c) Update the pressure and displacement increments, ${}^{k+1}\delta\hat{\mathbf{u}}$ and ${}^{k+1}\delta\hat{\mathbf{p}}$, using Eq. 2.66.

   (d) Compute deviatoric stress increment ${}^{k+1}\delta s_{ij}$ using Eq. 2.62.

   (e) Update displacement, pressure and stress:

$$ {}^{k+1}\hat{\mathbf{u}} = {}^{k+1}\delta\hat{\mathbf{u}} + {}^k\hat{\mathbf{u}} \tag{2.79} $$

$$ {}^{k+1}\hat{\mathbf{p}} = {}^{k+1}\delta\hat{\mathbf{p}} + {}^k\hat{\mathbf{p}} \tag{2.80} $$

$$ {}^{k+1}s_{ij} = {}^{k+1}\delta s_{ij} + {}^k s_{ij} \tag{2.81} $$

Table 2.1: Material parameters for viscoplastic deformation of Ti-6Al-2Sn-4Zr-2Mo-0.1Si.

ν	E_0 [GPa]	γ [MPa/s]	q	α [1/°C]	ϑ [1/%c]
0.32	120.8	25.0	1.0	7.7e-6	1.1e-3
A [MPa]	B [MPa]	F [MPa/%c]	n	m	c_{crit} [%]
895.0	125.0	140.0	0.2	0.85	4.5
T_{melt} [°C]	$\dot{\varepsilon}^0$ [1/s]	D_1^∞	D_1^α	D_5	
1700.0	1.0	0.1676	5.0e-3	3.0	

(f) Update ${}^{k+1}\dot{\varepsilon}_{ij}^{vp}$ and ${}^{k+1}\varepsilon_{ij}^{vp}$ by simultaneously evaluating:

$$ {}^{k+1}\varepsilon_{ij}^{vp} = {}_t\varepsilon_{ij}^{vp} + \theta\Delta t\, {}^{k+1}\dot{\varepsilon}_{ij}^{vp} + (1-\theta)\Delta t\, {}_t\dot{\varepsilon}_{ij}^{vp} \tag{2.82} $$

$$ {}^{k+1}\dot{\varepsilon}_{ij}^{vp} = \gamma \left\langle \frac{{}^{k+1}f}{{}^{k+1}\sigma_Y} \right\rangle^{q\ k+1} \left(\frac{\partial f}{\partial \sigma_{ij}} \right) \tag{2.83} $$

(g) $k = k+1$

2.4 Numerical Verification

In this section, the performance of the proposed three-field model is verified using numerical simulations. The effect of element type on the accuracy and stability characteristics of the transport and deformation problems based on numerical simulations is investigated.

I am concerned with the response of a near alpha titanium alloy, Ti-6Al-2Sn-4Zr-2Mo-0.1Si (Ti-6242S), which displays good mechanical properties at high temperatures. When exposed to high temperatures for an extended period of time, this alloy is known to exhibit significant embrittlement [24] caused by ingress of oxygen. The material properties that characterize the mechanical response at a wide range of temperatures and oxygen exposure are summarized in Table 2.1. Figure 2.3 illustrates the geometry and discretization of the numerical specimen. The specimen dimensions are 0.8mm x 0.4mm with a 0.4mm deep notch at the middle. The notch radius is 20μm. Due to symmetry, only a quarter of the specimen is discretized (with 1846 quadrilateral elements or 3298 triangular elements). The

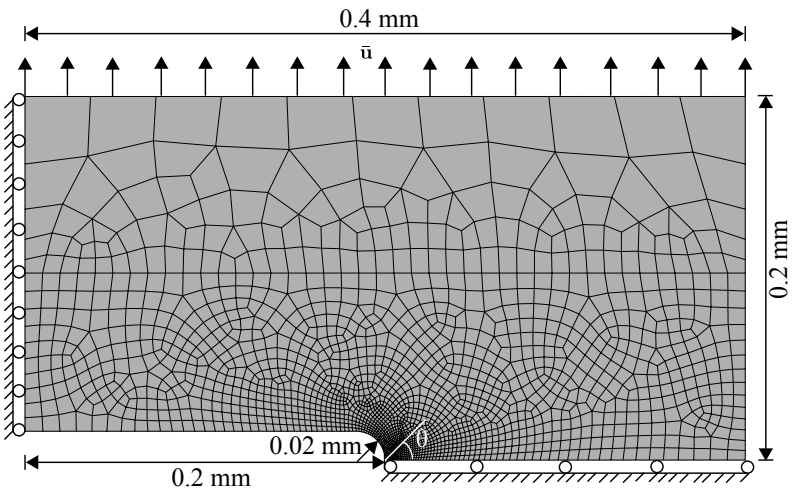

Figure 2.3: Geometry, boundary conditions and the finite element mesh of the notched specimen.

notched specimen is employed to generate a stress gradient, which captures the effects of advection and reaction terms in the transport model. Plane strain conditions are assumed.

The specimen is discretized using four types of elements, named as u4p4, u4p1, u6p3 and u9p4. The types of elements and the associated nodal positions are shown in Fig. 2.4. u4p4 consists of four-noded Lagrangian quadrilateral elements for both displacement and pressure degrees of freedom. In u4p1, the pressure is discretized using a single node positioned at the centroid of the finite element, whereas the displacement is discretized using four-node quadrilateral elements. Two types of Taylor-Hood elements were employed. u6p3 consists of a triangular, quadratic, six-node element for displacement degrees of freedom, and a three-node, linear element for pressure degrees of freedom. u9p4 consists of a quadrilateral, bi-quadratic, nine-node Lagrangian element for displacement degrees of freedom, whereas a four-node bi-linear element is employed for pressure degrees of freedom. In u4p4, u6p3 and u9p4 elements, the pressure field exhibits inter-element continuity, allowing a straightforward computation of the pressure gradients (i.e., using Eq. 2.53). In all four element types, the displacement discretization is isoparametric, whereas pressure field is non-isoparametric. The performance of the four mixed elements are compared to the reference model (denoted as u4), which is the standard displacement-based finite el-

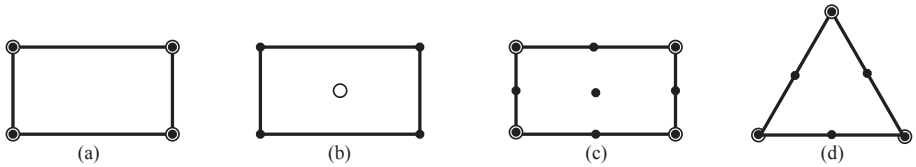

Figure 2.4: The nodal positions in the mixed finite elements: (a) u4p4; (b) u4p1; (c) u9p4 and (d) u6p3.

ement with four-noded bi-linear shape functions. In u4, the pressure is evaluated at the integration points.

In the case of u4p1 element, the pressure is constant within a finite element, and Eq. 2.53 cannot be used to directly compute the pressure gradients. The computation of the pressure gradient for u4p1 is based on the pressure smoothing procedure of the least squares type [34]. In this procedure, a piecewise continuous smoothed pressure field is computed. The smoothed pressure approximation is made as a function of four-noded bi-linear Lagrangian quadrilateral shape functions. The pressure gradient is then computed using Eq. 2.53 from the smoothed pressure field.

The specimen is subjected to displacement controlled tensile loading with maximum amplitude of $6.4e^{-4}$ mm applied in 11.52 seconds at 650°C and the mechanical response is evaluated using the four mixed elements described above. Figures 2.5 and 2.6 display the pressure as a function of distance from the notch tip plotted along lines 0° and 70° to the horizontal, respectively. The pressure profiles at the loading magnitudes of $4.32e^{-4}$ mm and $6.32e^{-4}$ mm are shown. At both loading amplitudes a zone of plastic deformation forms around the notch tip as shown in Fig. 2.7. The peak pressure moves away from the notch tip as the loading increases due to accumulation of damage and expansion of the area of the plastic zone. All four models yield similar response at low loading amplitude, but the results begin to deviate as the loading increases. u4p4 displays slight oscillation around the peak pressure (Fig. 2.6), whereas u4p1, u6p3 and u9p4 elements yield response free of oscillations. The pressure predictions of u4p1, u6p3 and u9p4 are stable everywhere inside the problem domain and in reasonable agreement throughout the loading history. For

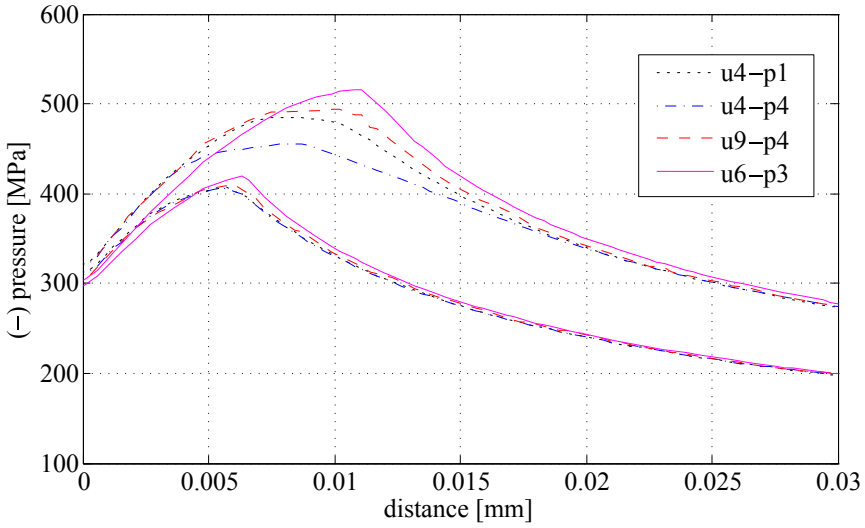

Figure 2.5: Pressure distribution along the notch tip: $\theta = 0$.

u4p4 element, the pressure oscillations are observed within part of the specimen domain and it is severe along the 70° to the horizontal. Figure 2.8 shows the oscillating pressure distribution around the notch tip at the loading magnitudes of $4.32e^{-4}$ mm and $6.32e^{-4}$ mm. The oscillatory behavior of the u4p4 element is expected as this element does not satisfy the Babuska-Brezzi stability criteria and therefore not guaranteed to be stable.

The convergence characteristics of the mixed formulation are investigated in a mesh sensitivity study. The mesh sensitivity study was performed using the u6p3 elements. The pressure variations around the notch tip at $\Theta = 0$ orientation computed using three different mesh densities are shown in Fig. 2.9. The results correspond to the applied magnitudes of $4.32e^{-4}$ mm (lower curves) and $6.32e^{-4}$ mm (upper curves). In the three discretizations considered, the element edge lengths around the crack tip were set to $h = 2$ μm, 1μm and 0.5μm, respectively. All three mesh densities produce very similar pressure profiles. The pressure profiles computed using the $h = 0.5$ μm and 1μm edge lengths are nearly identical, pointing to mesh convergence.

The key benefit of employing the mixed finite element approach in computing the coupled aggressive agent ingress and deformation response is to accurately capture the pressure gradients across the problem domain. The pressure gradient fields are in turn employed in

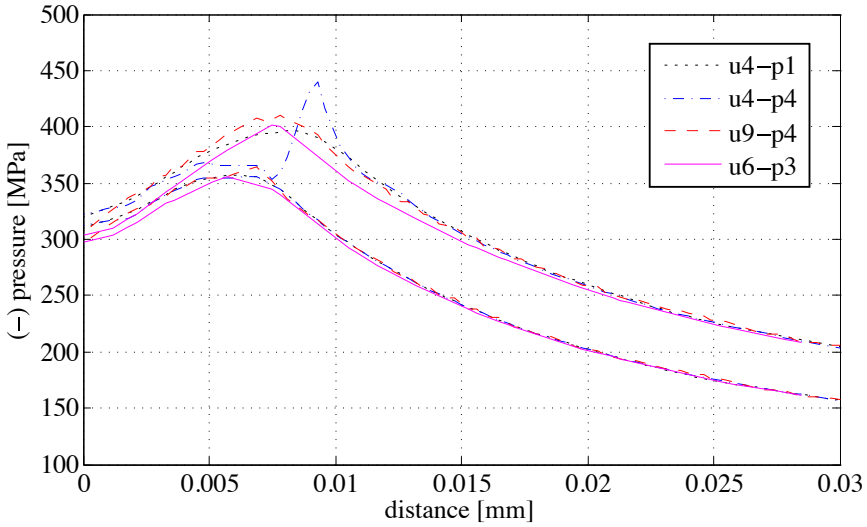

Figure 2.6: Pressure distribution along the notch tip: $\theta = 70$.

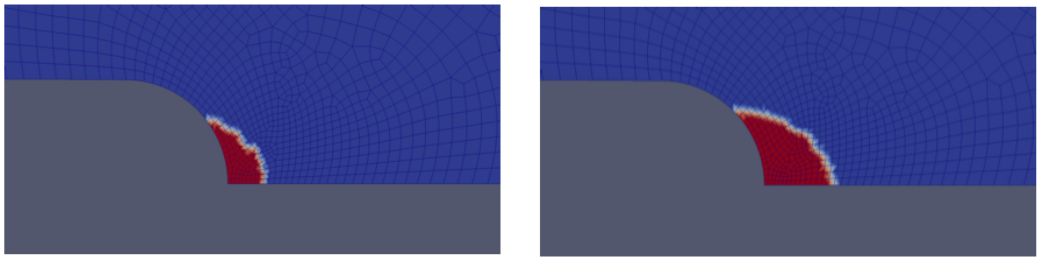

(a) (b)

Figure 2.7: The area of plastic deformation at applied displacement: (a) 4.32e^{-4}mm ; (b) 6.32e^{-4}mm computed using the u9p4 model.

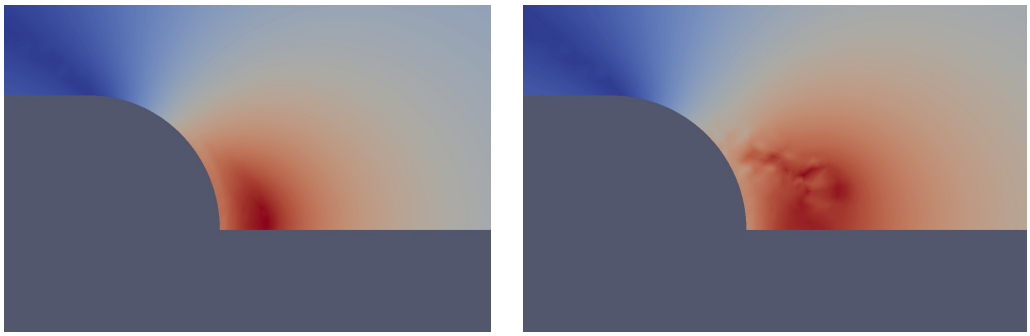

(a) (b)

Figure 2.8: The pressure field at applied displacement: (a) 4.32e^{-4}mm ; (b) 6.32e^{-4}mm computed using the u4p4 model.

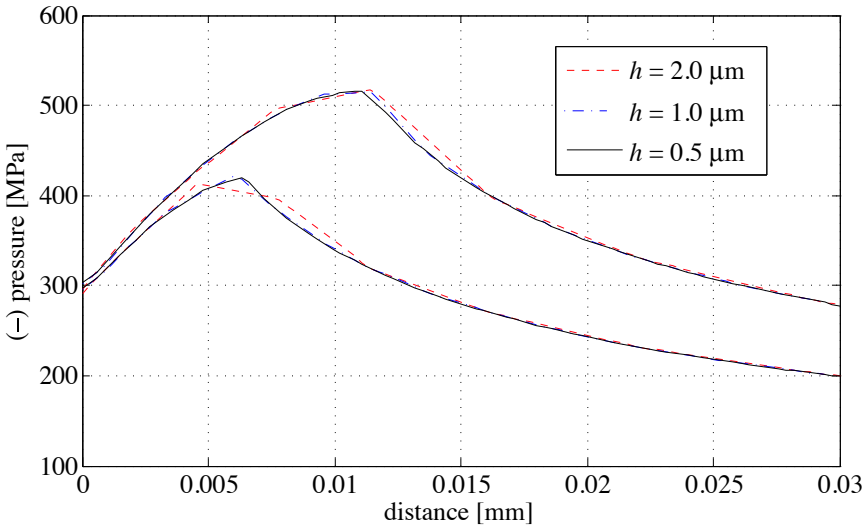

Figure 2.9: The pressure distributions along the notch tip ($\theta = 0$ direction) computed using the u6p3 elements with element edge lengths of 2μm, 1μm and 0.5μm.

accurately capturing the transport response. This is in contrast to the displacement-based finite element method, in which the stresses are computed point-wise at the integration points and must be approximated to extract the pressure gradient fields. It is convenient and accurate to use the mixed approach since the pressure is available as a continuous field. Additionally, the mixed finite element method addresses the well-known numerical issues related to incompressible materials and incompressible flow within the plastic deformation process. Figure 2.10 shows the pressure distributions as a function of distance from the notch tip plotted along the direction 45° to the horizontal at loading magnitudes of $1.84e^{-4}$ mm, $4.32e^{-4}$ mm and $6.32e^{-4}$ mm, respectively. The pressure distributions computed using the u9p4 and u4 models are compared. The pressure profile of the u4 model is obtained by interpolating the point-wise pressure values at the integration and smoothing the interpolated response. When the applied loading is low and the accumulated plastic strains are small, the pressure distributions from the displacement-based and mixed formulations are very similar. At higher loading amplitudes, significant discrepancy is observed between the mixed and displacement-based formulations close to the notch tip. The mixed formulation also results in a relatively smooth pressure field as a function of distance from

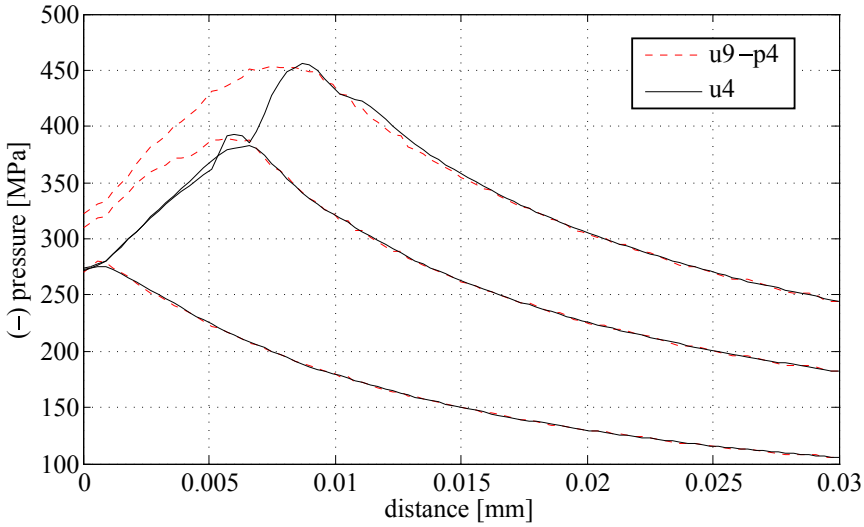

Figure 2.10: Pressure distribution along the notch tip: $\theta = 45$.

the notch tip compared to the displacement-based formulation, which displayed some oscillations. Away from the notch tip, where the pressure gradients are low, the pressure plots from the mixed- and displacement-based formulations are very similar.

Next, the performance of the proposed stabilized transport model is investigated in the context of a mechanical pressure dependent oxygen transport problem. The numerical specimen is heated to a uniform temperature of 650°C and kept at this constant temperature level for the duration of 420 hours. The time step size employed in the simulations below is set to 1 hour. The nonuniform pressure field computed in the example above is employed in the simulations. The pressure field is taken to be time-invariant throughout the duration of the simulation. While, stress relaxation would likely occur at such high temperatures, the pressure field is set as constant (but spatially non-uniform) to assess the performance of the transport model in the presence of significant pressure gradient fields. The transport properties that control the oxygen ingress process into the titanium alloy are summarized in Table 2.2. The diffusivity is taken to be independent of concentration magnitude. In the transport simulations, no external boundary concentrations or boundary fluxes are imposed, and the transport is taken to be due to pressure gradient induced internal advection only. The pressure induced oxygen transport within the specimen is observed for the duration of

Table 2.2: Material parameters for oxygen transport in Ti-6Al-2Sn-4Zr-2Mo-0.1Si.

D_0 [mm^2/sec]	c_∞ [%]	Q [KJ/mole]	ω_c	ω_{ec}	a	$\bar{V}_O$ [cm^3/mole]
5.39	0.15	184.0	0.1	0.7	3.56	3.5

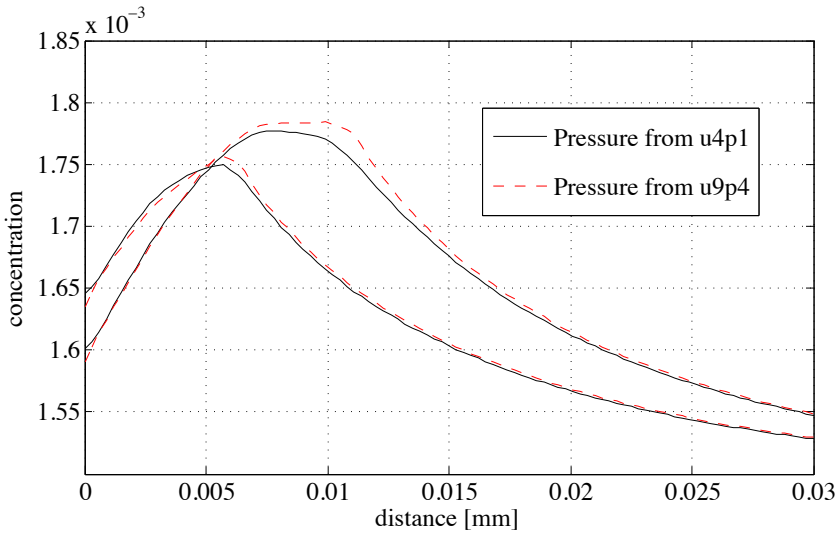

Figure 2.11: Concentration distribution along the notch tip: $\theta = 0$.

high temperature exposure. The transport problem is discretized using four-node bi-linear elements for concentration degrees of freedom. Figure 2.11 displays the oxygen concentration profiles obtained by the transport model plotted as a function of distance from the notch tip along the horizontal line (i.e., $\theta = 0$). The two plots compare the concentration profiles computed using the pressures from u4p1 and u4p9 deformation models. Elevated pressures lead to increased advection flow of oxygen and higher oxygen concentrations. The concentration profiles computed using the pressures from u4p1 and u9p4 models are close to each other and computation of the pressure fields using both models provide reasonable approximations.

In order to verify the stabilization scheme employed in the transport model, a parametric study is performed by varying the Peclet number of the transport equation. The Peclet number (i.e., Eq. 2.41) controls the contribution of the advection component of the transport with respect to the diffusion component. At high Peclet numbers, unstabilized transport models exhibit instability and inaccuracy. For all simulations in the parametric study, the

pressure profile computed using the u9p4 deformation model is employed. Figures 2.12-2.14 compares the oxygen concentration fields generated using the stabilized and unstabilized transport models. The normalized concentration fields are plotted along the horizontal line ($\theta = 0$) from the notch tip. Figures 2.12, 2.13 and 2.14 shows simulations conducted using the value of the Peclet numbers of $P_e = 1.52 \times 10^{-4} \| p_{,i} \| h_e$; $1.52 \times 10^{-2} \| p_{,i} \| h_e$ and $6.08 \times 10^{-2} \| p_{,i} \| h_e$; respectively, the former computed by the material parameters shown in Table 2.2. The exact value of the Peclet number varies as a function of the pressure gradient as well as the characteristic size of the element. The Peclet numbers are achieved by varying the coefficient of advection, α. When the original Peclet number is employed, the stabilized and the unstabilized simulations coincide, indicating that the transport is diffusion dominated. For increased values of the Peclet numbers, the unstabilized model exhibits significant errors. When the Peclet number is equal to $1.52 \times 10^{-2} \| p_{,i} \| h_e$, significant deviations in the concentration values between the stabilized and unstabilized simulations are observed. When the Peclet number is set to $6.08 \times 10^{-2} \| p_{,i} \| h_e$, severe oscillations are generated by the unstabilized model with negative concentration values. In all cases considered, the stabilized model displays concentration distribution free of oscillations around the notch tip. The present parametric study artificially varied the Peclet number to investigate the stability of the proposed transport model and instability was only observed when the Peclet number is set to a higher than the original value. There exists a significant variability in the transport parameters measured even in a single alloy type [21], which contributes to wide variations in the Peclet numbers. In addition, the presence of high thermal gradients and cracks may also lead to high advection coefficients and high Peclet number transport.

2.5 Conclusion

This chapter provided a three-field computational model for coupled transport-deformation problems. The proposed model is based on a tightly coupled two-field formulation for the viscoplastic deformation response to provide accurate pressure and pressure gradient fields

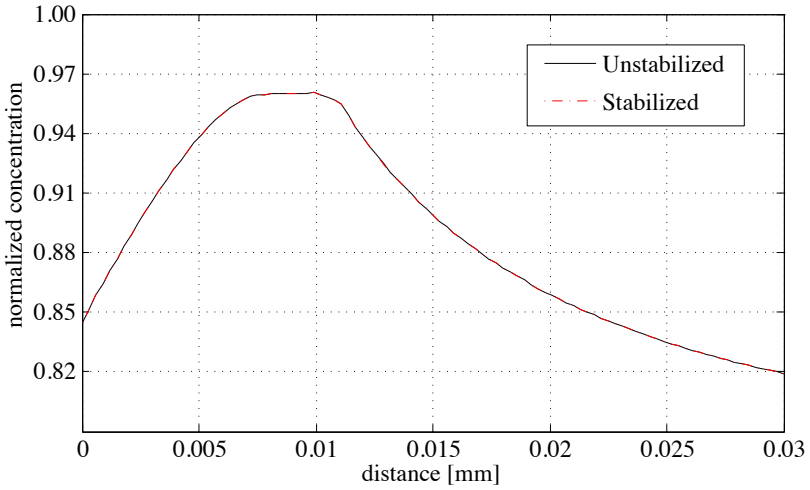

Figure 2.12: Normalized concentration distribution along the notch tip: $\theta = 0$ computed using the $P_e = 1.52 \times 10^{-4} \|p_{,i}\| h_e$.

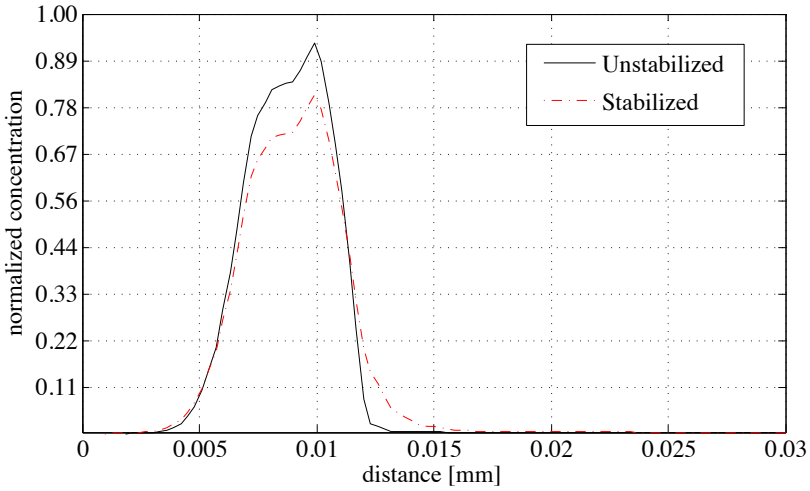

Figure 2.13: Normalized concentration distribution along the notch tip: $\theta = 0$ computed using the $P_e = 1.52 \times 10^{-2} \|p_{,i}\| h_e$.

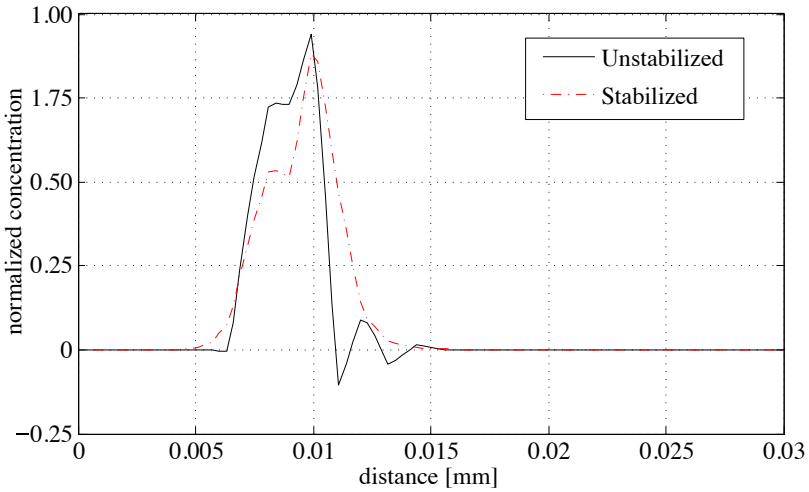

Figure 2.14: Normalized concentration distribution along the notch tip: $\theta = 0$ computed using the $P_e = 6.08 \times 10^{-2} \|p_{,i}\| h_e$.

to a transport problem. It is demonstrated that modeling the transport processes at the high stress gradient zones such as around notch tips requires accurately approximating the pressure and pressure gradient fields. The proposed computational model conveniently and accurately computes these fields based on the mixed finite element approach.

A number of challenges remain to be investigated in predictive modeling of transport-deformation problems. One of the main challenges is because of the localized character of the transport process. In some practical problems, the oxygen ingress is localized within a very small boundary region of the structure with a thickness of the order of a few grain diameters. Accurate characterization of localized deformation and failure within this zone necessitates resolution of the grain scale deformation and transport processes within the boundary region. Multiscale computational models that can accurately incorporate such grain scale information into a structural scale problem remain an outstanding issue. Such models are currently under investigation [35] and will be employed to address localized coupled transport - inelastic deformation problems.

Chapter 3

A VISCOELASTIC-VISCOPLASTIC MODEL OF TITANIUM STRUCTURES SUBJECTED TO THERMO-CHEMO-MECHANICAL ENVIRONMENT

3.1 Introduction

Understanding and predicting the mechanical performance of metallic material and structural systems operating in combined environments have been active research topics for decades. Combined environment refers to the simultaneous presence of potentially aggressive environmental agents, elevated temperatures and thermal loads, and a variety of mechanical loads. In a combined high-temperature environment, aggressive environmental elements tend to deteriorate the mechanical performance of the material. A case in point is the effect of oxygen ingress into titanium alloys, which results in significant changes in the material properties including embrittlement, increased hardness, and dramatic reduction in fatigue life [23, 24].

Modeling and prediction of the oxygen ingress induced deterioration in structures made of titanium and other alloys is of particular concern for aerospace structural components employed in hypersonic air vehicles. The perceived operating thermo-mechanical conditions for hypersonic structures are typically at the upper end of the capability spectra of titanium alloys. In the presence of high temperatures, atmospheric oxygen tends to diffuse into the alloy, leading to the deterioration of the material properties marked by a strong coupling between oxygen transport and mechanical deformation. The presence of elevated concentrations of oxygen at lattice interstitials and trap sites (e.g., dislocations) causes lattice straining, and inhibits dislocation glide, leading to hardening and embrittlement (i.e., early onset of fracture initiation). Further increase of oxygen content leads to phase transformation (e.g., from β to α) and formation of an oxide layer. The diffusion of oxygen

is also affected by the deformation processes and damage state since the microcrack formation within the brittle oxygen-rich layer as dislocations serve as preferential sites for oxygen. The presence of surface microcracks and microvoids that typically (but not necessarily) originate at the triple junctions and at grain boundaries also enhances diffusivity of oxygen deeper towards the interior of the structure.

Extensive research exists on experimental and modeling based investigations of oxygen ingress into titanium alloys (e.g., [12, 13, 14, 15]). A comprehensive review of earlier diffusivity characterization of titanium and titanium alloys is provided by Liu and Welsch [21]. In contrast, investigations of the coupling mechanisms between oxygen transport, deformation and damage have been relatively scarce. Peters *et al.* [18] experimentally investigated the effect of mechanical loading on the oxygen transport rates. Applied loading beyond yielding showed nominal acceleration of oxygen ingress at elevated temperatures. The authors pointed to the effect of very significant relaxation that dominates the response under sustained deformations, which complicates the coupling between the transport and mechanical processes. Parthasarathy *et al.* [19] proposed a fatigue life prediction methodology for oxygen exposed Titanium alloys subjected to uniaxial tension loads. Pilchak *et al.* [20] provided experimental and fractographic investigation of the effect of high temperature exposure of a near-α titanium alloy undergoing oxygen ingress. More recently Refs. [3, 36] developed a computational transport-deformation model that accounts for the coupling mechanisms between the two physical processes. This model does not adequately account for the relaxation processes that significantly affect both the mechanical response and the coupling mechanisms.

In this chapter, a new coupled deformation-transport model is proposed to study the response of titanium alloys at combined environments. The proposed approach builds on the model by Ref. [3] by extending it to account for creep and relaxation processes, which are critical to the response characterization at high temperatures. The coupled-transport model is implemented using a three field formulation, in which concentration, displacement

and pressure are evaluated as independent unknowns [36]. The transport solver includes pressure dependent advection and reaction terms, which are stabilized using the Galerkin least-squares stabilization method [31]. The computational model was validated against experiments conducted in combined environments. The two main novel contributions of this chapter are: (1) The proposed model accurately captures the time-dependent creep/relaxation processes through the incorporation of viscoelastic-viscoplastic mechanisms. The authors' previous modeling work did not provide the necessary relaxation mechanisms at elevated temperatures [3]; (2) A detailed investigation of the coupling mechanisms between the oxygen ingress induced embrittlement, relaxation and the inelastic deformation is provided, including partial validation of the interaction mechanisms based on experimental data.

The remainder of this chapter is organized as follows: Section 3.2 provides the formulation of viscoelastic-viscoplastic model coupled with the oxygen transport model. The finite element implementation of the viscoelastic-viscoplastic deformation model is described in Section 3.3. Section 3.4 details the numerical investigation of a high-temperature titanium alloy of interest, Ti-6242S, subjected to combined loading and high temperature environment. The calibration of the proposed model based on the independent set of experimental data and a detailed analysis of the failure and relaxation characteristics of oxygen-exposed specimens are included in this section. The conclusions and future research directions are included in Section 3.5.

3.2 Problem Statement

The problem domain is described in Fig. 3.1, where the solid body, $\Omega \subset \mathbb{R}^{n_{\text{sd}}}$ is subjected to an aggressive agent (oxygen) at the exterior surfaces of the problem domain (n_{sd}: number of space dimensions). The ingressed oxygen results in a more brittle and hardening material compared to the substrate alloy, where surface cracks will initiate under mechanical loading, as shown in Fig. 3.1. In this section the viscoelastic-viscoplastic deformation

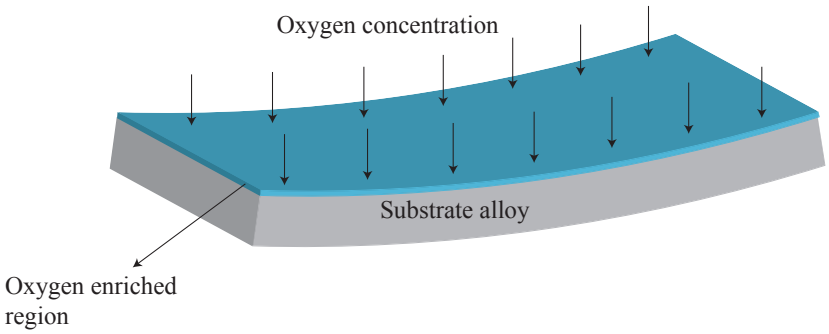

Figure 3.1: Structural component subjected to coupled transport-deformation processes.

model is formulated together with the transport model. The oxidation mechanism as well as its effects on mechanical property degradation including the loss of ductility and hardening are investigated.

3.2.1 Deformation Model

In this section, a viscoelastic-viscoplastic model is defined to describe deformation behavior in the presence of aggressive agents that affect the mechanical response. The model presented here extends the coupled transport-deformation model presented in [3] to account for the relaxation/creep behavior, which is predominant in combined environment response at elevated temperatures, which also activates aggressive agent transport within the solid. In particular, the alloys of interest could demonstrate relaxation up to near stress-free states at elevated temperatures (see Section 3.4). The purpose of the proposed model is to accurately idealize the short-term (i.e., a few seconds) and the long-term (i.e., in the order of hours) time dependent creep/relaxation behavior. From the rheological perspective, the viscoelastic-viscoplastic model is a three-dimensional generalization of Wiechert springs serially connected to a viscoplastic device as illustrated in Fig. 3.2.

The governing equilibrium equations describing the mechanical response is expressed in the following form:

$$s_{ij,j}(\mathbf{x},t) - p_{,i}(\mathbf{x},t) + b_i(\mathbf{x},t) = 0 \tag{3.1}$$

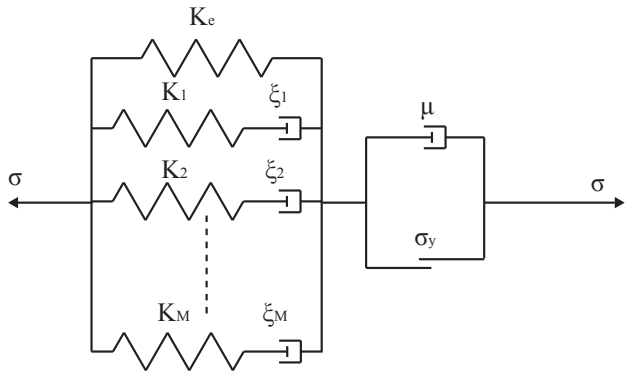

Figure 3.2: One dimensional rheological representation of the viscoelastic-viscoplastic model.

where, **b** the body force per unit volume; **s** is the deviatoric stress tensor; $p = -\text{tr}(\boldsymbol{\sigma})/3$ the pressure; $\boldsymbol{\sigma}$ the stress tensor ($\boldsymbol{\sigma} = \mathbf{s} - p\boldsymbol{\delta}$); $\boldsymbol{\delta}$ the second order identity tensor; and $\text{tr}(\cdot)$ denotes trace. I adopt the index notation in the problem formulation (i.e., $i = 1, ..., n_{\text{sd}}$). Repeated indices of the spatial dimensions indicate summation unless otherwise stated. A subscript followed by a comma indicates partial derivative (i.e., $f_{,i} = \partial f / \partial x_i$). **x** and t parameterize the spatial and temporal dimensions, respectively. Bold symbol indicates vector notation (i.e., $\mathbf{x} = [x_1, x_2, x_3]$ for $n_{\text{sd}} = 3$) and superscribed dot indicates differentiation with respect to time. The following boundary conditions are prescribed to evaluate the mechanical problem:

$$u_i(\mathbf{x}, t) = \bar{u}_i(\mathbf{x}, t) \qquad \mathbf{x} \in \Gamma_D^u \tag{3.2}$$

$$\sigma_{ij} n_j = \bar{t}_i(\mathbf{x}, t) \qquad \mathbf{x} \in \Gamma_N^u \tag{3.3}$$

where, **u** denotes the displacement vector field; $\bar{\mathbf{u}}$ is the prescribed displacement along the Dirichlet boundary; Γ_D^u; $\bar{\mathbf{t}}$ the prescribed traction along the Neumann boundary, Γ_N^u, such that $\Gamma_D^u \cap \Gamma_N^u = \emptyset$ and $\Gamma_D^u \cup \Gamma_N^u = \Gamma$; and **n** the outer unit normal to the traction boundary.

Assuming small strain kinematics, the total strain tensor, ε, is:

$$\varepsilon_{ij} = \frac{1}{2}\left(u_{i,j}(\mathbf{x}, t) + u_{j,i}(\mathbf{x}, t)\right) \tag{3.4}$$

The adoption of the small strain theory implies that large rotations and large plastic deformations that may be present in some high temperature applications are not included in this study. The total deformation in the viscoelastic-viscoplastic model is separated into four components:

$$\varepsilon_{ij} = \varepsilon_{ij}^{\mathrm{ve}} + \varepsilon_{ij}^{\mathrm{vp}} + \varepsilon_{ij}^{\mathrm{T}} + \varepsilon_{ij}^{\mathrm{c}} \tag{3.5}$$

$\varepsilon^{\mathrm{ve}}$, $\varepsilon^{\mathrm{vp}}$, ε^{T} and ε^{c} respectively denote the viscoelastic, viscoplastic, thermal and elevated aggressive agent concentration induced strain, respectively.

The constitutive relationship between the deviatoric stress and the viscoelastic strain is modeled using the Boltzmann superposition integral in the context of linear viscoelasticity:

$$s_{ij}(t) = \int_0^t L'_{ijkl}(t-\tau)\frac{d\varepsilon_{kl}^{\mathrm{ve}}(\tau)}{d\tau}d\tau \tag{3.6}$$

in which, the spatial dependence of the pertinent fields is suppressed for simplicity. $\mathbf{L}'$ is the time-dependent deviatoric component of the tensor of viscoelastic moduli, taken to be symmetric and positive definite at any time during the deformation process:

$$L'_{ijkl} = L'_{klij} = L'_{jikl} = L'_{ijlk} \tag{3.7}$$

$$\zeta_{ij}L'_{ijkl}\zeta_{kl} \geq \eta\,\zeta_{ij}\zeta_{ij}; \quad \forall\zeta_{ij} = \zeta_{ji}; \quad \eta > 0 \tag{3.8}$$

A convenient time evolution expression for the viscoelastic moduli is the Prony series:

$$L'_{ijkl}(t) = \left[K_e + \sum_{m=1}^{M} K_m \exp\left(-\frac{t}{\xi_m}\right)\right]\bar{L}'_{ijkl} \tag{3.9}$$

in which, $\bar{\mathbf{L}}'$ is a time independent moduli tensor; M the number of Maxwell elements incorporated in the Wiechert model; K_e is the ratio of equilibrium deviatoric moduli over instantaneous deviatoric moduli; and K_m and ξ_m are the ratio of deviatoric moduli on m^{th} Maxwell element over instantaneous deviatoric moduli and the time parameters in the m^{th}

Maxwell element, respectively. By employing the above expression, all components of the viscoelastic moduli relax uniformly. A straightforward generalization to component-dependent relaxation is possible by using a slightly modified version of the Prony series approximation. By constraining the values of the Prony series parameters such that $K_e + \sum_{m=1}^{M} K_m = 1$, the time independent moduli tensor becomes the instantaneous elastic moduli; i.e., $\bar{\mathbf{L}}' = \mathbf{L}'(t=0)$.

For an isotropic solid, the deviatoric component of the elastic moduli is expressed as:

$$L'_{ijkl}(t) = 2G(t)\left(\delta_{ik}\delta_{jl} - \frac{1}{3}\delta_{ij}\delta_{kl}\right) \tag{3.10}$$

Substituting Eqs. 3.9 and 3.10 into Eq. 3.6, the deviatoric stress tensor is expressed as:

$$s_{ij}(t) = 2\bar{G}K_e\varepsilon^{\mathrm{ve}}_{ij}(t) + 2\bar{G}\sum_{m=1}^{M} K_m\varepsilon^{m}_{ij}(t) \tag{3.11}$$

where,

$$\varepsilon^{m}_{ij}(t) = \int_0^t \exp\left(-\frac{t-\tau}{\xi_m}\right)\frac{d\varepsilon^{\mathrm{ve}}_{ij}(\tau)}{d\tau}d\tau \tag{3.12}$$

in which, $\varepsilon^{\mathrm{ve}}$ is the deviatoric component of the viscoelastic strain, and $\bar{G} = G(0)$ the instantaneous shear modulus.

The variation of the relaxation behavior as a function of temperature is modeled using the Williams-Landel-Ferry (WLF) equation. Let a_T denote the WLF time-temperature shift factor expressed in the form:

$$\log a_T(T) = \frac{-C_1(T - T_{\mathrm{ref}})}{C_2 + (T - T_{\mathrm{ref}})} \tag{3.13}$$

where, T denotes temperature; C_1 and C_2 are material constants and T_{ref} is the reference temperature, taken to be the room temperature in this study. Provided the relaxation behavior at the reference temperature and the material constants are known, the relaxation behavior at an arbitrary temperature is obtained by shifting the time scale within a master

WLF curve using a_T:

$$t = \int_0^{\tau} \frac{d\xi}{a_T\left(T(\xi)\right)} \tag{3.14}$$

The thermal and aggressive agent concentration induced strains are taken to be volumetric:

$$\varepsilon_{ij}^{\mathrm{T}} = \alpha\left(T - T_{\mathrm{ref}}\right)\delta_{ij} \tag{3.15}$$

$$\varepsilon_{ij}^{\mathrm{c}} = \vartheta\left(c - c_{\infty}\right)\delta_{ij} \tag{3.16}$$

where, α is the thermal expansion coefficient; c the concentration; and ϑ the concentration induced volumetric expansion coefficient. The viscoplastic strain is taken to remain in the deviatoric strain space (i.e., $\mathrm{tr}(\varepsilon^{\mathrm{vp}}) = 0$). Considering an isotropic solid with insignificant relaxation under hydrostatic loading, the constitutive relationship for pressure becomes:

$$p(t) = -ku_{i,i}(t) + 3k\left[\alpha\left(T(t) - T_0\right) + \vartheta\left(c(t) - c_{\infty}\right)\right] \tag{3.17}$$

in which, k is the bulk modulus.

The evolution of the viscoplastic strain is modeled by a generalization of the Johnson-Cook plasticity model to account for the effects of elevated aggressive agent concentration. The viscoplastic model employed in this study accounts for the effects of embrittlement and hardening as a function of the aggressive agent concentration [3]. The flow rule of the viscoplastic strain is expressed in terms of a power law:

$$\dot{\varepsilon}_{ij}^{\mathrm{vp}} = \gamma\left\langle \frac{f}{\sigma_Y} \right\rangle^{q(T^*)} \frac{\partial f}{\partial \sigma_{ij}} \tag{3.18}$$

where, γ is the fluidity parameter; $\langle\cdot\rangle$ denotes Macaulay brackets (i.e., $\langle\cdot\rangle = ((\cdot) + |\cdot|)/2$); σ_Y the flow stress; and $f(\boldsymbol{\sigma}, \sigma_Y)$ the loading function. The viscoplastic hardening exponent,

q, is expressed as a function of the non-dimensional temperature, T^*, as:

$$q(T^*) = q_{\text{ref}} + (\bar{q} - q_{\text{ref}})T^*; \quad T^\star = \frac{T - T_{\text{ref}}}{\bar{T} - T_{\text{ref}}} \tag{3.19}$$

where $q_{\text{ref}} = q(T_{\text{ref}})$ and $\bar{q} = q(\bar{T})$ are exponents evaluated at two temperatures.

The Von-Mises loading function is adopted in this study:

$$f\left(\sigma_{ij}, \sigma_Y\right) = \sigma_{eq} - \sigma_Y = \sqrt{3}\bar{s} - \sigma_Y \tag{3.20}$$

in which, σ_{eq} is the equivalent stress; and $\bar{s}$ the second invariant of the deviatoric stress, $\mathbf{s}$. The generalized Johnson-Cook flow stress provides a functional relationship between yielding and the strain, temperature and concentration:

$$\sigma_Y = [A + B(\bar{\varepsilon}^{\text{vp}})^n + F(c - c_\infty)][1 - (T^\star)^m] \tag{3.21}$$

in which A,B, F, m and n are material parameters. When the non-dimensional temperature reaches unity, Eq. 3.21 implies complete lack of material strength. In some applications of similar models, the non-dimensional temperature is expressed using the melting temperature (i.e., $\bar{T} = T_{\text{melt}}$). For the titanium alloys of interest, the extrapolation of the experimental data on the yield strength variation as a function of temperature indicates vanishing yield strength at around the beta transus temperature. I therefore use $\bar{T} = T_\beta$ in this study. It must be noted that it is impractical to characterize q in Eq. 3.19 by an experiment conducted at the beta transus temperature. Since the temperature variation of the exponent is linear, an experiment conducted at any temperature between T_{ref} and T_β is sufficient to identically calibrate q.

The equivalent viscoplastic strain $\bar{\varepsilon}^{\text{vp}}$ is defined as:

$$\bar{\varepsilon}^{\text{vp}} = \sqrt{\frac{2}{3}\varepsilon_{ij}^{\text{vp}} : \varepsilon_{ij}^{\text{vp}}} \tag{3.22}$$

The damage progression within the material is modeled as a function of temperature and concentration. Let the damage parameter, ω, be the ratio between the equivalent strain, $\bar{\varepsilon}^{vp}$ and the failure strain, ε_f:

$$\omega = \frac{\bar{\varepsilon}^{\mathrm{vp}}}{\varepsilon_f} \tag{3.23}$$

$\omega \in [0,1)$ denotes the state of damage at a material point, with ω=0 indicating no additional defect compared to the initial state, and, ω=1 corresponds to loss of load carrying capacity at the material point. The failure strain ε_f is described as:

$$\varepsilon_f = D_1(c)\left(1 + D_5 \exp\left(D_6 T^{\star}\right)\right) \tag{3.24}$$

in which, D_5 and D_6 parameterizes the effect of temperature on the failure strain. D_1 varies as a function of concentration and idealizes the progressive embrittlement due to aggressive agent ingress:

$$D_1(c) = \begin{cases} D_1^{\infty} & \text{if} \quad c \leqslant c_{\infty} \\ \frac{1}{c_{\infty} - c_{\mathrm{crit}}}\left(\left(D_1^{\infty} - D_1^{\alpha}\right)c + D_1^{\alpha} c_{\infty} - D_1^{\infty} c_{\mathrm{crit}}\right) & \text{if} \quad c_{\infty} < c < c_{\mathrm{crit}} \\ D_1^{\alpha} & \text{if} \quad c \geqslant c_{\mathrm{crit}} \end{cases} \tag{3.25}$$

D_1^{∞} denotes the failure strain at room temperature in the absence of elevated concentration; D_1^{α} denotes failure strain beyond a critical concentration, c_{crit}; and the embrittlement is assumed to be linear at intermediate concentration values. The effect of aggressive agent ingress on the mechanical response is modeled based on the concentration dependent terms in Eqs. 3.21 and 3.25. In Eq. 3.21, the flow stress is affected by the concentration. Elevated concentration tends to harden the material. In addition to hardening, the elevated concentration embrittles the response by reducing the failure strain in Eq. 3.24.

In an alternative approach, the plasticity theory has been extended to account for relaxation below the yield values and employed to describe cyclic response at high tempera-

ture [37]. This approach presents a model that can also capture the viscoelastic response in cyclic loading through viscoplastic modeling together with pure kinematic hardening. The key assumption made is the vanishing threshold for yielding, which links the response to the viscoelastic regime. The treatment of viscoelasticity is spectral in contrast to the integral type viscoelasticity considered herein. The approach taken in this chapter therefore constitutes a complimentary proposition to the ideas of Ref. [37].

3.2.2 Transport Model

By incorporating Oriani's equilibrium theory to describe the diffusion of the aggressive agent into the stressed solid [26] and considering the effect of stress on the diffusion process, the governing equation of the aggressive agent transport is expressed as an advection-reaction-diffusion problem of the form:

$$\dot{c} - \left(Dc_{,i}\right)_{,i} + \alpha_i c_{,i} + \beta c = 0 \tag{3.26}$$

in which, D is the diffusivity of the aggressive agent within the solid, and c the concentration of aggressive agent, given as weight ratio of the diffusing agent and the solid substrate within an infinitesimal control volume. α_i and β are coefficients of advection and reaction, respectively, expressed as a function of pressure gradient and Laplacian:

$$\alpha_i = -\frac{D\bar{V}_c}{RT} p_{,i} \tag{3.27}$$

$$\beta = \left(\frac{D\bar{V}_c T_{,i}}{RT^2} - \frac{D_{,i}\bar{V}_c}{RT}\right) p_{,i} - \frac{D\bar{V}_c}{RT} p_{,ii} \tag{3.28}$$

in which, R is the universal gas constant; and $\bar{V}_c$ the partial molar volume of the ingressed gas in the substrate solid.

The initial and boundary conditions for the transport problem are expressed as:

$$c(\mathbf{x}, t=0) = c_\infty(\mathbf{x}); \qquad \mathbf{x} \in \Omega \tag{3.29}$$

$$c(\mathbf{x}, t) = c_0(\mathbf{x}, t); \qquad \mathbf{x} \in \Gamma_c \tag{3.30}$$

$$q_i(\mathbf{x}, t)\, n_i = 0; \qquad \mathbf{x} \in \Gamma_q \tag{3.31}$$

in which, c_∞ is the concentration of the aggressive agent at the natural state of the solid; c_0 the boundary concentration prescribed along Γ_c; $\mathbf{q}$ the concentration flux; and $\mathbf{n}$ the outward normal unit vector to the boundary, Γ_q.

The transport process is coupled to the mechanical deformation through two mechanisms. The first is the stress dependent advection and reaction flow, as shown in Eqs. 3.27 and 3.28. The second is by linking the diffusivity to the state of damage within the solid. Considering the enhancement of diffusivity as the increased defect density [28, 27, 29], the diffusivity is modeled based on the percolation theory [3] as:

$$D(\omega, T) = D_0\,(1 + \mathscr{D}(\omega)) \exp\left(-\frac{Q}{RT}\right) \tag{3.32}$$

where, D_0 is the pre-exponential constant; Q the activation energy; and, $\mathscr{D}(\omega)$ the effect of mechanical damage on diffusivity:

$$\mathscr{D}(\omega) = \begin{cases} a\omega; & \omega < \omega_c \\ a\omega - \dfrac{(\omega - \omega_c)^2}{\omega - \omega_{ec}}; & \omega_c \leqslant \omega < \omega_{ec} \\ \infty; & \omega \geqslant \omega_{ec} \end{cases} \tag{3.33}$$

in which, ω_c and ω_{ec} denote the conduction and elastic percolation thresholds respectively; and, a is a material parameter.

The diffusivity is in a linear relationship with the damage variable when damage is smaller than the conduction percolation threshold value ($\omega < \omega_c$) [28]. The state when

the damage exceeds the elastic percolation threshold, ω_{ec}, indicates a physical crack which allows free flow of the aggressive agent. Beyond ω_{ec}, $\mathscr{D}(\omega)$ is assigned a large but finite value to avoid numerical instability. At intermediate values of the damage state, the diffusivity progressively increases as a function of damage [30].

The mechanical state in the proposed model influences transport in two ways: (1) the increased diffusivity as a function of the damage parameter through damage percolation idea [29]; and (2) the advection induced by pressure gradients. In the presence of a distinct crack or notch (either initially present or formed during the process), the pressure gradients within the process zones produce a non-zero advection term in the transport equation and induce transport of the aggressive agent, even in the absence of elevated concentration around external boundaries. This capability of the model was demonstrated in Yan *et al.* [36]. Mechanism (1), in the absence of the formation of a distinct crack, does not introduce transport as only the apparent diffusivity parameter is increased by the presence of damage. In the investigations discussed in this chapter (i.e., oxygen transport in a titanium alloy) the gradient-induced transport alone would not cause significant embrittlement since, the amount of oxygen content in the bulk alloy is very low (i.e., approximately 0.15 %wt).

3.3 Numerical Implementation of the Deformation Model

The deformation and transport models described in Section 3.2 are numerically evaluated using a coupled finite element formulation. The evaluation of the transport problem is performed based on the Galerkin Least Squares stabilized finite element method [32]. The stabilized approach eliminates potential instabilities resulting from the advection dominated flow generated around zones of stress concentration such as crack and notch tips.

The coupled solution of the deformation and transport problems are performed based on a staggered solution strategy of isothermal type. In this strategy, the mechanical and transport problems are evaluated in turn until convergence is achieved in both problems at

each time step. When solving the transport problem, the pressure and the pressure gradients are considered as known fields, computed in the deformation problem. Similarly in the deformation problem, the concentration field is considered known computed in the evaluation of the transport problem at the current iteration. The thermal state of the system is regarded as an input to both transport and mechanical solvers. The thermal state of the structure is critical to the overall coupled chemo-mechanical deformation and failure behavior. The transient thermal diffusion, which is not modeled in this chapter, may also be important in certain problems such as in the presence of high rate deformation. All cases in this chapter investigate relatively long term behavior, in which isothermal conditions prevail (hours to hundreds of hours). The thermal steady state is typically reached in a matter of a few seconds, and therefore the thermal transients do not significantly affect the chemo-mechanical processes. A detailed formulation of the transport problem and the coupled solution algorithm has been provided in Ref. [36].

In the remainder of this section, a mixed finite element formulation is proposed and formulated for the viscoelastic-viscoplastic deformation model. In contrast to the traditional purpose of the mixed formulations (e.g., address incompressibility), the current formulation employs the mixed approach to obtain an accurate description of the pressure and pressure gradient fields. The pressure and pressure gradient fields are in turn used to describe the advection and reaction components of the transport equation.

3.3.1 Recurrence formula for deviatoric stress tensor

A direct computation of the stress based on the viscoelastic strain (i.e., Eq. 3.11) requires the storage of and computation using the entire strain history. Storage of the entire strain history at each integration point within a large discretized domain is clearly expensive from the memory perspective. In order to reduce the memory cost, a recurrence formula has been employed [38]. Consider a time discretization of the governing deformation problem and let the left subscripts t denote the value of a response field at the previous equilibrated

increment. Left subscripts $t+\Delta t$ indicates the response field evaluated at the current increment. For simplicity, the left subscript for the current increment is sometimes omitted. From Eq. 3.12, the values of ε at the previous and current increments are respectively:

$$ {}_{t}\varepsilon_{ij}^{m} = \int_{0}^{t} \exp\left(-\frac{t-\tau}{\xi_m}\right) \frac{d\varepsilon_{ij}^{\mathrm{ve}}(\tau)}{d\tau} d\tau \tag{3.34} $$

$$ {}_{t+\Delta t}\varepsilon_{ij}^{m} = \int_{0}^{t} \exp\left(-\frac{t+\Delta t-\tau}{\xi_m}\right) \frac{d\varepsilon_{ij}^{\mathrm{ve}}(\tau)}{d\tau} d\tau + \int_{t}^{t+\Delta t} \exp\left(-\frac{t+\Delta t-\tau}{\xi_m}\right) \frac{d\varepsilon_{ij}^{\mathrm{ve}}(\tau)}{d\tau} d\tau \tag{3.35} $$

Assuming that the viscoelastic strain $\varepsilon^{\mathrm{ve}}$ varies linearly within the current time step:

$$ {}_{t+\Delta t}\varepsilon_{ij}^{m} = \exp\left(-\frac{\Delta t}{\xi_m}\right) {}_{t}\varepsilon_{ij}^{m} + \frac{{}_{t+\Delta t}\varepsilon_{ij}^{\mathrm{ve}} - {}_{t}\varepsilon_{ij}^{\mathrm{ve}}}{\Delta t} \xi_m \left(1 - \exp\left(-\frac{\Delta t}{\xi_m}\right)\right) \tag{3.36} $$

Subtracting the deviatoric stress tensor evaluated at the previous and current time steps using Eq. 3.11, and employing Eq. 3.36 yields:

$$ s_{ij} - {}_{t}s_{ij} = 2\bar{G}\left(\varepsilon_{ij}^{\mathrm{ve}} - {}_{t}\varepsilon_{ij}^{\mathrm{ve}}\right)\bar{K} - 2\bar{G}\sum_{m}^{M} K_m \left(1 - \exp\left(-\frac{\Delta t}{\xi_m}\right)\right) {}_{t}\varepsilon_{ij}^{m} \tag{3.37} $$

where,

$$ \bar{K} = K_e + \sum_{m}^{M} K_m \left(1 - \exp\left(-\frac{\Delta t}{\xi_m}\right)\right) \frac{\xi_m}{\Delta t} \tag{3.38} $$

Equation 3.37 indicates that the calculation of the deviatoric stress at current time step requires the value of ε at the previous time step, only rather than its entire history, significantly reducing the computing and memory requirements.

3.3.2 Mixed FEM formulation of the viscoelastic-viscoplastic deformation model

The weak forms of the governing equations of equilibrium in terms of the deviatoric stress and pressure (i.e., Eqs. 3.1 and 3.17, respectively) are expressed as:

$$\int_{\Omega} v^h_{i,j} s_{ij} d\Omega - \int_{\Omega} v^h_{i,i} p d\Omega - \int_{\Gamma^u_N} v^h_i \bar{t}_i d\Gamma - \int_{\Omega} v^h_i b_i d\Omega = 0 \tag{3.39}$$

$$\int_{\Omega} \frac{1}{k} q^h p^h d\Omega + \int_{\Omega} q^h u^h_{i,i} d\Omega - \int_{\Omega} 3q^h [\alpha (T - T_0) + \vartheta (c - c_\infty)] d\Omega = 0 \tag{3.40}$$

where, $\mathbf{v}$ and q are the test functions for displacement and pressure, defined within the appropriate Sobolev spaces and with sufficient smoothness. Let $\mathbf{v}^h$ and q^h belong to the corresponding finite dimensional subspaces of the test functions, $\mathbf{v}$ and q, respectively. I perform a Bubnov-Galerkin discretization of the displacement and pressure fields, as well as the corresponding test functions:

$$u^h_i (\mathbf{x}, t) = \sum_{a=1}^{n_u} N^u_a (\mathbf{x}) \hat{u}_{ai} (t) \tag{3.41}$$

$$p^h (\mathbf{x}, t) = \sum_{a=1}^{n_p} N^p_a (\mathbf{x}) \hat{p}_a (t) \tag{3.42}$$

in which, N^u_a and N^p_a are respectively the basis functions of the displacement and pressure fields that correspond to node a; $\hat{(\cdot)}$ denotes the nodal coefficients of the corresponding field; and n_u and n_p are the total number of displacement and pressure nodes, respectively.

Substituting Eqs. 3.41 and 3.42 into Eqs. 3.39 and 3.40, respectively, the discretized equilibrium equations take the form:

$$\Psi_{bi} := \int_{\Omega} N^u_{b,j} s_{ij} d\Omega - \sum_{c=1}^{n_p} \int_{\Omega} N^u_{b,i} N^p_c d\Omega \hat{p}_c - \int_{\Gamma^u_N} N^u_b \bar{t}_i d\Gamma - \int_{\Omega} N^u_b b_i d\Omega = 0; \quad b = 1, ..., n_u \tag{3.43}$$

$$\Theta_c := \sum_{a=1}^{n_p} \int_\Omega \frac{1}{k} N_c^p N_a^p d\Omega \hat{p}_a + \sum_{b=1}^{n_u} \int_\Omega N_c^p N_{b,i}^u d\Omega \hat{u}_{bi} - \int_\Omega 3N_c^p [\alpha (T - T_0) + \vartheta (c - c_\infty)] d\Omega = 0; \quad c = 1, ..., n_p \quad (3.44)$$

Consider a one-parameter family discretization of the viscoplastic strain rate in the form:

$$\frac{{}_{t+\Delta t}\varepsilon_{ij}^{\text{vp}} - {}_t\varepsilon_{ij}^{\text{vp}}}{\Delta t} = \theta \, {}_{t+\Delta t}\dot{\varepsilon}_{ij}^{\text{vp}} + (1-\theta) \, {}_t\dot{\varepsilon}_{ij}^{\text{vp}} \quad (3.45)$$

in which, $\theta \in [0,1]$ is an algorithmic parameter. The choices of $\theta = 0, 1$ and 0.5 correspond to the explicit, implicit and midpoint rules, respectively. Substituting Eqs. 3.5 and 3.41 into Eq. 3.37 and using Eq. 3.45, the discretized form of the constitutive equation for the deviatoric stress is expressed as:

$$R_{ij} :=_{t+\Delta t} s_{ij} -_t s_{ij} - 2\bar{G} \sum_{a=1}^{n_u} N_{a,j}^u (\mathbf{x}) \, {}_{t+\Delta t}\hat{u}_{ai} \bar{K} + 2\bar{G} \sum_{a=1}^{n_u} N_{a,j}^u (\mathbf{x}) \, {}_t\hat{u}_{ai} \bar{K} + 2\bar{G}\Delta t \, \theta \, {}_{t+\Delta t}\dot{\varepsilon}_{ij}^{\text{vp}} \bar{K} + 2\bar{G}\Delta t \, (1-\theta) \, {}_t\dot{\varepsilon}_{ij}^{\text{vp}} \bar{K} + 2\bar{G} \sum_m^M K_m \left(1 - \exp\left(-\frac{\Delta t}{\xi_m}\right)\right) {}_t\varepsilon_{ij}^m \quad (3.46)$$

Equations 3.43, 3.44 and 3.46 together consist of the discretized nonlinear system of the viscoelastic-viscoplastic deformation problem. Newton's method is employed to solve this system of equations [33]. Considering the first order Taylor-series expansion of all three equations yield:

$${}^{k+1}\Psi_{bi} \approx {}^k\Psi_{bi} + {}^k\left(\frac{\partial \Psi_{bi}}{\partial s_{kl}}\right)^{k+1} \delta s_{kl} + \sum_{c=1}^{n_p} {}^k\left(\frac{\partial \Psi_{bi}}{\partial \hat{p}_c}\right)^{k+1} \delta \hat{p}_c = {}^k\Psi_{bi} + \int_\Omega N_{b,j}^u \, {}^{k+1}\delta s_{ij} d\Omega - \sum_{c=1}^{n_p} \int_\Omega N_{b,i}^u N_c^p d\Omega \, {}^{k+1}\delta \hat{p}_c = 0 \quad (3.47)$$

$$
\begin{aligned}
{}^{k+1}\Theta_c &\approx {}^{k}\Theta_c + \sum_{b=1}^{n_u} {}^{k}\left(\frac{\partial \Theta_c}{\partial \hat{u}_{bk}}\right)^{k+1}\delta\hat{u}_{bk} + \sum_{a=1}^{n_p} {}^{k}\left(\frac{\partial \Theta_c}{\partial \hat{p}_a}\right)^{k+1}\delta\hat{p}_a \\
&= {}^{k}\Theta_c + \sum_{b=1}^{n_u}\int_\Omega N_c^p N_{b,i}^u d\Omega\, {}^{k+1}\delta\hat{u}_{bi} + \sum_{a=1}^{n_p}\int_\Omega \frac{1}{k} N_c^p N_a^p d\Omega\, {}^{k+1}\delta\hat{p}_a = 0
\end{aligned} \tag{3.48}
$$

$$
\begin{aligned}
{}^{k+1}R_{ij} &\approx {}^{k}R_{ij} + {}^{k}\left(\frac{\partial R_{ij}}{\partial s_{kl}}\right)^{k+1}\delta s_{kl} + \sum_{a=1}^{n_u} {}^{k}\left(\frac{\partial R_{ij}}{\partial \hat{u}_{ak}}\right)^{k+1}\delta\hat{u}_{ak} \\
&= {}^{k}R_{ij} - 2\bar{G}\bar{K}\sum_{a=1}^{n_u} N_{a,j}^u\, {}^{k+1}\delta\hat{u}_{ai} + \left(I_{ijkl} + 2\bar{G}\bar{K}\theta\Delta t\, {}^{k}C_{ijkl}\right)^{k+1}\delta s_{kl} = 0
\end{aligned} \tag{3.49}
$$

in which, the left superscript denotes the Newton iteration count. The Taylor series expansion is performed about the previous iteration, k. $\delta(\cdot)$ denotes the incremental change in the corresponding response field $(\cdot)$ within the Newton iteration; and,

$$
{}^{k}C_{ijkl} = {}^{k}\left(\frac{\partial \dot{\varepsilon}_{ij}^{\mathrm{vp}}}{\partial s_{kl}}\right) \tag{3.50}
$$

The increment of deviatoric stress, ${}^{k+1}\delta s_{ij}$ is evaluated using Eq. 3.49 as:

$$
{}^{k+1}\delta s_{ij} = {}^{k}Q_{ijkl}\left(2\bar{G}\bar{K}\sum_{a=1}^{n_u} N_{a,l}^u\, {}^{k+1}\delta\hat{u}_{ak} - {}^{k}R_{kl}\right) \tag{3.51}
$$

where, the modulus ${}^{k}\mathbf{Q}$ is defined as:

$$
{}^{k}Q_{ijkl} = \left(I_{ijkl} + 2\bar{G}\bar{K}\theta\Delta t\, {}^{k}C_{ijkl}\right)^{-1} \tag{3.52}
$$

Substituting Eq. 3.51 into Eqs. 3.47 and 3.48 yield:

$$
\begin{aligned}
&\int_\Omega 2\bar{G}\bar{K}\, {}^{k}Q_{ijkl} N_{b,j}^u \sum_{a=1}^{n_u} N_{a,l}^u d\Omega\, {}^{k+1}\delta\hat{u}_{ak} \\
&\qquad - \sum_{c=1}^{n_p}\int_\Omega N_{b,i}^u N_c^p d\Omega\, {}^{k+1}\delta\hat{p}_c = \int_\Omega {}^{k}Q_{ijkl} N_{b,j}^u\, {}^{k}R_{kl} d\Omega - {}^{k}\Psi_{bi}
\end{aligned} \tag{3.53}
$$

and,

$$-\sum_{b=1}^{n_u}\int_\Omega N_c^p N_{b,i}^u d\Omega\, {}^{k+1}\delta\hat{u}_{bi} - \sum_{a=1}^{n_p}\int_\Omega \frac{1}{k} N_c^p N_a^p d\Omega\, {}^{k+1}\delta\hat{p}_a = {}^{k}\Theta_c \tag{3.54}$$

Equations 3.53 and 3.54 are simultaneously evaluated for the increments of the displacement (${}^{k+1}\delta\hat{\mathbf{u}}$) and pressure fields (${}^{k+1}\delta\hat{\mathbf{p}}$) at the current iteration, $k+1$.

When expressed in the matrix form, Eqs. 3.53 and 3.54 yield:

$$\begin{bmatrix} {}^{k}\mathbf{K}^{uu} & \mathbf{K}^{up} \\ (\mathbf{K}^{up})^T & \mathbf{K}^{pp} \end{bmatrix} \begin{Bmatrix} {}^{k+1}\delta\hat{\mathbf{u}} \\ {}^{k+1}\delta\hat{\mathbf{p}} \end{Bmatrix} = \begin{Bmatrix} {}^{k}\mathbf{f}^{u} \\ {}^{k}\mathbf{f}^{p} \end{Bmatrix} \tag{3.55}$$

in which, the components of the tangent stiffness matrix are expressed as:

$${}^{k}K_{\alpha\beta}^{uu} = \int_\Omega 2\bar{G}\bar{K}^{k} Q_{ijmn} N_{b,j}^u \sum_{a=1}^{n_u} N_{a,n}^u d\Omega; \quad \alpha = b+(i-1)n_u; \quad \beta = a+(m-1)n_u \tag{3.56}$$

$$K_{\alpha c}^{up} = -\int_\Omega N_{b,i}^u N_c^p d\Omega; \quad \alpha = a+(i-1)n_u; \quad 1 \le c \le n_p \tag{3.57}$$

$$K_{ab}^{pp} = -\int_\Omega \frac{1}{k} N_a^p N_b^p d\Omega; \quad 1 \le a,b \le n_p \tag{3.58}$$

The left superscript is included only on the sub matrix, $\mathbf{K}^{uu}$, which is the only nonlinear part of the tangent stiffness. The unknown displacement and pressure coefficients, as well as the force vectors are expressed in the vector form as:

$${}^{k+1}\delta\hat{\mathbf{u}} = \{{}^{k+1}\hat{u}_1, ..., {}^{k+1}\hat{u}_{n_{\mathrm{sd}}\times n_{\mathrm{u}}}\}^T; \quad {}^{k}\mathbf{f}^{u} = \{{}^{k}f_1^u, ..., {}^{k}f_{n_{\mathrm{sd}}\times n_{\mathrm{u}}}^u\}^T \tag{3.59}$$

$${}^{k+1}\delta\hat{\mathbf{p}} = \{{}^{k+1}\hat{p}_1, ..., {}^{k}\hat{p}_{n_p}\}^T; \qquad {}^{k}\mathbf{f}^{p} = \{{}^{k}f_1^p, ..., {}^{k}f_{n_p}^p\}^T \tag{3.60}$$

and the components of the force vector are given as:

$${}^{k}f_\alpha^u = \int_\Omega {}^{k}Q_{ijkl} N_{b,j}^u {}^{k}R_{kl} d\Omega - {}^{k}\Psi_{bi}; \quad \alpha = b+(i-1)n_u \tag{3.61}$$

$${}^{k}f_a^p = {}^{k}\Theta_a; \quad 1 \le a \le n_p \tag{3.62}$$

The finite elements discretizing the displacements and the pressure fields are chosen

in order to satisfy the Babuska-Brezzi constraint. Ensuring this constraint is satisfied in the choice of the pressure and displacement discretizations avoids the potential numerical instability and response oscillations observed in mixed formulations. In the numerical studies provided in this chapter, I employ nine-node biquadratic in displacement and four-node bilinear in pressure Taylor-Hood element.

Based on the expressions above, I employ the following algorithm to compute the pressure and displacement fields:

At arbitrary time $t+\Delta t$: Given the state at the previous time step; ${}_t\hat{\mathbf{u}}$, ${}_t\hat{\mathbf{p}}$, ${}_t\mathbf{s}$ and ${}_t\dot{\varepsilon}^{\mathrm{vp}}$; Find the response at the current step; $\hat{\mathbf{u}}$, $\hat{\mathbf{p}}$.

1. Initiate the algorithm: $k=0$.

2. Set the initial guesses for the pressure and deformation coefficients at the current increment:

$$ {}^0\hat{\mathbf{u}} = {}_t\hat{\mathbf{u}}; \quad {}^0\hat{\mathbf{p}} = {}_t\hat{\mathbf{p}}; \quad {}^0\mathbf{s} = {}_t\mathbf{s}; \quad {}^0\dot{\varepsilon}^{\mathrm{vp}} = {}_t\dot{\varepsilon}^{\mathrm{vp}} \tag{3.63} $$

3. Loop until convergence:

   (a) Compute the moduli: $\bar{K}$, ${}^k\mathbf{C}$ and ${}^k\mathbf{Q}$ using Eqs. 3.38, 3.50 and 3.52, respectively.

   (b) Calculate ${}^k\mathbf{\Psi}$, ${}^k\mathbf{\Theta}$ and ${}^k\mathbf{R}$ using Eqs. 3.43, 3.44 and 3.46, respectively.

   (c) Update the pressure and displacement increments, ${}^{k+1}\delta\hat{\mathbf{u}}$ and ${}^{k+1}\delta\hat{\mathbf{p}}$ by solving the linear system in Eq. 3.55.

   (d) Compute deviatoric stress increment ${}^{k+1}\delta\mathbf{s}$ at each integration point using Eq. 3.51.

   (e) Update displacement, pressure and stress:

$$ {}^{k+1}\hat{\mathbf{u}} = {}^{k+1}\delta\hat{\mathbf{u}} + {}^k\hat{\mathbf{u}} \tag{3.64} $$

$$ {}^{k+1}\hat{\mathbf{p}} = {}^{k+1}\delta\hat{\mathbf{p}} + {}^k\hat{\mathbf{p}} \tag{3.65} $$

$$ {}^{k+1}\mathbf{s} = {}^{k+1}\delta\mathbf{s} + {}^k\mathbf{s} \tag{3.66} $$

(f) Update ${}^{k+1}\dot{\varepsilon}^{\text{vp}}$ and ${}^{k+1}\varepsilon^{\text{vp}}$ by simultaneously evaluating:

$$ {}^{k+1}\varepsilon^{\text{vp}} = {}_{t}\varepsilon^{\text{vp}} + \theta\Delta t\, {}^{k+1}\dot{\varepsilon}^{\text{vp}} + (1-\theta)\Delta t\, {}_{t}\dot{\varepsilon}^{\text{vp}} \tag{3.67} $$

$$ {}^{k+1}\dot{\varepsilon}^{\text{vp}} = \gamma\left\langle \frac{{}^{k+1}f}{{}^{k+1}\sigma_Y} \right\rangle^{q\ \ k+1} \left(\frac{\partial f}{\partial \boldsymbol{\sigma}} \right) \tag{3.68} $$

(g) $k = k+1$

3.4 Numerical Investigation of Ti-6242S Response in Combined Environment

The proposed computational model was employed to investigate the mechanical response of a titanium alloy exposed to oxygen at elevated temperatures. I focus on modeling the near alpha titanium alloy, Ti-6Al-2Sn-4Zr-2Mo-0.1Si (Ti-6242S) within a temperature range of 23-650^{0}C. Ti-6242S displays good mechanical properties at elevated temperature, making them a candidate structural material for hypersonic aircraft applications. The applicability of the proposed model to idealize the behavior of the alloy requires temperature stability, since the effect of microstructure evolution is not explicitly included. The tensile strength properties of Ti-6242S have been reported to be largely unaffected at creep - high temperature exposure conditions up to 650^{0}C [39]. While the micrographs of from the experimental investigations considered in this study is not available, the literature on prior experiments and imaging performed on aged specimens at temperatures up to 650^{0}C points to limited microstructure evolution (see e.g., [40]). It is possible that even higher temperatures would induce microstructural evolution that will significantly alter the physical mechanisms that shape the relaxation, creep and other mechanical behavior of this alloy. It is noted that the maximum temperature covered in this study already extends the range of temperatures considered in applications of Ti-6242S, which is typically limited to 500-550^{0}C. Nevertheless, a more systematic experimental study is needed to clarify the sources of high temperature deformation mechanisms, including the microstructure evolution.

The present investigation includes the calibration of the model parameters for the cho-

Table 3.1: Material parameters for oxygen transport in Ti-6Al-2Sn-4Zr-2Mo-0.1Si.

D_0 [mm^2/s]	c_∞ [%]	Q [kJ/mole]	ω_c	ω_{ec}	a	$\bar{V}_O$ [cm^3/mole]
5.397	0.15	184.8	0.1	0.7	3.56	3.5

sen titanium alloy based on experimental data (Section 3.4.1), and characterization of the coupling effects between the oxygen embrittlement, viscous and deformation mechanisms (Section 3.4.2).

3.4.1 Model calibration

Model calibration includes the identification of the material properties for oxygen transport into the titanium alloy, the viscoelastic and viscoplastic properties of the alloy as well as the properties that characterize the coupling between the transport and deformation processes. Model calibration is performed based on the experimental data conducted at the Air Force Research Laboratory, as well as the data available in the literature. The calibrations that include multiple model parameters were conducted using the least squares minimization of the pertinent objective function, defined as the discrepancy between the experimental observable (e.g., stress-strain curve, relaxation curve, etc.) and the results of the numerical simulations.

The calibrated oxygen transport model parameters are summarized in Table 3.1. The pre-exponential constant, D_0, and the activation energy, Q, are experimentally determined as 5.397 mm^2/s and 184.8 kJ/mole, respectively. These parameters are consistent with prior experimental investigations [41, 42] as well. The bulk oxygen concentration in the titanium alloy is provided by the manufacturer (Timet) as 0.15%. The partial molar volume of oxygen in the alloy is taken to be 3.5 cm^3/mole, same as that reported by Ref. [43] for pure titanium. The parameters that characterize the effect of mechanical damage on oxygen diffusivity, ω_c, ω_{ec} and a are consistent with the reported values based on the percolation theory [44, 45].

The material properties that describe the mechanical behavior are summarized in Ta-

Table 3.2: Material parameters for viscoplastic deformation of Ti-6Al-2Sn-4Zr-2Mo-0.1Si.

ν	E_0 [GPa]	γ [MPa/h]	$\dot{\varepsilon}^0$ [1/s]	α [1/°C]	ϑ [1/%c]	A [MPa]
0.32	120.8	2000.0	1.0	7.7e-6	1.1e-3	895.0
B [MPa]	F [MPa/%c]	n	m	c_{crit} [%]	T_β [°C]	q_{ref}
125.0	140.0	0.2	1.35	4.5	1000.0	1.0
$\bar{q}$	D_1^∞	D_1^α	D_5	D_6	M	K_e
2.7586	0.1676	5.0e-3	9.5e-7	23.25	5	0.0
K_1	K_2	K_3	K_4	K_5	ξ_1 [h]	ξ_2 [h]
0.5	0.2	0.15	0.1	0.05	4.5e4	4.667e5
ξ_3 [h]	ξ_4 [h]	ξ_5 [h]	C_1	C_2		
4.167e6	4.167e7	4.167e8	-6.3714	-1094.75		

ble 3.2. The temperature effect on the elastic and plastic responses are calibrated based on a series of uniaxial tensile experiments conducted at room temperature, 538^0C, 593^0C and 650^0C, from which the temperature variation of Young's modulus, Poisson's ratio, yield strength, failure strain and strain hardening variable are calibrated. The loading rate effect is investigated at room temperature only, where the viscosity at room temperature was determined. The loading rate experiment conducted at room temperature shows little difference between the fast and slow loading tests. The rate effect is typically stronger at elevated temperatures and the discrepancy between the fast and slow loading tests could be more pronounced. Literature on the quantified effect of load rate on the yield strength at high temperature for Ti-6242S is quite limited and additional experimental data to fully quantify the rate effects is needed. The simulated stress-strain response at high temperatures using the calibrated properties are compared to the experimental measurements in Fig. 3.3. The necking process dictated by large structural deformation is not incorporated into the proposed model and currently the model is limited to small deformation theory. No attempt was therefore made to calibrate the post-peak behavior of the engineering curve. The oxygen induced hardening parameter, F, is calibrated based on the microhardness experiments conducted on oxygen-exposed specimens [19]. The embrittlement parameter, D_1^α, is chosen such that the ductility nearly vanishes at the critical oxygen concentration

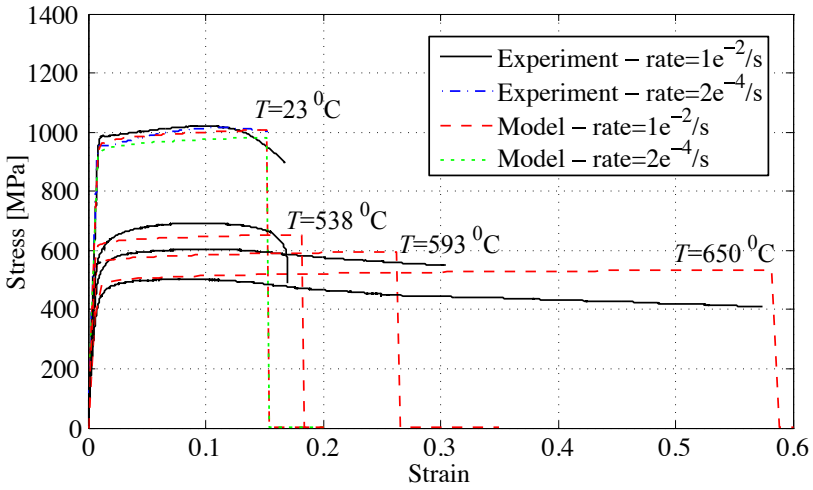

Figure 3.3: The stress-strain response of Ti-6Al-2Sn-4Zr-2Mo-0.1Si at room and elevated temperatures.

c_{crit}, taken to be 4.5%. The resulting constitutive response as a function of concentration are illustrated in Figs. 3.4 and 3.5 at room temperature and 593^{0}C, respectively.

The viscoplastic parameters including the fluidity parameter, γ, the viscoplastic hardening parameters, q_0 and q^*, and the viscoelastic parameters including the number of Maxwell elements, M, the Prony series coefficients, K_m and ξ_m ($m = 1,\ldots,M$), and the temperature dependence parameters, C_1 and C_2, are calibrated based on stress relaxation tests conducted at temperatures of 593^{0}C and 650^{0}C. The number of Maxwell elements is chosen as 5, the minimum number necessary to accurately evaluate the stress relaxation response at both short and long time scales. Figure 3.6 compares the experimentally observed and simulated short term relaxation behavior at temperatures of 593^{0}C and 650^{0}C under the constant strain magnitude of 3.5%. Within the first 40 seconds of relaxation, both viscoelastic and viscoplastic relaxation processes are active since the specimens were loaded to stress levels beyond the static yield strength. Figures 3.7 and 3.8 compare the simulated and observed long-term relaxation behavior up to 100 hours. The long-term relaxation behavior is governed by the viscoelastic component of the model only, as the stress drops below the temperature dependent static yield stress. A near complete relaxation is observed at 100 hours of exposure of the specimen to 650^{0}C, whereas the stress asymptotes at ap-

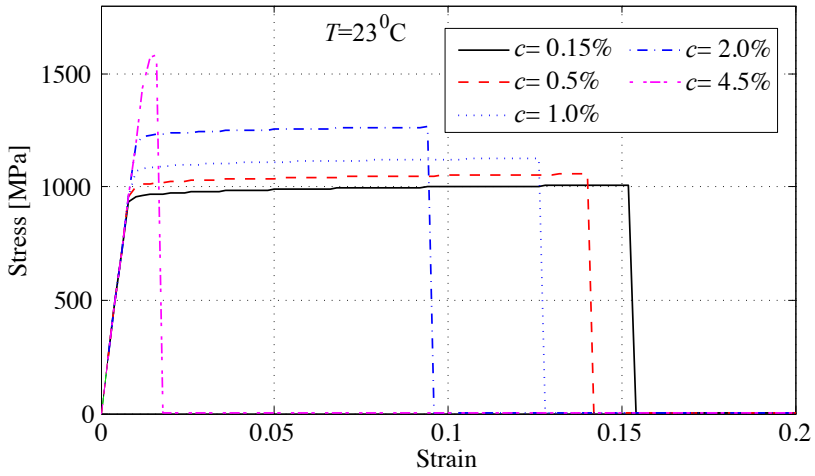

Figure 3.4: The stress-strain response of Ti-6Al-2Sn-4Zr-2Mo-0.1Si with varying oxygen content at room temperature.

proximately 6.25 MPa when exposed to 593^0C. In both cases, the model is in excellent agreement with the observed relaxation behavior. Further experimental investigation of the microstructure during the combined loading and high temperature exposure would provide additional information on the microstructural origins of the relaxation process. The relaxation experiments included in this study were uninterrupted and the possible microstructure evolution was therefore could not be observed.

3.4.2 Response under combined thermo-mechanical environment

The calibrated transport-deformation model is employed to investigate the combined environment response of Ti-6242S. The investigations focused on the coupling mechanisms between oxygen transport, relaxation and deformation behavior. The proposed numerical investigations are focused on the combined environment setup of the experiments conducted by Peters *et al.* [18]. Figure 3.9 illustrates the overview of the experimental procedure. Each specimen was displacement-loaded using four-point bend (4PB) apparatus. The specimens were consequently subjected to constant elevated temperature at their loaded state. The duration of high temperature exposure was 100 hours. The specimens were then cooled back to the room temperature and tested using a three-point bend (3PB)

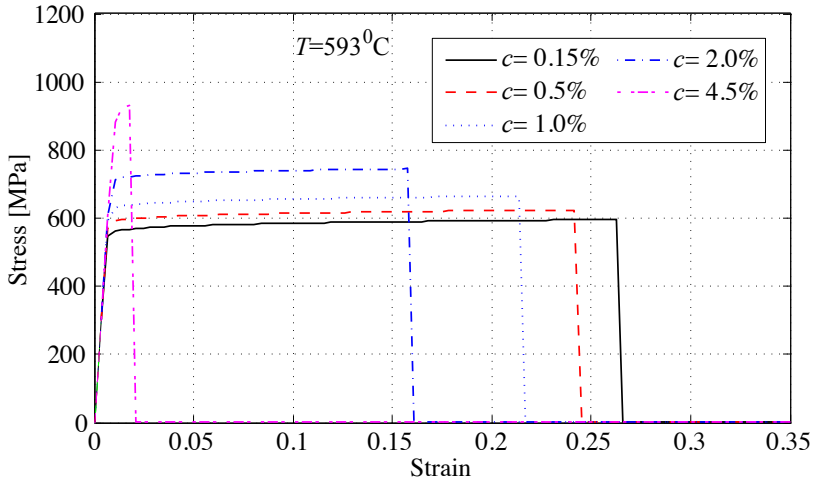

Figure 3.5: The stress-strain response of Ti-6Al-2Sn-4Zr-2Mo-0.1Si with varying oxygen content at 593 ^{0}C.

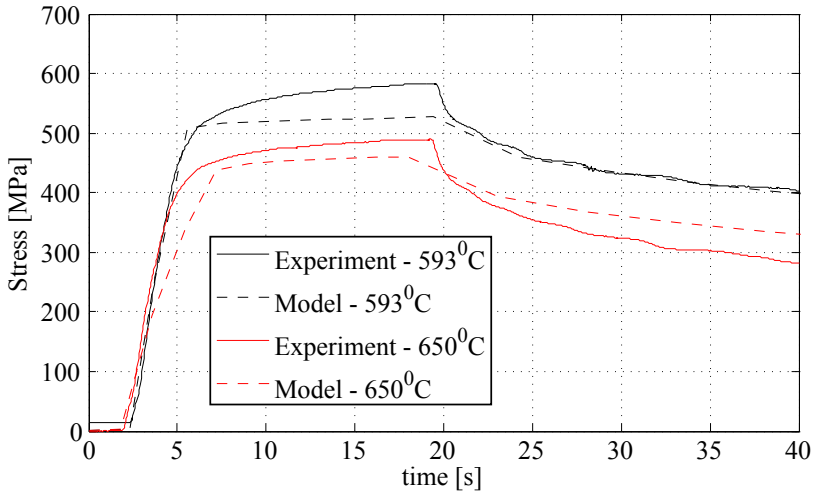

Figure 3.6: The stress relaxation test of Ti-6Al-2Sn-4Zr-2Mo-0.1Si at 593^{0}C and 650^{0}C for 40 seconds.

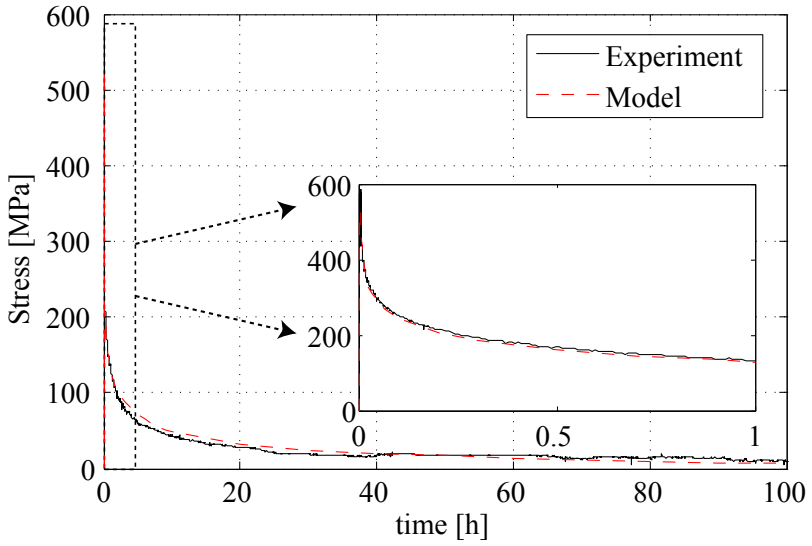

Figure 3.7: The stress relaxation test of Ti-6Al-2Sn-4Zr-2Mo-0.1Si at 593^0C for 100 hrs.

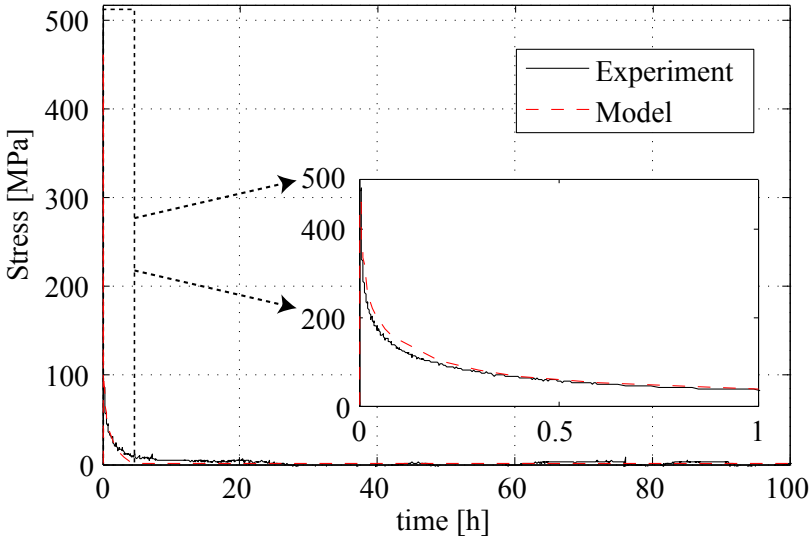

Figure 3.8: The stress relaxation test of Ti-6Al-2Sn-4Zr-2Mo-0.1Si at 650^0C for 100 hrs.

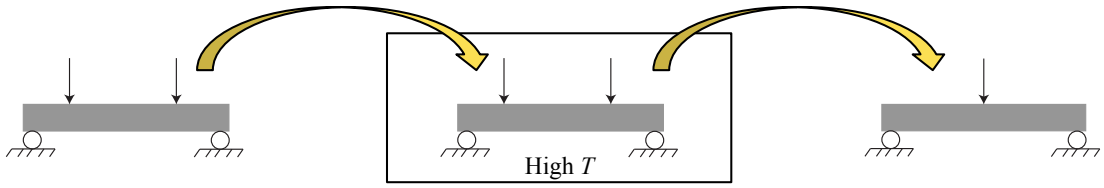

Figure 3.9: Coupled transport- deformation experiments procedure

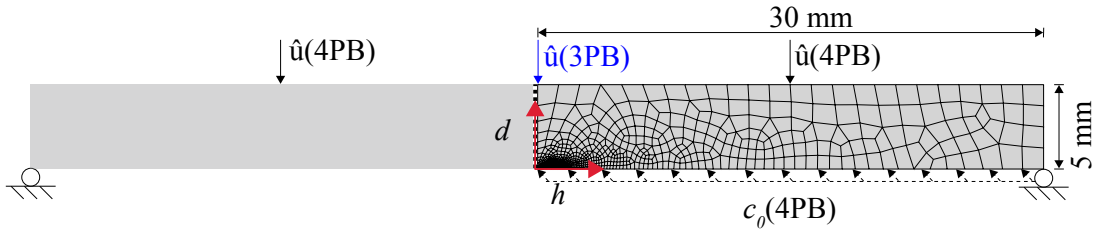

Figure 3.10: Geometry, boundary condition and finite element mesh of the 4 point bend and the 3 point bend configurations.

setup. Four different scenarios were considered: specimens subjected to 0.75mm (low amplitude loading) or 1.5mm (high amplitude loading) maximum displacement in 4PB apparatus and exposed to 450^0C and 550^0C in the heating chamber.

Figure 3.10 shows the geometry, boundary conditions and the finite element discretization of the numerical specimen. Plane-strain conditions were assumed. Only half of the specimen is discretized due to the symmetry of the geometry and the loading conditions. For computational efficiency, the focus is kept on the tension (bottom) side of the specimen. The bottom-left corner of the specimen has very fine resolution with element size of approximately 0.2μm. The oxygen ingress is applied at the tension side only since the oxygen induced tension cracks are more critical than the compression observed at the top surface.

Table 3.3 summarizes the maximum stress achieved immediately after loading in specimens subjected to four-point bending at elevated temperatures. The computed values are compared to theoretical maximum stress provided in Ref. [18]. The computed and theoretical stress magnitudes are in reasonable agreement with each other, albeit some differences particularly at high loading amplitude. The discrepancy is attributed to the fact that the the-

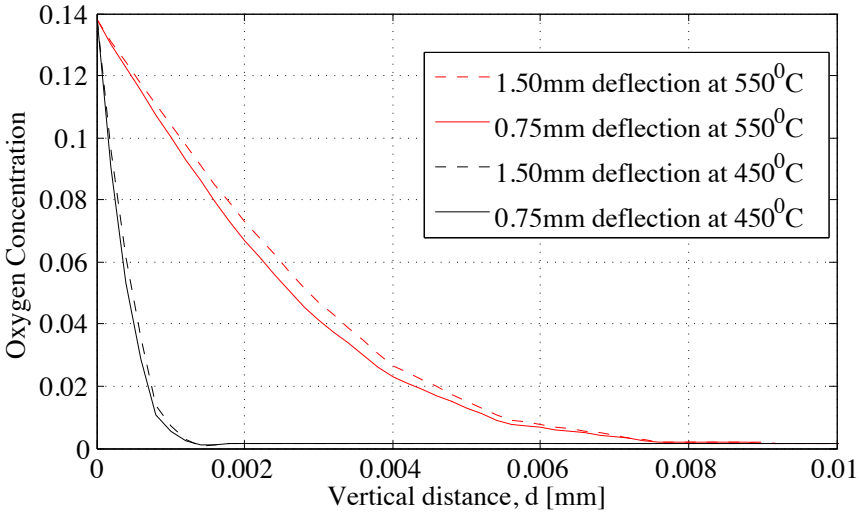

Figure 3.11: Oxygen concentration along the depth from the tensile surface.

oretical values do not consider relaxation during the loading process. The low amplitude loading remains within the elastic range at both 450^{0}C and 550^{0}C. Figure 3.11 shows the oxygen concentration distribution measured from the center of the bottom surface along the vertical direction towards the interior for all four configurations after the 100 hour high temperature exposure. The oxygen content of the ambient environment is taken to be 13.8% wt. [19], which was applied as the concentration boundary condition at the tension side of the specimen. I note that the oxygen uptake capacity of the alloy is approximately 7% wt. beyond which the oxide layer is formed [15]. Typically, the size of the oxide layer is significantly smaller than the oxygen enriched case and the effects of oxide formation are neglected. Figure 3.11 shows that the presence of loading has a nominal effect on the oxygen ingress in this case, which is consistent with the experimental observations. The thicknesses of the oxygen enriched layers are 3.162 μm, 2.868 μm, 0.588 μm and 0.515 μm for the high load - 550^{0}C, low load - 550^{0}C, high load - 450^{0}C and low load - 450^{0}C cases, respectively. Since there is no significant inelastic strain in the low amplitude load cases, the mechanical state does not affect the oxygen ingress.

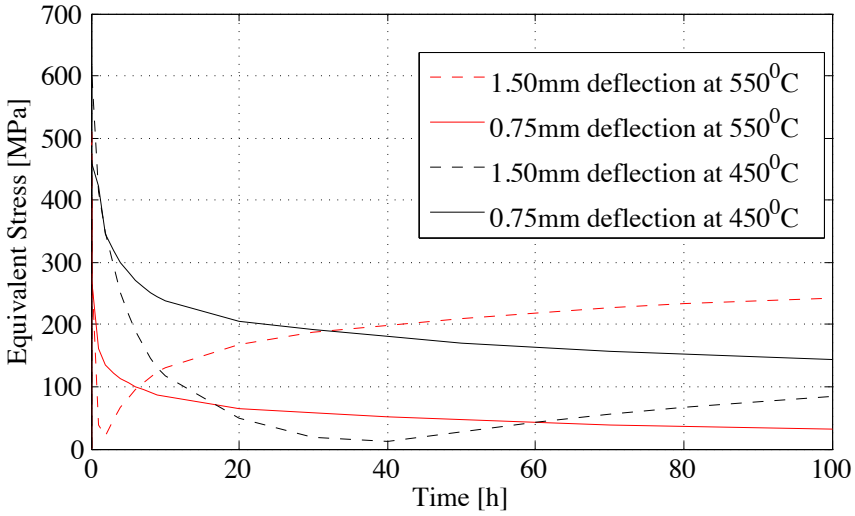

Figure 3.12: Equivalent stress variation in 4 point bending tests for 100 h at the center of the tensile surface.

3.4.2.1 Relaxation and oxygen ingress under high temperature exposure

Since the four point bending tests were performed at high temperatures under displacement control, significant stress relaxation is expected. The relaxation process interacts with both the transport of oxygen and the resulting stress state. Figure 3.12 shows the equivalent stress history at the bottom center of the specimen for the four test conditions. The specimens loaded at low applied displacement magnitude display a typical relaxation behavior. Since no plastic deformation is predicted at low amplitude loading, the relaxation is entirely viscoelastic. At high amplitude loading, a very different stress evolution is observed at both temperatures, in which an exponential relaxation is followed by a stress recovery phase. For instance, at 550^{0}C, the stress drops from the peak value of 513 MPa to 38 MPa after 1 hour and steadily increase to 243 MPa at 100 hours of exposure. At 450^{0}C, the stress recovery behavior is similar to the 550^{0}C case, but the recovery is less severe.

In order to interpret the stress recovery observed in plastically loaded specimens, the numerical simulations were extended up to 2000 hours of high temperature exposure, at which the specimens reach full relaxation or steady state. Figure 3.13 depicts the equivalent stress distribution of the four point bending specimens along the vertical line measured

from the bottom-center towards the top (shown as vector d in Fig. 3.10) at a number of time instances. When the midspan deflection is set to 0.75 mm (i.e., low amplitude loading) the stresses relax uniformly as the process is purely viscoelastic as shown in Fig. 3.13a,b. The specimen subjected to 550^0C displays complete relaxation at the exposure time of 2000 hr. The slight stress asymmetry between the compression and tension sides is due to the biased meshing as well as the oxygen ingress imposed on the tension side. When the specimens are plastically loaded with midspan deflection of 1.5mm, a significantly different time dependent behavior is observed as shown in Fig. 3.13c,d. The loading clearly induces plastic deformation near the compression and tension sides of the specimens with approximately 1 mm thickness. Within the interior of the specimens, the deformation remains viscoelastic. Initially, the plastically loaded region induces a faster relaxation compared to the elastically loaded region since both the viscoelastic and viscoplastic stress relaxation mechanisms are active in the plastically loaded region. The uneven relaxation moves the peak stress towards the interior of the specimen. The relaxation induced stress distribution is resisted by the equilibrium process, which leads to higher stresses at the outer faces of the specimen at longer times. At the steady state, significant residual stresses are observed at the plastically loaded outer faces of the specimens. It is important to note that the stress recovery process is limited to the outer faces of the specimen and despite the stress recovery mechanism, the overall energy of the specimen monotonically reduces during the exposure duration since the viscous dissipation process is not recoverable. Similar behavior is observed in the specimens subjected to 550^0C and 450^0C environments. The relaxation and stress recovery naturally occurs at a faster rate at 550^0C (Fig. 3.13c) compared to 450^0C (Fig. 3.13d). The time evolution of the stress contours within the four-point bending tests under 550^0C exposure for the elastically and plastically loaded specimens are shown in Fig. 3.14. The spatial evolution of the equivalent stress in the plastically loaded specimens are highly nonuniform in contrast to the elastically loaded specimens, whose stress distribution remains nearly identical with monotonically decreasing magnitude.

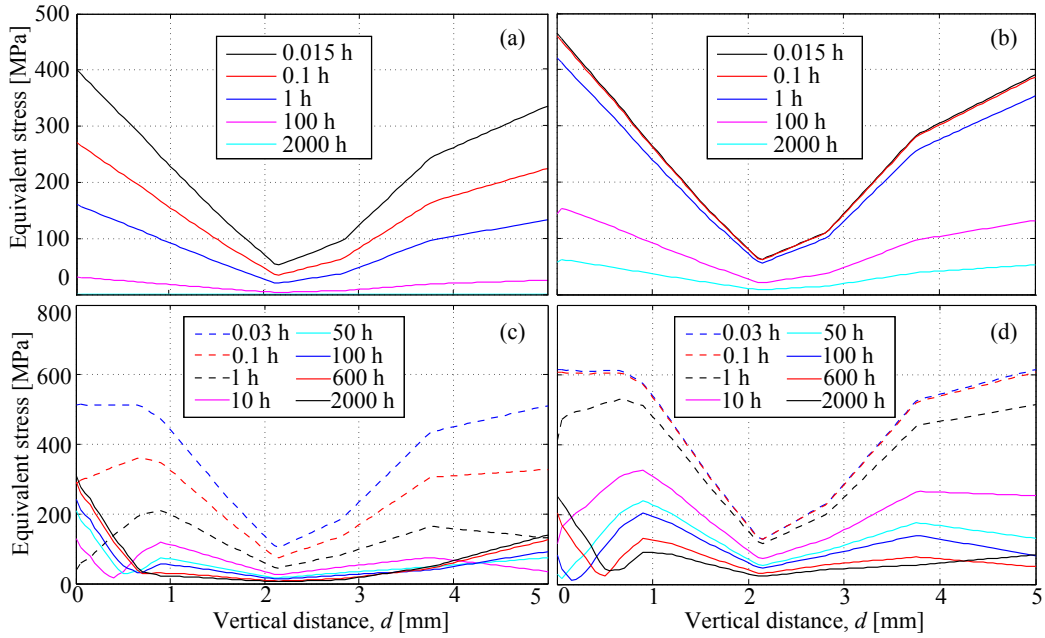

Figure 3.13: Equivalent stress along the depth from the tensile surface: (a) 0.75 mm loading at 550^0C; (b) 0.75 mm loading at 450^0C; (c) 1.5 mm loading at 550^0C; and (d) 1.5 mm loading at 450^0C.

Table 3.3: Influence of oxidation on cracking at room temperature in 3-P bending.

		4PB		3PB	
T (^{0}C)	D (mm)	σ_{max} [MPa] Theoretical [18]	σ_{max} [MPa] Model	[cracks/mm] Experiment	[cracks/mm] Model
450	0.75	419.00	464.64	-	18.18
450	1.50	$>644.20(\sigma_{p0.2})$	619.80	20.00	18.18±9.1%
550	0.75	390.00	400.66	22.36	18.18±18.7%
550	1.50	$>578.80(\sigma_{p0.2})$	516.73	8.70	10.26±17.9%

3.4.2.2 Three-Point Bend Response of Exposed Specimens

The numerical specimens subjected to 100 hours of high temperature exposure at the loaded state are unloaded and cooled to the room temperature prior to further testing using the three-point bend test setup. This procedure mimics the experimental protocol followed by Peters *et al.* [18]. A midpoint vertical deflection of up to 3.6 mm and 4.8 mm was applied to the specimens exposed to 550^0C and 450^0C environment, respectively.

Figure 3.15 displays the damage propagation during the 3PB testing of the specimen

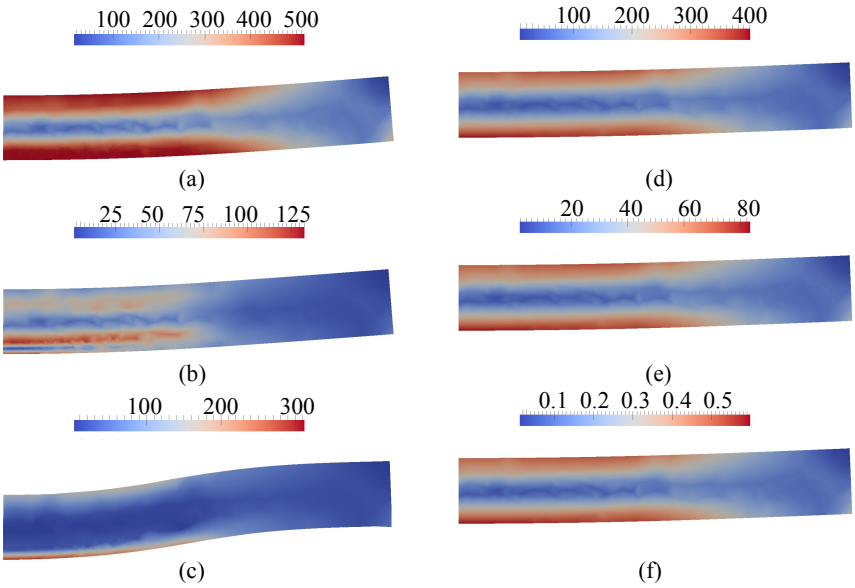

Figure 3.14: Equivalent stress contour of 4 point bending specimen at 550^0C with: (a) 1.50 mm midspan deflection at 0.03 hr; (b) 1.50 mm midspan deflection at 10 hrs; c) 1.50 mm midspan deflection at 2000 hrs; (d) 0.75 mm midspan deflection at 0.015 hr; (e) 0.75 mm midspan deflection at 10 hrs; f) 0.75 mm midspan deflection at 2000 hrs;

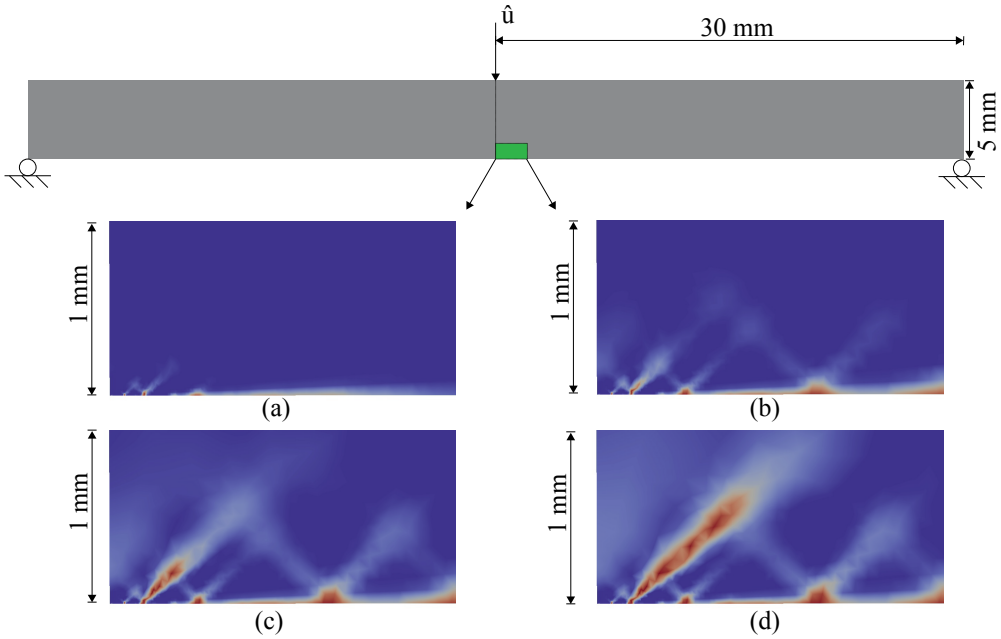

Figure 3.15: Three point bending damage at applied displacement of: (a) 2.4 mm; (b) 2.9 mm; c) 3.3 mm; (d) 3.7 mm of the specimen oxidized with 0.75 mm deflection at 450^0C.

that was exposed to 450 ^{0}C under the midspan deflection of 0.75 mm. The damage contours are from a 2mm by 1mm region near the central section of the tensile surface. A thin surface layer of 0.515 μm thickness has reached or exceeded c_{crit} during the exposure process, within which the early onset of damage propagation is initiated. The damage progressively propagates towards the interior of the specimen along the shear path, reaching a length of 0.8 mm at the applied midspan deflection of 3.7 mm. The damage evolution during the 3PB testing of the specimen that was exposed to 450 ^{0}C under the midspan deflection of 1.5 mm is very similar, which indicates that the small change in the surface oxygen concentration has insignificant effect on the mechanical performance. Figure 3.16 compares the damage state in the three-point bend specimens subjected to 3.6 mm midspan deflection, that were previously exposed to 550 ^{0}C under the midspan deflection of 0.75 mm and 1.5 mm. The specimen that was previously exposed to high temperature while viscoelastically loaded developed a slightly larger damage region compared to the viscoplastically loaded specimen. The difference between the oxygen enriched region thicknesses between the two specimens prior to the three-point bending is nominal, whereas the initial stress distributions are significantly different owing to the stress recovery process discussed above. The discrepancy between the damage patterns is attributed to the different stress states of the specimens prior to loading in the three-point bend apparatus. In both cases shown in Fig. 3.16, the cracks propagate at an angle of approximately 41^0-45^0. Experimental data on the direction of the crack paths is not available for validation of the path of crack propagation, which may shed further light on the microstructural origins of the failure behavior.

In the current chapter, the scalar damage variable affects the behavior only at the onset of the state of failure (i.e., $\omega = 1$). At failure, the residual stiffness of the corresponding element is set to a small fraction of the elastic stiffness of the material, which accounts for failure induced relaxation and load redistribution. The stiffness relaxation introduced by this approach is known to induce mesh-dependency [46, 47]. Introduction of advection-diffusion terms was shown to regularize mesh dependency in certain conditions [48, 49].

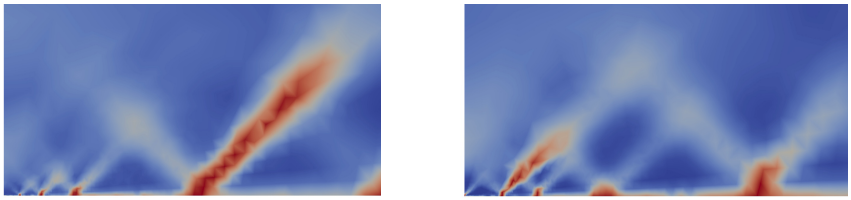

(a) (b)

Figure 3.16: Three point bending damage at applied displacement of 3.6 mm of the specimen oxidized at 550^0C with deflection: (a) 0.75 mm; (b) 1.50 mm.

Through a similar mechanism, the coupling between the oxygen transport and the deformation problem could pose as localization limiter of the deformation problem. The results in this study indicate that the mesh localization phenomenon is not observed and the damage zone thickness remains larger than the mesh size ($3\times$ the element size) in the example problems studied herein. The current chapter does not include a thorough mesh localization investigation and further study of this point is needed to assess whether realistic oxygen diffusion rates could act as localization limiter for the deformation problem.

Figure 3.17 displays the three point bending damage profiles along the tensile surface for specimens previously exposed to 450^0C and 550^0C. The three point bending test generates nearly identical damage distribution along the tensile surface within the specimens previously subjected to 450^0C regardless of the four point bend loading amplitude as shown in Fig. 3.17a-c. In contrast, the specimen previously subjected to 550^0C and low four point bend loading amplitude has a significantly different surface damage pattern compared to the specimen previously subjected to 550^0C and high four point bend loading amplitude as shown in Fig. 3.17d-f. One key difference is the change in the periodic crack spacing, which reduces from approximately 18 cracks/mm to 10 cracks/mm, which is consistent with the experimentally observed crack spacing of 22 cracks/mm and 9 cracks/mm, respectively as summarized in Table 3.3. The thickness of the brittle surface layer is increased with increasing temperature because of the higher diffusivity of oxygen at elevated temperatures. The relationship between the spacing between the periodic embrittlement-induced

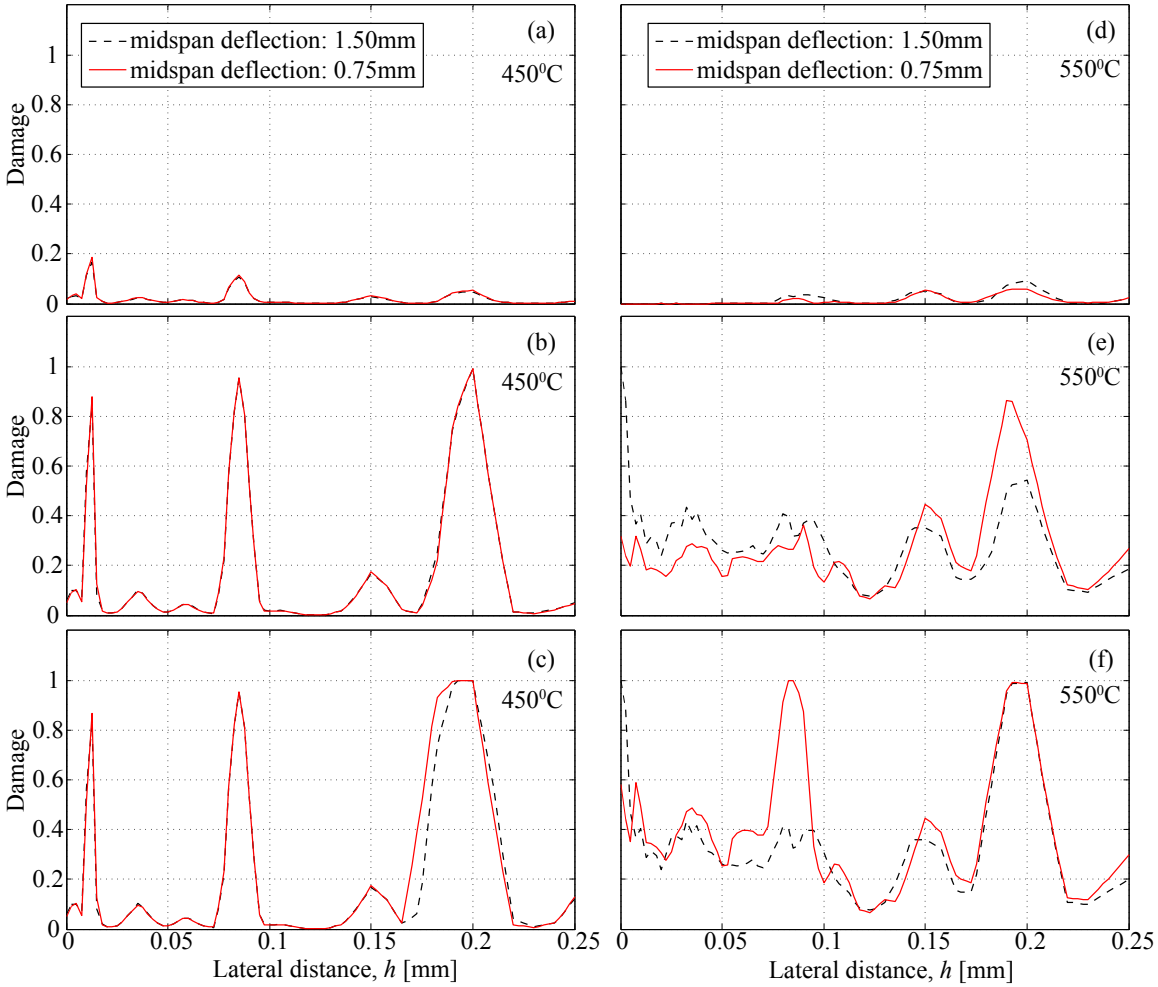

Figure 3.17: 3 point bending damage profile of the specimen oxidized at 450^{0}C along tensile surface at applied displacement of: (a) 1.4 mm; (b) 2.1 mm; (c) 3.7 mm; at 550^{0}C along tensile surface at applied displacement of (d) 1.35 mm; (e) 1.875 mm; (f) 2.475 mm.

surface cracks and the thickness of the brittle surface layer was investigated by Hutchinson *et al.* [50], Thoulesset *al.* [51] and others. The saturation crack spacing is proportional to the crack length to the first order of approximation. This relationship is due to the increased fracture process zone around the longer surface cracks compared to the shorter cracks. Under a critical stress magnitude, cracks start to form on the brittle layer and the stresses at the ligament around the crack relax. With increase in loading, more cracks progressively form until the saturation is reached where the shear stress at the interface of the brittle case and the substrate reaches its maximum allowable [19].

3.5 Conclusion

This chapter provided a viscoelastic-viscoplastic model to describe the mechanical response of titanium structures operating under high temperature and mechanical loading. The effects of temperature-activated oxygen ingress into the structure and consequent embrittlement and hardening are included by considering a fully coupled transport model to the proposed deformation model. A suite of experiments on a high temperature alloy, Ti-6242S, has been employed to calibrate the model parameters and to understand the coupled mechanisms of oxygen ingress induced embrittlement, viscous relaxation/creep and deformation.

The experimental and the numerical investigations suggest that directly quantifying the effect of stress or strain state on the oxygen ingress rate is not straightforward. In a displacement-controlled setup, viscoelastic relaxation quickly reduces the internal stress, and hence, the load effect on oxygen ingress. In contrast, the effect of small changes in the oxygen ingress rate due to loading may be significant for cyclic loading cases, where the interactions of loading and the oxygen ingress rate may have a cumulative effect on crack initiation. Despite such difficulties, the proposed model accurately captures the coupled deformation-relaxation-embrittlement response at high temperature environments.

The experimental data employed in this chapter to calibrate and validate the relaxation

behavior is not exhaustive. While, it is beyond the scope of this chapter to perform a comprehensive suite of experiments to fully characterize and connect the proposed model to the microstructural origins of relaxation, the need to further testing on creep-relaxation regime including a detailed microstructure study is important to link the relaxation behavior to the material microstructure, which is quite complex for Ti-6242S. A more systematic experimental study could clarify the sources of relaxation, and point to the effect of microstructure evolution on creep and relaxation, which is not included in this study.

From the modeling perspective, further improvements to the proposed computational model are necessary to understand and predict the behavior of titanium alloys operating in high thermo-mechanical environments. First, the model will be extended to describe the cyclic behavior to accurately predict initiation of fatigue damage, which is significantly affected by oxygen ingress. It is also clear that the oxygen ingress is localized within a very small boundary region of the structure with a thickness of the order of a few grain diameters. Accurate characterization of localized deformation and failure within this zone necessitates very fine resolution along the exposed surfaces [35, 52]. Straightforward biased meshing with such a refined resolution within a realistic structural component is not computationally feasible. A multi resolution modeling approach is necessary to accurately capture both the local (i.e., around the boundaries) and global (i.e., throughout the structure) response. Future research will focus on the development of such a multi resolution modeling approach.

Chapter 4

MULTI-YIELD SURFACE MODELING OF VISCOPLASTIC MATERIALS

4.1 Introduction

Modeling cyclic response in the presence of material nonlinearity is critical for many engineering applications ranging from response of soils subjected to earthquake excitations to metals subjected to low cycle fatigue. I am particularly concerned with modeling and prediction of the cyclic response in aerospace structures made of titanium and other alloys operating in hypersonic conditions in the presence of high temperatures.

Modeling the cyclic response of metals at high temperature has seen tremendous developments in the past few decades. Thorough surveys of literature have been presented by McDowell [53], Chaboche [54], Lemaitre [55] among many others. Beyond the crystal plasticity based cyclic deformation models (e.g., [56, 57, 58]), the majority of phenomenological plasticity models relies on a single yield surface, typically defined in the stress space as well as evolution laws, often derived based on the yield surface. Those deformation mechanisms pertinent to the high temperature environment such as dynamic and or static recovery are incorporated based on complex functional relationships into the evolution functions of the internal state variables. The simplest model is the linear kinematic hardening introduced by Prager *et al.* [59], where a linear stress-strain response is assumed in the plastic deformation. A modified model consists of a dynamic recovery term was proposed by Armstrong *et al.* [60] to generalize the model to a more variety of materials, where the evolution of backstress is exponential for a monotonic uniaxial loading. More modified models were presented by Watanabe *et al.* [61] to generate a better description of the onset of the plastic flow by introducing a superposition of backstress.

An alternative formulation, multi-yield surface plasticity, was proposed by Mroz *et al.* [62] and further developed in the field of soil mechanics(e.g., [63, 64, 65]). In multi-

yield surface plasticity, multiple, non-intersecting yield surfaces define the evolution of plastic flow. The primary advantage of this approach is that the behavior is approximated as linearly hardening between two neighboring yield surfaces, leading to a piecewise linear approximation of the plastic flow. The evolution equations are therefore very simple and the accuracy is controlled by number of defined yield surfaces. A modified multi-yield surface model was proposed by Elgamal *et al.* [66, 67], in order to reduce the computational cost by redefining the backstress translation direction. The available literature in multi-yield surface plasticity focuses on the rate independent behavior, where dissipation was introduced as structural damping. To the best of authors' knowledge, no attempt has been made so far to introduce rate effects at the material level. Other closely linked modeling approaches such as bounding surface plasticity[68, 69, 70, 53, 71, 72], which is based on two yield surfaces have also been proposed. Simo[73] explored the idea of using multiple (intersecting) hypersurfaces in the stress space to describe complex yield surface shapes in the context of single yield surface plasticity.

In this chapter, a multi-yield surface viscoplastic model is proposed to study the cyclic response of alloys. The proposed approach builds on the model by Mroz *et al.* [62] by extending it to account for viscoplastic process, which is critical to the response characterization of metals at high temperatures. The model is implemented using a mixed finite element approach, in which displacement and pressure are evaluated as independent unknowns [74]. The multi-yield surface viscoplasticity is incorporated into a viscoelastic-viscoplastic constitutive model to describe the response of titanium alloys operating at high temperature environments. The computational model was validated against experiments conducted at a variety of temperatures. The main contribution of this chapter is the extension of the multi-yield surface plasticity approach to the viscoplastic regime. The effect of rate dependent behavior on the evolution of the backstress is induced without violating Mroz's collinearity rule. A nonlinear kinematic hardening law is introduced by incorporating linear kinematic hardening [59] and multi-yield surface plasticity.

The remainder of this chapter is organized as follows: Section 4.2 introduces the background and the basic theory of the multi-yield surface plasticity. The proposed multi-yield surface viscoplasticity model is explained in Section 4.3. Section 4.4 presented the viscoelastic-viscoplastic constitutive deformation equation systems. Section 4.5 describes the finite element implementation of the multi-yield surface viscoplasticity deformation model. Section 4.6 details the numerical investigation of titanium alloy, Ti-6242S, at various temperatures. The calibration of the proposed model is based on an independent set of experimental data and a detailed analysis of the cyclic characteristics of specimens is included in this section. The conclusions and future research directions are provided in Section 4.6.2.

4.2 Overview of multi-yield surface plasticity

In this section, Mroz's multi-yield surface plasticity model[62], which is the starting point of the proposed model, is summarized. In Mroz's formulation, a series of yield surfaces are defined, each of which is associated with a unique plastic moduli, a yield stress and a backstress to describe piecewise linear, elasto-plastic, rate independent constitutive behavior.

Consider M yield surfaces to approximate the elastoplastic behavior as illustrated in Fig.4.1. The yield surfaces are taken to be initially concentric pointing to initial isotropy of yielding. The yield surfaces are ordered according to their sizes in the π-plane as shown in Fig.4.1a. For simplicity, each yield surface is modeled using the Von-Mises yield function (Fig.4.1b). An arbitrary yield function is expressed as:

$$f^m = \sqrt{3}\bar{s}^m - \sigma_Y^m \leqslant 0; \quad m = 1,2,...,M \tag{4.1}$$

where, σ_Y^m is the flow stress of the mth yield surface; $f^m(\boldsymbol{s}, \boldsymbol{\alpha}^m; \sigma_Y^m)$ the mth yield function; $\bar{s}^m$ is the second invariant of the difference between the deviatoric stress $\mathbf{s}$ and the backstress

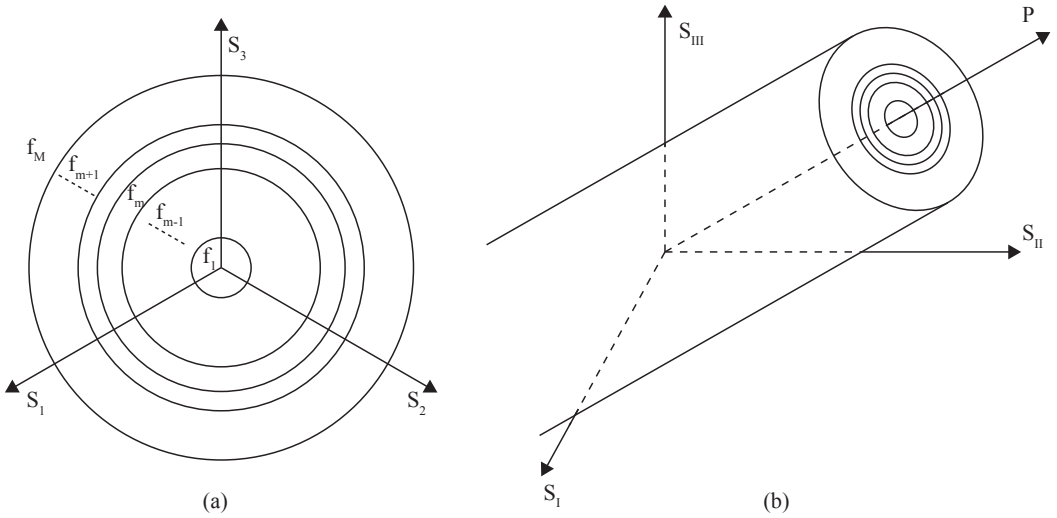

Figure 4.1: Yield surfaces of multi-yield-surface J2 plasticity model in (a) deviatoric space; (b) principal space.

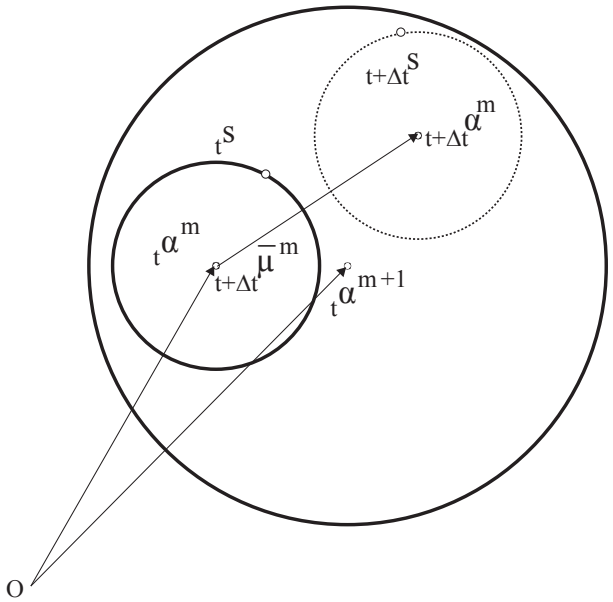

Figure 4.2: Mroz deviatoric hardening rule.

α^m of the mth yield surface:

$$\bar{s}^m = \sqrt{\frac{1}{2}\left(s_{ij} - \alpha_{ij}^m\right)\left(s_{ij} - \alpha_{ij}^m\right)} \tag{4.2}$$

In what follows, I adopt the index notation in the problem formulation (i.e., $i = 1, ..., n_{\text{sd}}$), where n_{sd} is the number of spatial dimensions. Repeated indices of the spatial dimensions indicate summation unless otherwise stated. A subscript followed by a comma indicates partial derivative (i.e., $f_{,i} = \partial f / \partial x_i$) and the dummy index m is reserved to indicate the pertinent variable associated with the mth yield surfce.

In multi-yield surface plasticity, a pure kinematic hardening rule is typically employed. As shown in Fig.4.1, each yield surface undergoes rigid body translation towed by the deviatoric stress tensor. The shifting of the yield surfaces has to be performed such that none of the yield surfaces intersect another (i.e., collinearity condition [62]). Let $\hat{m}$ denote the current active yield surface at an arbitrary equilibrium state, defined as follows:

$$f^m \geqslant 0 \ \forall \ 1 < m \leqslant \hat{m}; \ \text{ and } \ f^{\hat{m}+1} < 0 \tag{4.3}$$

The associative flow rule is used to define the evolution of the plastic strain, which follows the direction of the outward normal to the current active yield surface at the stress point[67, 65]:

$$Q_{ij}^{\hat{m}} = \frac{1}{Q^{\hat{m}}} \frac{\partial f^{\hat{m}}}{\partial s_{ij}} \tag{4.4}$$

where:

$$Q^{\hat{m}} = \sqrt{\frac{\partial f^{\hat{m}}}{\partial s_{ij}} \frac{\partial f^{\hat{m}}}{\partial s_{ij}}} \tag{4.5}$$

Employing the standard complementary and consistency conditions defined on the current active yield surface, the magnitude of the slip rate is computed as:

$$L^{\hat{m}} = \frac{1}{H^{\hat{m}}} Q_{ij}^{\hat{m}} \dot{s}_{ij} \tag{4.6}$$

Where $H^{\hat{m}}$ is the plastic modulus associated with the current active yield surface. Then the evolution of plastic strain $\dot{\varepsilon}^p$ is defined as:

$$\dot{\varepsilon}^p_{ij} = \langle L_{\hat{m}} \rangle \, Q_{\hat{m}_{ij}} \tag{4.7}$$

Where, $\langle \cdot \rangle$ denotes the Macaulay brackets (i.e., $\langle \cdot \rangle = ((\cdot) + |\cdot|)/2$).

Pure deviatoric kinematic hardening rule is adopted as:

$$\dot{\alpha}^{\hat{m}} = |\dot{\alpha}^{\hat{m}}| \mu^{\hat{m}} \tag{4.8}$$

where the magnitude of the translation $|\dot{\alpha}^{\hat{m}}|$ of the current active yield surface satisfies the consistency condition and the translation unit direction $\mu_{\hat{m}}$ was proposed by Mroz for elasto-plastic material. As shown in Fig.4.2, where translation tensor $\bar{\mu}^{\hat{m}}_{ij}$ for current active yield surface $\hat{m}$ is defined as:

$$\bar{\mu}^{\hat{m}}_{ij} = \frac{\sigma_Y^{\hat{m}+1}}{\sigma_Y^{\hat{m}}} \left(s_{ij} - \alpha^{\hat{m}}_{ij} \right) - \left(s_{ij} - \alpha^{\hat{m}+1}_{ij} \right) \tag{4.9}$$

and the normalized direction is:

$$\mu^{\hat{m}}_{ij} = \frac{\bar{\mu}^{\hat{m}}_{ij}}{\| \bar{\mu}^{\hat{m}}_{ij} \|} \tag{4.10}$$

Which is employed to avoid any overlapping between yield surface $\hat{m}$ and $\hat{m}+1$. With the completion of the translation of the current active yield surface $\hat{m}$, yield surface $\hat{m}$-1 becomes the new active yield surface and repeat the translation process. Eventually all the yield surfaces will be translated tangent to each other at the current deviatoric stress point s.

4.3 Multi-yield surface viscoplasticity

In this section, I propose a new formulation that extends the multi-yield surface modeling to viscoplasticity. The formulation presented here extends Mroz's multi-yield surface plasticity model into rate dependent regime, incorporating kinematic hardening. The relationship between the evolution of backstress and viscoplastic strain is replaced by a general form [75] that guarantees the collinearity condition point out by Mroz *et al.* [62].

I posit the existence of a viscoplastic potential defined as a function of all yield surfaces, i.e., $\Omega\left(f^1, f^2, ..., f^M\right)$. The evolution of viscoplastic strain is expressed as[76]:

$$\dot{\varepsilon}_{ij}^{vp} = \frac{\partial \Omega\left(f^1, f^2, ..., f^M\right)}{\partial \sigma_{ij}} = \frac{\partial \Omega}{\partial f^1}\frac{\partial f^1}{\partial \sigma_{ij}} + \frac{\partial \Omega}{\partial f^2}\frac{\partial f^2}{\partial \sigma_{ij}} + ... + \frac{\partial \Omega}{\partial f^M}\frac{\partial f^M}{\partial \sigma_{ij}} = \sum_{m=1}^{M}\frac{\partial \Omega}{\partial f^m}\frac{\partial f^m}{\partial \sigma_{ij}} \tag{4.11}$$

It is convenient to consider a generalization of the Perzyna law in order to specify the viscoplastic potential. Let the viscoplastic potential consists of the additive sum of the contributions from the viscoplastic potential associated with a single yield surface:

$$\Omega\left(f^1, f^2, ..., f^M\right) = \sum_{m-1}^{M}\Omega^m\left(f^m\right) \tag{4.12}$$

in which:

$$\Omega^m = \frac{\gamma \sigma_Y^m}{q+1} < \frac{f^m}{\sigma_{Y^m}} >^{q+1} \tag{4.13}$$

The resulting flow rule is:

$$\dot{\varepsilon}_{ij}^{vp} = \sum_{m=1}^{M}\gamma < \frac{f^m}{\sigma_{Y^m}} >^q \frac{\partial f^m}{\partial \sigma_{ij}} \tag{4.14}$$

where, γ and q denote the fluidity and viscoplastic hardening parameter, respectively. Substituting Eq.4.1 into Eq.4.14:

$$\frac{\partial f^m}{\partial \sigma_{ij}} = \frac{\sqrt{3}}{2\bar{s}^m}\left(s_{ij} - \alpha_{ij}^m\right) \tag{4.15}$$

The formulation of the hardening evolution equations for each yield surface requires

special attention since it differs significantly from rate-independent multi-yield surface plasticity. I adopt a simple pure kinematic piecewise linear hardening law, following from the Prager's model. In the context of single yield surface plasticity, the evolution of the backstress is expressed as:

$$\dot{\alpha}_{ij} = C\dot{\varepsilon}^{vp}_{ij} \tag{4.16}$$

where C is material parameter that defines the plastic modulus and the direction of translation of a yield surface in the multi-yield approach is shown in Eq. 4.10.

It is important to note that in contrast to rate independent plasticity the stress state does not have to lie within or on the current active yield surface $\hat{m}$ when rate effect is included. For instance, in case of a creep test, where the stress state remains unaltered, all yield surfaces within the active yield surface (i.e., $1 < m \leqslant \hat{m}$) continue to translate with respect to each other until eventually reaching the image stress at t=∞. At the asymptote, all yield surfaces remain tangent to each other.

The hardening translation rule in the multi-yield surface viscoplastic model is formulated from the single yield surface viscoplasticity and the multi-yield surface plasticity approach discussed above.

I adopt a form similar to the Prager's rue to describe the hardening evolution law for the current active yield surface, $\hat{m}$:

$$\dot{\alpha}^{\hat{m}}_{ij} = \hat{C}^{\hat{m}}\mu^{\hat{m}}_{ij} \tag{4.17}$$

in which, $\hat{C}^{\hat{m}}$ denotes the instantaneous plastic modulus associated with the current active yield surface expressed as:

$$\hat{C}^{\hat{m}} = C^{\hat{m}}\mu^{\hat{m}}_{ij}\dot{\varepsilon}^{vp}_{ij} \tag{4.18}$$

where, $C^{\hat{m}}$ is the plastic modulus of the current active yield surface. The instantaneous plastic modulus is scaled by the magnitude of the projection of the slip rate on to the translation direction of the active yield surface. This is analogous to the instantaneous

modulus in case of single yield surface viscoplasticity, where the plastic modulus is scaled with the magnitude of slip rate. The yield surfaces that lie outside the current stress state (i.e., $m > \hat{m}$), the backstress remains instantaneously stationary.

In contrast to the rate independent plasticity, where the inner surfaces remain tangent to the active yield surface, the viscoplastic model does not require the stress state to remain within the yield surfaces. The time dependent translation of the active yield surface and the inner yield surfaces must satisfy the collinearity condition at all times. The evolution of backstress for the inner yield surface are expressed as:

$$\dot{\alpha}_{ij}^{m} = \hat{C}^{\hat{m}} \mu_{ij}^{\hat{m}} \tag{4.19}$$

which implies that all inner yield surfaces translate at the some speed and direction with the current active yield surface.

This restriction guarantees that there is no relative translation among the inner surfaces until the active yield surface $\hat{m}$ reaches the stress point. Fig.4.3 illustrates the hardening evolution processes during the creep test when the active yield surface reaches the stress state (i.e., $f^{\hat{m}} = 0$), the current active yield surface switches to the next yield surface ($\hat{m} \leftarrow \hat{m} - 1$). The reminder of the inner yield surfaces then translate based on the plastic modulus and direction of the new active yield surface.

4.4 Viscoelastic-viscoplastic model for cyclic deformation at high temperature

In this section, a viscoelastic-viscoplastic model is defined to capture the cyclic behavior of metals in high temperature environment. The viscoelastic behavior is modeled based on the Boltzmann integral and Prony series approximation of the time dependent moduli. The viscoplastic behavior is modeled using the multi-yield surface viscoplastic model formulated in Section 4.3. The purpose of the proposed model is to accurately idealize the cyclic response in high temperature environment, where rate dependence of the response is non trivial. The proposed model builds on the viscoelastic-viscoplastic model previously

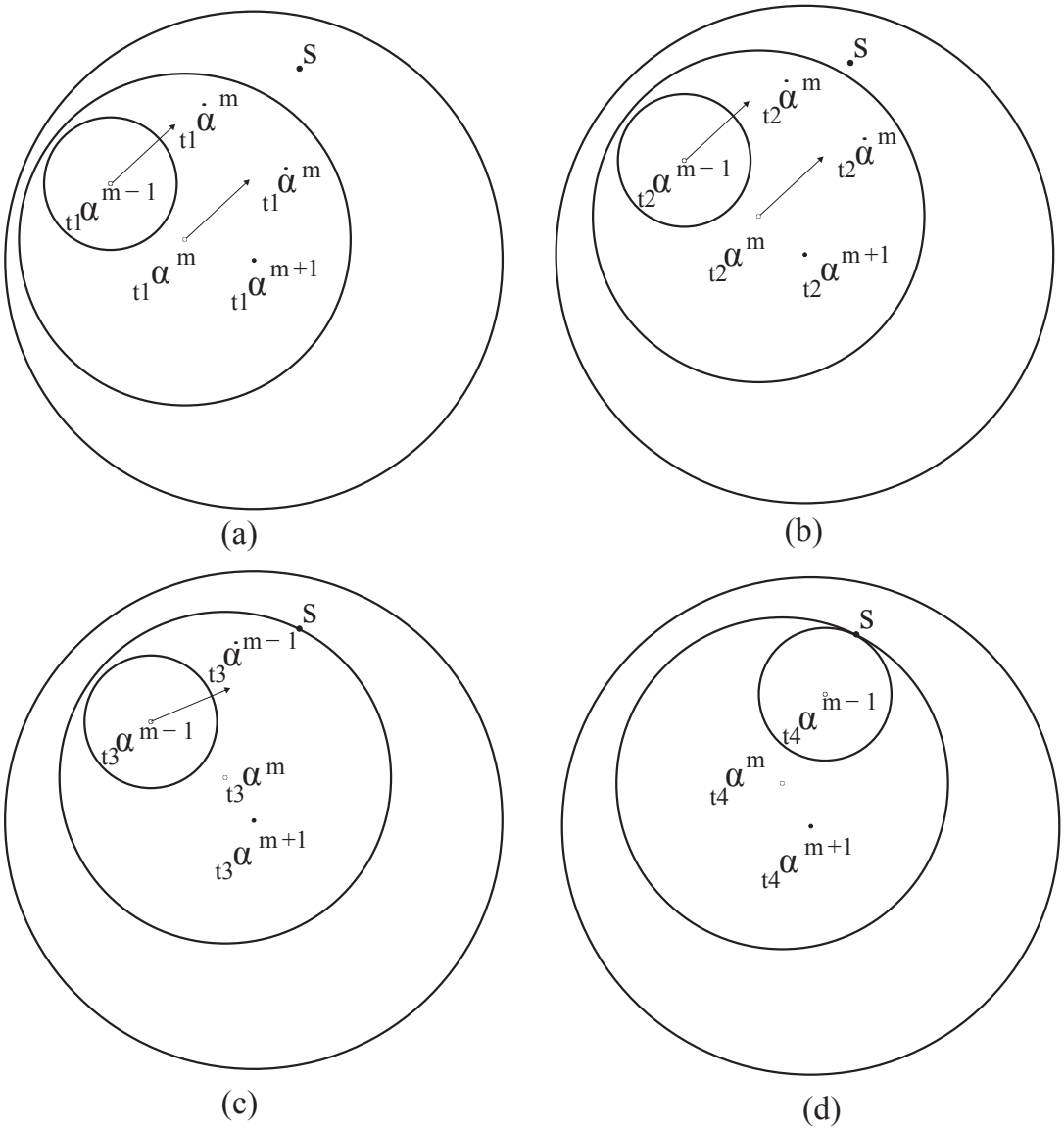

Figure 4.3: Inner yield surface translation process at (a) time t1; (b) time t2; (c) time t3; (d) time t4.

developed by the authors[3, 74], and extends the formulation to describe the cyclic behavior using the multi-yield surface viscoplasticity framework.

The governing equilibrium equations describing the mechanical response of a body occupying the domain $\Omega \subset \mathbb{R}^{n_{\text{sd}}}$ is expressed in the following form:

$$s_{ij,j}(\mathbf{x},t) - p_{,i}(\mathbf{x},t) + b_i(\mathbf{x},t) = 0; \;\; \mathbf{x} \subset \Omega; \;\; t \in [0,t_0] \tag{4.20}$$

where, $\mathbf{b}$ is the body force per unit volume; $\mathbf{s}$ the deviatoric stress tensor; $p = -\text{tr}(\boldsymbol{\sigma})/3$ the pressure; $\boldsymbol{\sigma}$ the stress tensor ($\boldsymbol{\sigma} = \mathbf{s} - p\boldsymbol{\delta}$); $\boldsymbol{\delta}$ the second order identity tensor; and $\text{tr}(\cdot)$ denotes trace. $\mathbf{x}$ and t parameterize the spatial and temporal dimensions, respectively. t_0 is the upper limit of the time domain. Bold symbol indicates vector notation (i.e., $\mathbf{x} = [x_1, x_2, x_3]$ for $n_{\text{sd}} = 3$). The following boundary conditions are prescribed:

$$u_i(\mathbf{x},t) = \bar{u}_i(\mathbf{x},t) \qquad \mathbf{x} \in \Gamma_D, \;\; t \in [0,t_0] \tag{4.21}$$

$$\sigma_{ij} n_j = \bar{t}_i(\mathbf{x},t) \qquad \mathbf{x} \in \Gamma_N, \;\; t \in [0,t_0] \tag{4.22}$$

where, $\mathbf{u}$ denotes the displacement vector field; $\bar{\mathbf{u}}$ is the prescribed displacement along the Dirichlet boundary; $\Gamma_D \subset \Gamma \equiv \partial\Omega$; $\bar{\mathbf{t}}$ the prescribed traction along the Neumann boundary, $\Gamma_N \subset \Gamma$, such that $\Gamma_D \cap \Gamma_N = \emptyset$ and $\Gamma_D \cup \Gamma_N = \Gamma$; and $\mathbf{n}$ is the outer unit normal to the traction boundary.

Assuming small strain kinematics, the total strain tensor, ε, is:

$$\varepsilon_{ij}(\mathbf{x},t) = \frac{1}{2}\left(u_{i,j}(\mathbf{x},t) + u_{j,i}(\mathbf{x},t)\right) \tag{4.23}$$

The adoption of the small strain theory implies that large rotations and large plastic deformations that may be present in some high temperature applications are not included in this study. The total deformation in the viscoelastic-viscoplastic model is separated into three

components:

$$\varepsilon_{ij} = \varepsilon_{ij}^{\mathrm{ve}} + \varepsilon_{ij}^{\mathrm{vp}} + \varepsilon_{ij}^{\mathrm{T}} \tag{4.24}$$

$\varepsilon^{\mathrm{ve}}$, $\varepsilon^{\mathrm{vp}}$ and ε^{T} respectively denote the viscoelastic, viscoplastic and thermal induced strain.

The constitutive relationship between the deviatoric stress and the viscoelastic strain is modeled using the Boltzmann superposition integral in the context of linear viscoelasticity:

$$s_{ij}(t) = \int_0^t L'_{ijkl}(t-\tau)\frac{d\varepsilon_{kl}^{\mathrm{ve}}(\tau)}{d\tau}d\tau \tag{4.25}$$

in which, the spatial dependence of the pertinent fields is suppressed for simplicity. $\mathbf{L}'$ is the time-dependent deviatoric component of the tensor of viscoelastic moduli, taken to be symmetric and positive definite at any time during the deformation process:

$$L'_{ijkl} = L'_{klij} = L'_{jikl} = L'_{ijlk} \tag{4.26}$$

$$\zeta_{ij}L'_{ijkl}\zeta_{kl} \geq \eta\,\zeta_{ij}\zeta_{ij}; \quad \forall\zeta_{ij} = \zeta_{ji}; \quad \eta > 0 \tag{4.27}$$

A convenient time evolution expression for the viscoelastic moduli is the Prony series:

$$L'_{ijkl}(t) = \left[K_e + \sum_{me=1}^{ME} K_{me}\exp\left(-\frac{t}{\xi_{me}}\right)\right]\bar{L}'_{ijkl} \tag{4.28}$$

in which, $\bar{\mathbf{L}}'$ is the initial moduli tensor; ME the number of Maxwell elements incorporated in the Wiechert model; K_e denotes the ratio of equilibrium deviatoric moduli over instantaneous deviatoric moduli; and K_{me} and ξ_{me} are the ratio of deviatoric moduli on me^{th} Maxwell element over instantaneous deviatoric moduli and the time parameters associated with the me^{th} Maxwell element, respectively. Prony series approximation is utilized to generate a component-dependent relaxation. In order to make time independent moduli tensor the instantaneous elastic moduli; i.e., $\bar{\mathbf{L}}' = \mathbf{L}'(t=0)$, the values of the Prony series parameters are constrained such that $K_e + \sum_{me=1}^{M} K_{me} = 1$,

For an isotropic solid, the deviatoric component of the elastic moduli is expressed as:

$$L'_{ijkl}(t) = 2G(t)\left(\delta_{ik}\delta_{jl} - \frac{1}{3}\delta_{ij}\delta_{kl}\right) \tag{4.29}$$

Substituting Eqs. 4.28 and 4.29 into Eq. 4.25, the deviatoric stress tensor is expressed as:

$$s_{ij}(t) = 2\bar{G}K_e\varepsilon_{ij}^{\mathrm{ve}}(t) + 2\bar{G}\sum_{me=1}^{ME} K_{me}\varepsilon_{ij}^{me}(t) \tag{4.30}$$

where,

$$\varepsilon_{ij}^{me}(t) = \int_0^t \exp\left(-\frac{t-\tau}{\xi_{me}}\right)\frac{d\varepsilon_{ij}^{\mathrm{ve}}(\tau)}{d\tau}d\tau \tag{4.31}$$

in which, $\varepsilon^{\mathrm{ve}}$ is the deviatoric component of the viscoelastic strain, and $\bar{G} = G(0)$ the instantaneous shear modulus.

The variation of the relaxation behavior as a function of temperature is modeled using the Williams-Landel-Ferry (WLF) equation. Let a_T denote the WLF time-temperature shift factor expressed in the form:

$$\log a_T(T) = \frac{-C_1(T - T_{\mathrm{ref}})}{C_2 + (T - T_{\mathrm{ref}})} \tag{4.32}$$

where, T denotes temperature; C_1 and C_2 are material constants and T_{ref} is the reference temperature, typically taken to be the room temperature. Provided the relaxation behavior at the reference temperature and the material constants are known, the relaxation behavior at an arbitrary temperature is obtained by shifting the time scale within a master WLF curve using a_T:

$$t = \int_0^\tau \frac{d\xi}{a_T(T(\xi))} \tag{4.33}$$

The thermal strains are taken to be volumetric:

$$\varepsilon_{ij}^{\mathrm{T}} = \alpha(T - T_{\mathrm{ref}})\delta_{ij} \tag{4.34}$$

where, α is the thermal expansion coefficient. The viscoplastic strain is taken to remain in the deviatoric strain space (i.e., $\mathrm{tr}(\varepsilon^{\mathrm{vp}}) = 0$). Considering an isotropic solid with insignificant relaxation under hydrostatic loading, the constitutive relationship for pressure becomes:

$$p(t) = -ku_{i,i}(t) + 3k\left[\alpha\left(T(t) - T_0\right)\right] \tag{4.35}$$

in which, k is the bulk modulus. The viscoplastic behavior of the material is idealized based on the model defined in Section 4.3. The viscoplastic hardening exponent, q, is expressed as a function of the non-dimensional temperature, T^*, as:

$$q(T^*) = q_{\mathrm{ref}} + (\bar{q} - q_{\mathrm{ref}})T^*; \quad T^\star = \frac{T - T_{\mathrm{ref}}}{\bar{T} - T_{\mathrm{ref}}} \tag{4.36}$$

where $q_{\mathrm{ref}} = q(T_{\mathrm{ref}})$ and $\bar{q} = q(\bar{T})$ are exponents evaluated at two temperatures. The temperature dependent yield stress associated with yield surface m is defined as:

$$\sigma_Y^m = \sigma_{Y_{\mathrm{ref}}}\left(\bar{\varepsilon}^{vp^m}\right)\left(1 - (T^\star)^\varsigma\right) \tag{4.37}$$

where $\sigma_{Y_{\mathrm{ref}}}$ is the yield stress evolution with respect to plastic deformation at room temperature; $\bar{\varepsilon}^{vp^m}$ represents the equivalent viscoplastic strain at mth yield surface, and ς is a material parameter.

4.5 Numerical Implementation of the Multi-yield Surface Deformation Model

The solution of the deformation problem is performed based on a staggered solution strategy of isothermal type. In this strategy, the mechanical problem is evaluated until convergence is achieved at each time step. The thermal state of the system is regarded as an input to mechanical solvers. The thermal state of the structure is critical to the cyclic deformation and failure behavior. The transient thermal diffusion, which is not modeled in this chapter, may also be important in certain problems such as in the presence of high rate deformation. All cases in this chapter investigate relatively long term behavior, in which

isothermal conditions prevail (hours to hundreds of hours). The thermal steady state is typically reached in a matter of a few seconds, and therefore the thermal transients do not significantly affect the mechanical process. A detailed formulation of the transport problem and the coupled solution algorithm has been provided in Ref. [36]. In the remainder of this section, a θ rule scheme time discretization is proposed and formulated for the multi-yield surface deformation model.

4.5.1 Mixed FEM formulation of the multi-yield surface deformation model

The system of equations to evaluate the viscoelastic-viscoplastic response of the solid is numerically evaluated based on the mixed finite element method. In this approach, both displacement and pressure fields are taken to be the cardinal unknowns (as opposed to the standard finite element method, where the displacement field is the sole unknown field and stress is computed at quadrature points). The nodal displacement and pressure are simultaneously evaluated as described below.

The weak forms of the governing equations of equilibrium in terms of the deviatoric stress and pressure (i.e., Eqs. 4.20 and 4.35, respectively) are expressed as:

$$\int_{\Omega} v^h_{i,j} s_{ij} d\Omega - \int_{\Omega} v^h_{i,i} p d\Omega - \int_{\Gamma^u_N} v^h_i \bar{t}_i d\Gamma - \int_{\Omega} v^h_i b_i d\Omega = 0 \tag{4.38}$$

$$\int_{\Omega} \frac{1}{k} q^h p^h d\Omega + \int_{\Omega} q^h u^h_{i,i} d\Omega d\Omega = 0 \tag{4.39}$$

where, $\mathbf{v}$ and q are the test functions for displacement and pressure, defined within the appropriate Sobolev spaces and with sufficient smoothness, and Let $\mathbf{v}^h$ and q^h belong to the corresponding finite dimensional subspaces of the test functions, $\mathbf{v}$ and q, respectively. I perform a Bubnov-Galerkin discretization of the displacement and pressure fields, as well

as the corresponding test functions:

$$u_i^h(\mathbf{x},t) = \sum_{a=1}^{n_u} N_a^u(\mathbf{x})\,\hat{u}_{ai}(t) \tag{4.40}$$

$$p^h(\mathbf{x},t) = \sum_{a=1}^{n_p} N_a^p(\mathbf{x})\,\hat{p}_a(t) \tag{4.41}$$

in which, N_a^u and N_a^p are respectively the basis functions of the displacement and pressure fields that correspond to node a; $\hat{(\cdot)}$ denotes the nodal coefficients of the corresponding field; and n_u and n_p are the total number of displacement and pressure nodes, respectively.

Substituting Eqs. 4.40 and 4.41 into Eqs. 4.38 and 4.39, respectively, the discretized equilibrium equations take the form:

$$\Psi_{bi} := \int_\Omega N_{b,j}^u s_{ij} d\Omega - \sum_{c=1}^{n_p} \int_\Omega N_{b,i}^u N_c^p d\Omega \hat{p}_c - \int_{\Gamma_N} N_b^u \bar{t}_i d\Gamma - \int_\Omega N_b^u b_i d\Omega = 0; \quad b = 1,...,n_u \tag{4.42}$$

$$\Theta_c := \sum_{a=1}^{n_p} \int_\Omega \frac{1}{k} N_c^p N_a^p d\Omega \hat{p}_a + \sum_{b=1}^{n_u} \int_\Omega N_c^p N_{b,i}^u d\Omega \hat{u}_{bi} - \int_\Omega 3N_c^p[\alpha(T-T_0)] d\Omega = 0; \quad c = 1,...,n_p \tag{4.43}$$

Taking the time derivative of Eq. 4.30, and employing Eq. 4.31and discretizing in time yields the recurrence formula of the deviatoric stress tensor as:

$$s_{ij} -_t s_{ij} = 2\bar{G}\left(\varepsilon_{ij}^{\mathrm{ve}} -_t \varepsilon_{ij}^{\mathrm{ve}}\right)\bar{K} - 2\bar{G}\sum_{me}^{ME} K_{me}\left(1 - \exp\left(-\frac{\Delta t}{\xi_{me}}\right)\right)_t \varepsilon_{ij}^{me} \tag{4.44}$$

where,

$$\bar{K} = K_e + \sum_{me}^{ME} K_{me}\left(1 - \exp\left(-\frac{\Delta t}{\xi_{me}}\right)\right)\frac{\xi_{me}}{\Delta t} \tag{4.45}$$

I adopt the left subscript indicating the time discretization steps; and the left superscript as the iterative number. Eq. 4.44 indicates that the calculation of the deviatoric stress at current

time step requires the value of ε at the previous time step, only rather than its entire history as Eq. 4.31 implies, significantly reducing the computing and memory requirements.

Consider a one-parameter family discretization of the viscoplastic strain rate in the form:

$$\frac{{}_{t+\Delta t}\varepsilon_{ij}^{\mathrm{vp}} - {}_{t}\varepsilon_{ij}^{\mathrm{vp}}}{\Delta t} = \theta\, {}_{t+\Delta t}\dot{\varepsilon}_{ij}^{\mathrm{vp}} + (1-\theta)\, {}_{t}\dot{\varepsilon}_{ij}^{\mathrm{vp}} \tag{4.46}$$

in which, $\theta \in [0,1]$ is an algorithmic parameter. The choices of $\theta = 0, 1$ and 0.5 correspond to the explicit, implicit and midpoint rules, respectively. Substituting Eqs. 4.24 and 4.40 into Eq. 4.44 and using Eq. 4.46, the discretized form of the constitutive equation for the deviatoric stress is expressed as:

$$\begin{aligned} R_{ij} :=& {}_{t+\Delta t}\, s_{ij} - {}_{t}\, s_{ij} - 2\bar{G}\sum_{a=1}^{n_u} N_{a,j}^{u}(\mathbf{x})\, {}_{t+\Delta t}\hat{u}_{ai}\bar{K} + 2\bar{G}\sum_{a=1}^{n_u} N_{a,j}^{u}(\mathbf{x})\, {}_{t}\hat{u}_{ai}\bar{K} \\ &+ 2\bar{G}\Delta t\,\theta\, {}_{t+\Delta t}\dot{\varepsilon}_{ij}^{\mathrm{vp}}\bar{K} + 2\bar{G}\Delta t\,(1-\theta)\, {}_{t}\dot{\varepsilon}_{ij}^{\mathrm{vp}}\bar{K} + 2\bar{G}\sum_{me}^{ME} K_{me}\left(1-\exp\left(-\frac{\Delta t}{\xi_{me}}\right)\right) {}_{t}\varepsilon_{ij}^{me} \end{aligned} \tag{4.47}$$

Using Eq. 4.17, Eq. 4.19 and Eq. 4.46, the discretized form of the constitutive equation for the backstress of the mth yield surface is expressed as:

$$\begin{aligned} R_{ij}^{m} :=& {}_{t+\Delta t}\,\alpha_{ij}^{m} - {}_{t}\,\alpha_{ij}^{m} - {}_{t+\Delta t}C^{\hat{m}}\Delta t\,\theta\left({}_{t+\Delta t}\mu_{ij}^{\hat{m}}\right)\left({}_{t+\Delta t}\mu_{kl}^{\hat{m}}\right)\left({}_{t+\Delta t}\dot{\varepsilon}_{kl}^{\mathrm{vp}}\right) \\ &- {}_{t}C^{\hat{m}}\Delta t\,(1-\theta)\left({}_{t}\mu_{ij}^{\hat{m}}\right)\left({}_{t}\mu_{kl}^{\hat{m}}\right)\left({}_{t}\dot{\varepsilon}_{ij}^{\mathrm{vp}}\right) \end{aligned} \tag{4.48}$$

Equations 4.42, 4.43, 4.47 and 4.48 together consist of the discretized nonlinear system of the viscoelastic-viscoplastic deformation problem. Newton's method is employed to solve this system of equations [33]. Considering the first order Taylor-series expansion of all four

equations yield:

$$
\begin{aligned}
{}^{k+1}\Psi_{bi} &\approx {}^{k}\Psi_{bi} + {}^{k}\left(\frac{\partial \Psi_{bi}}{\partial s_{kl}}\right)^{k+1}\delta s_{kl} + \sum_{c=1}^{n_p} {}^{k}\left(\frac{\partial \Psi_{bi}}{\partial \hat{p}_c}\right)^{k+1}\delta \hat{p}_c \\
&= {}^{k}\Psi_{bi} + \int_{\Omega} N^u_{b,j}\,{}^{k+1}\delta s_{ij} d\Omega - \sum_{c=1}^{n_p}\int_{\Omega} N^u_{b,i} N^p_c d\Omega\,{}^{k+1}\delta \hat{p}_c = 0
\end{aligned} \tag{4.49}
$$

$$
\begin{aligned}
{}^{k+1}\Theta_c &\approx {}^{k}\Theta_c + \sum_{b=1}^{n_u} {}^{k}\left(\frac{\partial \Theta_c}{\partial \hat{u}_{bk}}\right)^{k+1}\delta \hat{u}_{bk} + \sum_{a=1}^{n_p} {}^{k}\left(\frac{\partial \Theta_c}{\partial \hat{p}_a}\right)^{k+1}\delta \hat{p}_a \\
&= {}^{k}\Theta_c + \sum_{b=1}^{n_u}\int_{\Omega} N^p_c N^u_{b,i} d\Omega\,{}^{k+1}\delta \hat{u}_{bi} + \sum_{a=1}^{n_p}\int_{\Omega} \frac{1}{k} N^p_c N^p_a d\Omega\,{}^{k+1}\delta \hat{p}_a = 0
\end{aligned} \tag{4.50}
$$

$$
\begin{aligned}
{}^{k+1}R_{ij} &\approx {}^{k}R_{ij} + {}^{k}\left(\frac{\partial R_{ij}}{\partial s_{kl}}\right)^{k+1}\delta s_{kl} + \sum_{a=1}^{n_u} {}^{k}\left(\frac{\partial R_{ij}}{\partial \hat{u}_{ak}}\right)^{k+1}\delta \hat{u}_{ak} \\
&= {}^{k}R_{ij} - 2\bar{G}\bar{K}\sum_{a=1}^{n_u} N^u_{a,j}\,{}^{k+1}\delta \hat{u}_{ai} + \left(I_{ijkl} + 2\bar{G}\bar{K}\theta\Delta t\,{}^{k}\bar{C}_{ijkl}\right)^{k+1}\delta s_{kl} = 0
\end{aligned} \tag{4.51}
$$

$$
\begin{aligned}
{}^{k+1}R^m_{ij} &\approx {}^{k}R^m_{ij} + {}^{k}\left(\frac{\partial R^m_{ij}}{\partial \alpha^m_{kl}}\right)^{k+1}\delta \alpha^m_{kl} \\
&= {}^{k}R^m_{ij} + \left(I_{ijkl} - {}^{k}C^m\theta\Delta t\left({}^{k}\mu^{\hat{m}}_{ij}\right)\left({}^{k}\mu^{\hat{m}}_{st}\right){}^{k}\bar{C}^m_{stkl}\right)^{k+1}\delta \alpha^m_{kl} = 0
\end{aligned} \tag{4.52}
$$

in which, the left superscript denotes the Newton iteration count. The Taylor series expansion is performed about the previous iteration, k. $\delta(\cdot)$ denotes the incremental change in the corresponding response field $(\cdot)$ within the Newton iteration. Incorporating Eq.4.14, at each yield surface yields:

$$
\begin{aligned}
{}^{k}\bar{C}^m_{ijkl} &= {}^{k}\left(\frac{\partial \dot{\varepsilon}^{\mathrm{vp}}_{ij}}{\partial \alpha^m_{kl}}\right) \\
&= -\gamma\left\langle \frac{{}^{k}f^m}{{}^{k}\sigma^m_Y}\right\rangle^{q(T^\star)}\left(\frac{\sqrt{3}}{2\left({}^{k}\bar{s}^m\right)}M_{ijkl} + \left(\frac{q(T^\star)}{{}^{k}f^m} - \frac{\sqrt{3}}{3\left({}^{k}\bar{s}^m\right)}\right){}^{k}\left(\frac{\partial f^m}{\partial \sigma_{ij}}\right){}^{k}\left(\frac{\partial f^m}{\partial \sigma_{kl}}\right)\right)
\end{aligned} \tag{4.53}
$$

where:

$$ {}^{k}\bar{C}_{ijkl} = {}^{k}\left(\frac{\partial \dot{\varepsilon}_{ij}^{\mathrm{vp}}}{\partial s_{kl}}\right) = -\sum_{m=1}^{M} {}^{k}\bar{C}_{ijkl}^{m} \tag{4.54} $$

$$ M_{ijkl} = \delta_{ik}\delta_{jl} - \frac{1}{3}\delta_{ij}\delta_{kl} \tag{4.55} $$

The increment of deviatoric stress, ${}^{k+1}\delta s_{ij}$ is evaluated using Eq. 4.51 as:

$$ {}^{k+1}\delta s_{ij} = {}^{k}Q_{ijkl}\left(2\bar{G}\bar{K}\sum_{a=1}^{n_u} N_{a,l}^{u}\,{}^{k+1}\delta\hat{u}_{ak} - {}^{k}R_{kl}\right) \tag{4.56} $$

where, the modulus ${}^{k}\mathbf{Q}$ is defined as:

$$ {}^{k}Q_{ijkl} = \left(I_{ijkl} + 2\bar{G}\bar{K}\theta\Delta t\,{}^{k}\bar{C}_{ijkl}\right)^{-1} \tag{4.57} $$

The increment of backstress, ${}^{k+1}\delta\alpha_{ij}^{m}$ is evaluated using Eq. 4.52 as:

$$ {}^{k+1}\delta\alpha_{ij}^{m} = -{}^{k}Q_{ijkl}^{m}\,{}^{k}R_{kl}^{m} \tag{4.58} $$

where, the modulus ${}^{k}\mathbf{Q}^{m}$ is defined as:

$$ {}^{k}Q_{ijkl}^{m} = \left(I_{ijkl} - {}^{k}C^{m}\theta\Delta t\,\left({}^{k}\mu_{ij}^{\hat{m}}\right)\left({}^{k}\mu_{st}^{\hat{m}}\right){}^{k}\bar{C}_{stkl}^{m}\right)^{-1} \tag{4.59} $$

Substituting Eq. 4.56 into Eqs. 4.49 and 4.50 yield:

$$ \int_{\Omega} 2\bar{G}\bar{K}\,{}^{k}Q_{ijkl}N_{b,j}^{u}\sum_{a=1}^{n_u} N_{a,l}^{u}d\Omega\,{}^{k+1}\delta\hat{u}_{ak} - \sum_{c=1}^{n_p}\int_{\Omega} N_{b,i}^{u}N_{c}^{p}d\Omega\,{}^{k+1}\delta\hat{p}_{c} = \int_{\Omega} {}^{k}Q_{ijkl}N_{b,j}^{u}\,{}^{k}R_{kl}d\Omega - {}^{k}\Psi_{bi} \tag{4.60} $$

and,

$$ -\sum_{b=1}^{n_u}\int_{\Omega} N_{c}^{p}N_{b,i}^{u}d\Omega\,{}^{k+1}\delta\hat{u}_{bi} - \sum_{a=1}^{n_p}\int_{\Omega}\frac{1}{k}N_{c}^{p}N_{a}^{p}d\Omega\,{}^{k+1}\delta\hat{p}_{a} = {}^{k}\Theta_{c} \tag{4.61} $$

Equations 4.60 and 4.61 are simultaneously evaluated for the increments of the displacement (${}^{k+1}\delta\hat{\mathbf{u}}$) and pressure fields (${}^{k+1}\delta\hat{\mathbf{p}}$) at the current iteration, $k+1$.

When expressed in the matrix form, Eqs. 4.60 and 4.61 yield:

$$\begin{bmatrix} {}^{k}\mathbf{K}^{uu} & \mathbf{K}^{up} \\ (\mathbf{K}^{up})^{T} & \mathbf{K}^{pp} \end{bmatrix} \begin{Bmatrix} {}^{k+1}\delta\hat{\mathbf{u}} \\ {}^{k+1}\delta\hat{\mathbf{p}} \end{Bmatrix} = \begin{Bmatrix} {}^{k}\mathbf{f}^{u} \\ {}^{k}\mathbf{f}^{p} \end{Bmatrix} \tag{4.62}$$

in which, the components of the tangent stiffness matrix are expressed as:

$$\begin{aligned} {}^{k}K^{uu}_{\alpha\beta} &= \int_{\Omega} 2\bar{G}\bar{K}^{k} Q_{ijmn} N^{u}_{b,j} \sum_{a=1}^{n_u} N^{u}_{a,n} d\Omega; \alpha = b + (i-1)\, n_u; \beta = a + (m-1)\, n_u & (4.63)\\ K^{up}_{\alpha c} &= -\int_{\Omega} N^{u}_{b,i} N^{p}_{c} d\Omega; \quad \alpha = a + (i-1)\, n_u; \quad 1 \le c \le n_p & (4.64)\\ K^{pp}_{ab} &= -\int_{\Omega} \frac{1}{k} N^{p}_{a} N^{p}_{b} d\Omega; \quad 1 \le a, b \le n_p & (4.65) \end{aligned}$$

The left superscript is included only on the sub matrix, $\mathbf{K}^{uu}$, which is the only nonlinear part of the tangent stiffness matrix. The unknown displacement and pressure coefficients, as well as the force vectors are expressed in the vector form as:

$$\begin{aligned} {}^{k+1}\delta\hat{\mathbf{u}} &= \{{}^{k+1}\hat{u}_1, ..., {}^{k+1}\hat{u}_{n_{\mathrm{sd}} \times n_{\mathrm{u}}}\}^{T}; \quad {}^{k}\mathbf{f}^{u} = \{{}^{k}f^{u}_{1}, ..., {}^{k}f^{u}_{n_{\mathrm{sd}} \times n_{\mathrm{u}}}\}^{T} & (4.66)\\ {}^{k+1}\delta\hat{\mathbf{p}} &= \{{}^{k+1}\hat{p}_1, ..., {}^{k}\hat{p}_{n_p}\}^{T}; \qquad {}^{k}\mathbf{f}^{p} = \{{}^{k}f^{p}_{1}, ..., {}^{k}f^{p}_{n_p}\}^{T} & (4.67) \end{aligned}$$

and the components of the force vector are given as:

$$\begin{aligned} {}^{k}f^{u}_{\alpha} &= \int_{\Omega} {}^{k}Q_{ijkl} N^{u}_{b,j} {}^{k}R_{kl} d\Omega - {}^{k}\Psi_{bi}; \quad \alpha = b + (i-1)\, n_u & (4.68)\\ {}^{k}f^{p}_{a} &= {}^{k}\Theta_{a}; \quad 1 \le a \le n_p & (4.69) \end{aligned}$$

The finite elements discretizing the displacements and the pressure fields are chosen in order to satisfy the Babuska-Brezzi constraint. Ensuring this constraint is satisfied in the choice of the pressure and displacement discretization to avoid the potential numerical

instability and response oscillations observed in mixed formulations. In the numerical studies provided in this chapter, I employ nine-node biquadratic in displacement and four-node bilinear in pressure Taylor-Hood element.

4.5.2 Implementation algorithm of the multi-yield surface deformation model

Based on the expressions above, I employ the following algorithm to compute the pressure and displacement fields:

At arbitrary time $t+\Delta t$: Given the state at the previous time step; ${}_t\hat{\mathbf{u}}$, ${}_t\hat{\mathbf{p}}$, ${}_t\mathbf{s}$, ${}_t\alpha$, ${}_t\dot{\varepsilon}^{\text{vp}}$ and ${}_t\dot{\varepsilon}^{\text{vp}}_m$; Find the response at the current step; $\hat{\mathbf{u}}$, $\hat{\mathbf{p}}$.

1. Initiate the algorithm: $k=0$.

2. Set the initial guesses for the pressure and deformation coefficients at the current increment:

$$ {}^0\hat{\mathbf{u}} = {}_t\hat{\mathbf{u}}; \quad {}^0\hat{\mathbf{p}} = {}_t\hat{\mathbf{p}}; \quad {}^0\mathbf{s} = {}_t\mathbf{s}; \quad {}^0\alpha_m = {}_t\alpha_m; \quad {}^0\dot{\varepsilon}^{\text{vp}} = {}_t\dot{\varepsilon}^{\text{vp}}; \quad {}^0\dot{\varepsilon}^{\text{vp}}_m = {}_t\dot{\varepsilon}^{\text{vp}}_m \tag{4.70} $$

3. Loop until convergence:

   (a) Compute the moduli: $\bar{K}$, ${}^k\bar{\mathbf{C}}$, ${}^k\mathbf{Q}$, ${}^k\bar{\mathbf{C}}^{\mathbf{m}}$ and ${}^k\mathbf{Q}^m$ using Eqs. 4.45, 4.54, 4.57, 4.53 and 4.59, respectively.

   (b) Calculate ${}^k\mathbf{\Psi}$, ${}^k\mathbf{\Theta}$, ${}^k\mathbf{R}$ and ${}^k\mathbf{R}^m$ using Eqs. 4.42, 4.43, 4.47 and 4.48, respectively.

   (c) Update the pressure and displacement increments, ${}^{k+1}\delta\hat{\mathbf{u}}$ and ${}^{k+1}\delta\hat{\mathbf{p}}$ by solving the linear system in Eq. 4.62.

   (d) Compute deviatoric stress increment ${}^{k+1}\delta\mathbf{s}$ and backstress increment ${}^{k+1}\delta\alpha_m$ at each integration point using Eq. 4.56 and Eq. 4.58.

(e) Update displacement, pressure, deviatoric stress and backstress:

$$^{k+1}\hat{\mathbf{u}} = {}^{k+1}\delta\hat{\mathbf{u}} + {}^{k}\hat{\mathbf{u}} \tag{4.71}$$

$$^{k+1}\hat{\mathbf{p}} = {}^{k+1}\delta\hat{\mathbf{p}} + {}^{k}\hat{\mathbf{p}} \tag{4.72}$$

$$^{k+1}\mathbf{s} = {}^{k+1}\delta\mathbf{s} + {}^{k}\mathbf{s} \tag{4.73}$$

$$^{k+1}\alpha^{m} = {}^{k+1}\delta\alpha^{m} + {}^{k}\alpha^{m} \tag{4.74}$$

(f) Update viscoplastic strain rate $^{k+1}\dot{\varepsilon}^{\mathrm{vp}}$ using Eqs. 4.14.

(g) Update viscoplastic strain $^{k+1}\varepsilon^{\mathrm{vp}}$ by evaluating:

$$^{k+1}\varepsilon^{\mathrm{vp}} = {}_{t}\varepsilon^{\mathrm{vp}} + \theta\Delta t\,{}^{k+1}\dot{\varepsilon}^{\mathrm{vp}} + (1-\theta)\Delta t\,{}_{t}\dot{\varepsilon}^{\mathrm{vp}} \tag{4.75}$$

(h) Update yield surface translation direction $^{k+1}\boldsymbol{\mu}^{m}$ using Eqs. 4.10.

(i) $k = k+1$

4.6 Numerical Investigations

The proposed computational model is employed to investigate the cyclic mechanical response of a titanium alloy at elevated temperatures. The alloy of the interest Ti-6Al-2Sn-4Zr-2Mo-0.1Si (Ti-6242S) displays good mechanical properties at elevated temperature, making it a candidate structural material for hypersonic aircraft applications. The present investigations start with the verification of the multi-yield surface viscoplastic model (Section 4.6.1), where a parametric study is conducted to investigate the effectiveness of the proposed theory in ensuring that the collinearity rule is strictly enforced. The second part is the calibration and simulation of the cyclic response of Ti-6242S in low cycle fatigue test (Section 4.6.2), where the Prager's linear kinematic hardening modulus, the number of yield surfaces and the yield stress associated with each surface are evaluated.

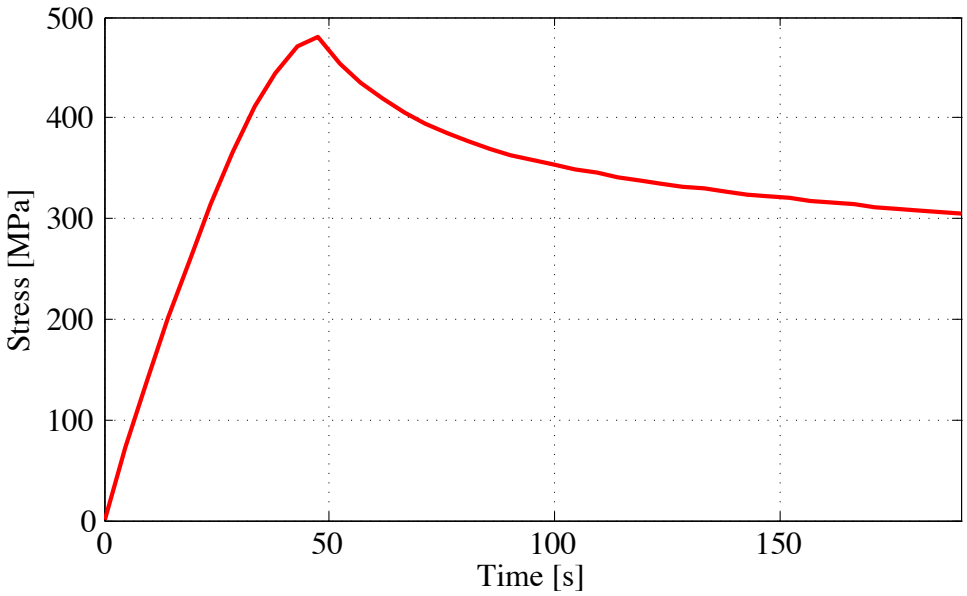

Figure 4.4: Stress relaxation test.

4.6.1 Multi-yield surface viscoplasticity verification

In order to verify the theory, a parametric study is performed by testing the viscoplastic response and the collinearity theory with given random stress variation input. Figure 4.4 shows the relaxation behavior under the constant strain magnitude of 3.5%. At the early stage of stress relaxation, both viscoelastic and viscoplastic relaxation processes are active since the specimens were loaded to stress levels beyond several yield surfaces. The long-term relaxation behavior is governed by the viscoelastic component of the model only, as the stress drops inside the first yield surface.

The test stress input history of the collinearity test is shown in Fig.4.5, where σ_{11} is monotonically increased to 1000 MPa in 40 s then gradually reduced to zero until 72 s. σ_{22} remains null in the first 40 s then linearly increase to -1000 MPa until 72 s. For comparison purpose, two sets of simulations are run in order to test the effectiveness of the proposed model. The first simulation is executed without the incorporated direction correction term; therefore the backstress evolution in each yield surface follows Prager's linear kinematic hardening in the uniaxial case as:

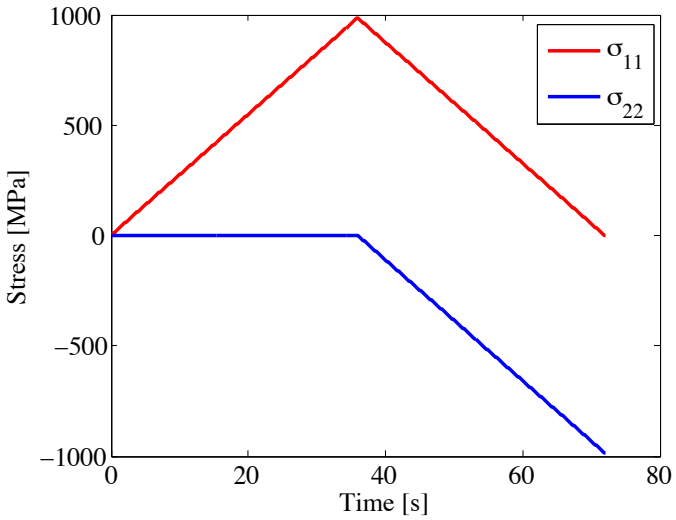

Figure 4.5: Time history input of stress tensor.

$$\dot{\alpha}_{ij}^{\hat{m}} = C^{\hat{m}} \dot{\varepsilon}_{ij}^{vp} \tag{4.76}$$

The second simulation follows the proposed theory in Eq.4.17. The simulation outcome of the parametric test is summarized in Fig.4.6, where 7 yield surfaces are employed and 3 snapshots are taken from the yield stress translation process at the beginning of test, at 40 s when the uniaxial loading ends and at 72 s when the simulation stops. All the yield surfaces are concentric circles in the beginning of test, when no loads are applied. At the end of the uniaxial test, both simulations yield unanimous outcomes as shown in (b) and (e) in Fig.4.6, implying the collinearity of the backstress of each yield surface and the stress tensor in uniaxial test. As the stress tensor deviates after time 40 s, the collinearity nature needs to be maintained by the proposed yield surface translation theory, therefore in (c) of Fig.4.6, clearly some non-smooth intersection occurs within several interior yield surfaces; however the proposed theory eliminate the intersection as shown in (f) of Fig.4.6 .

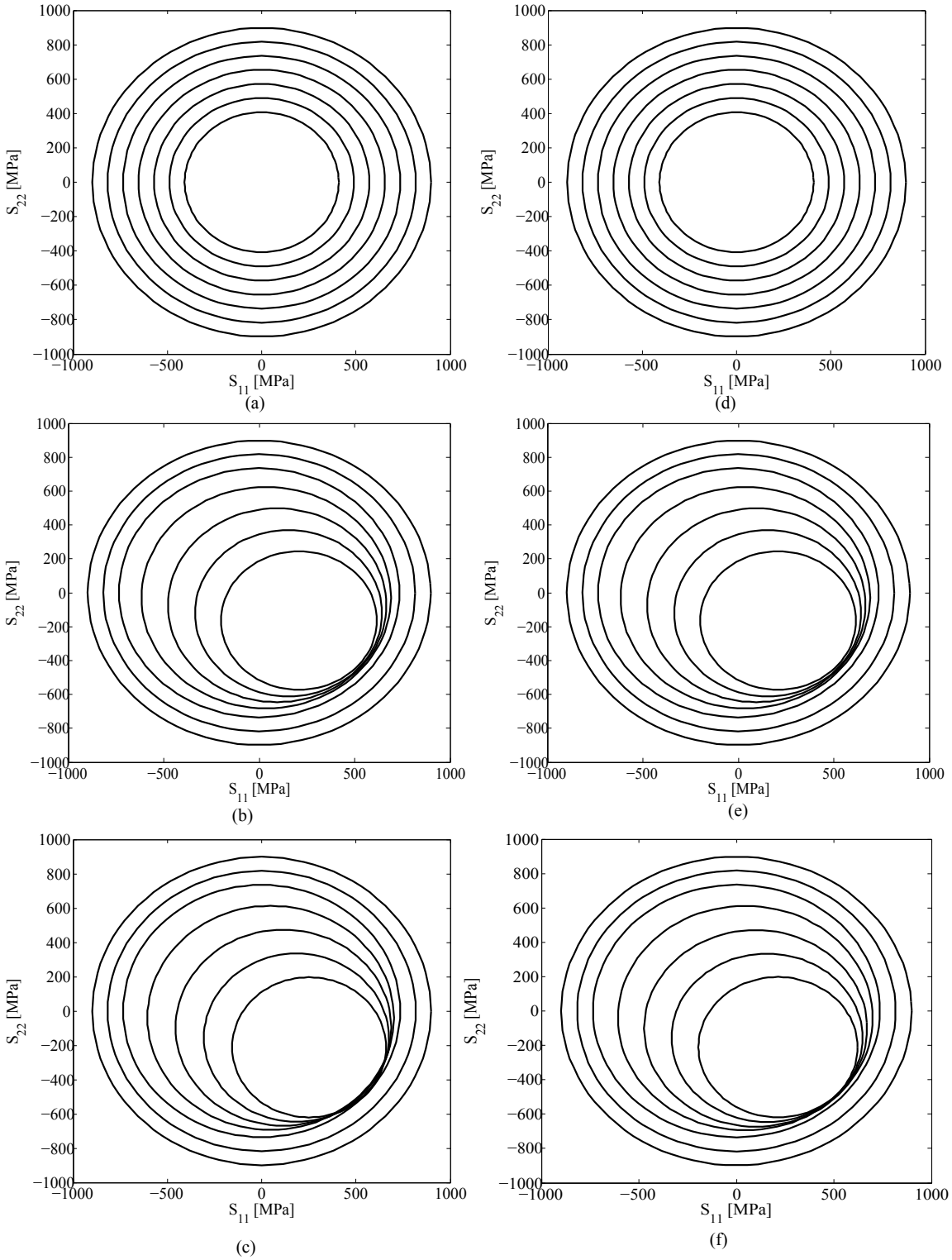

Figure 4.6: Yield surface translation process of no corrected translation direction at time (a) 0; (b) 40 s; (c) 72 s; of corrected translation direction at time (d) 0; (e) 40 s; (f) 72 s.

4.6.2 Cyclic response of Ti-6242S alloy

The cyclic responses of Ti-6242S cyclic tests are performed based on the experimental data conducted at the Air Force Research Laboratory. The test specimen is a round bar with a cross section diameter 0.25 in and a gauge length 1 inch. The uniaxial experiments were displacement controlled with a strain range 0.012 and constant strain rate $1.0e^{-3}$ 1/s. Two tests were performed at high temperature environment 450 ^{0}C with a strain ratio -1 and 550 ^{0}C with a strain ratio -∞. The plastic moduli are more linear in the low temperature environment and generally require less number of yield surfaces. In the current study 6 yield surfaces are employed to generate favorable results compared to the experiments. The outmost yield surface is set to be enormous enough so that the stress point won't be able to jump beyond it.

The simulation results at 450 ^{0}C as well as the comparison between the experiments are summarized in Fig. 4.7. The near identical strain input of experiment and simulation are shown in (a), where 2 cycles are modeled from the start of the test. The strain ratio of -1 makes this test a symmetric cyclic response. The simulation stress output is presented in (b), which generates a good match with respect to the experimental data. For the initially undamaged material all the yield surfaces (1,2...M) are concentric and share the same origin. The pure kinematic hardening law and the constant temperature determine that all the surfaces will translate in the deviatoric stress space without changing size and orientation. The simulated viscoplastic strain rate history is demonstrated in (c), where each jump of the viscoplastic strain rate magnitude is a direct consequence of the activation of one more yield surface, as shown in Eq.4.14. The comparison of the simulated initial hysteresis loop of stress strain curve and stress plastic strain curve are demonstrated in (d). The applied 0.6% strain generates an approximate 2.5 % plastic strain. It can be seen that the stress, viscoplastic strain rate and stress strain hysteresis loop all deliver the symmetric distribution due to the strain controlled input history.

The comparison of the initial experimental and simulation hysteresis loop of stress

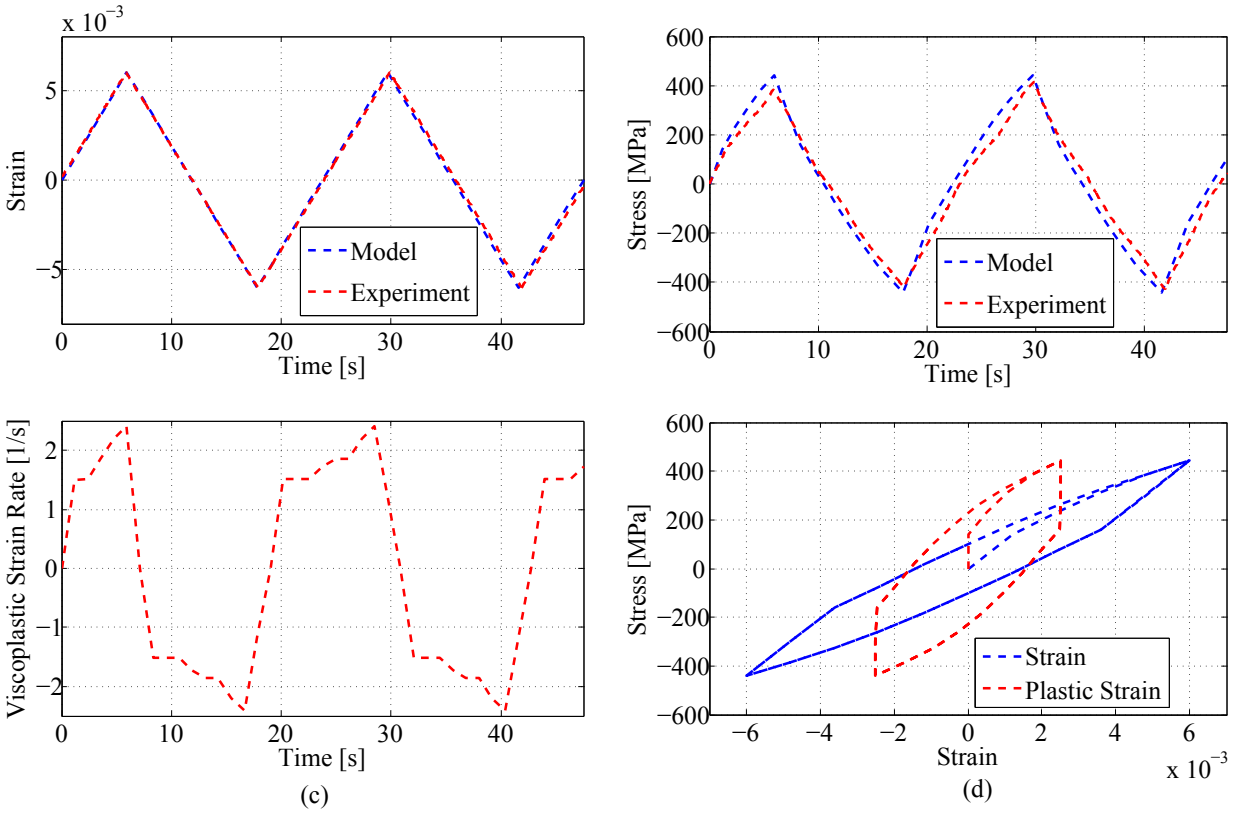

Figure 4.7: Strain controlled low cycle fatigue test at 450 ^{0}C of (a) simulation and experiment strain input history comparison; (b) simulation and experiment stress history comparison; (c) simulation viscoplastic strainrate history; (d) simulation stress vs. strain and stress vs. plastic strain comparison.

strain curve is presented in Fig. 4.8. It is convenient to generate a piecewise linear elasoplastic behavior through the multi-yield function viscoplastic model, and for 450 ^{0}C the activation of 3 yield surfaces gives good match to the experimental data. The other material parameters of Ti-6242S, Young's modulus, Poisson's ratio, viscoplastic parameters and viscoelastic parameters are all calibrated and validated in the previous work [74]. Since this is a uniaxial test, the deviatoric stress point moves back and forth along one direction, and the yield surface translation direction is coincident with the Prager's linear hardening law. As the test starts, the stress point moves from the origin. The plot is determined by the elastic moduli before the stress point reach the first yield surface. Next, the yield surface will be towed along the moving direction of the stress point, and the loading function Eq. 4.1 of the first yield surface can be a positive value depending on the viscosity. Here the slope of the stress strain curve is determined by the C_1 in Eq. 4.18. As the stress point moves beyond the second yield surface, both first and second yield surfaces are translating, with the rate calculated by C_2 in Eq. 4.18 of the second yield surface. In the unloading process, the stress point reverses the moving direction. Plastic unloading can occur in highly rate dependent materials, however it is trivial in the Ti-6242S up to 550 ^{0}C. It is noticeable that the strain distance of elastic deformation, plastic deformation of first yield surface translation and so on of unloading curve are all twice as large as the initial loading curve, this can also be observed from (c) and (d) of Fig.4.7. As a symmetric displacement controlled test, the two-stress peak also has equal magnitude and the hysteresis loop converges very fast.

Fig. 4.9 shows the simulation results at 550 ^{0}C. The strain input of experiment and simulation are shown in (a), where 2 cycles are modeled from the start of the test. The strain range is the same as the test in 450 ^{0}C but with a different ratio -∞ make this test a nonsymmetrical cyclic response. The simulation stress output is presented in (b), which shows more nonlinearity due to the higher temperature. The simulated viscoplastic strain rate history is presented in (c). It can be seen that the peak value reduces after the initial loading, which shows that it take longer time to converge in more rate dependent tests. The

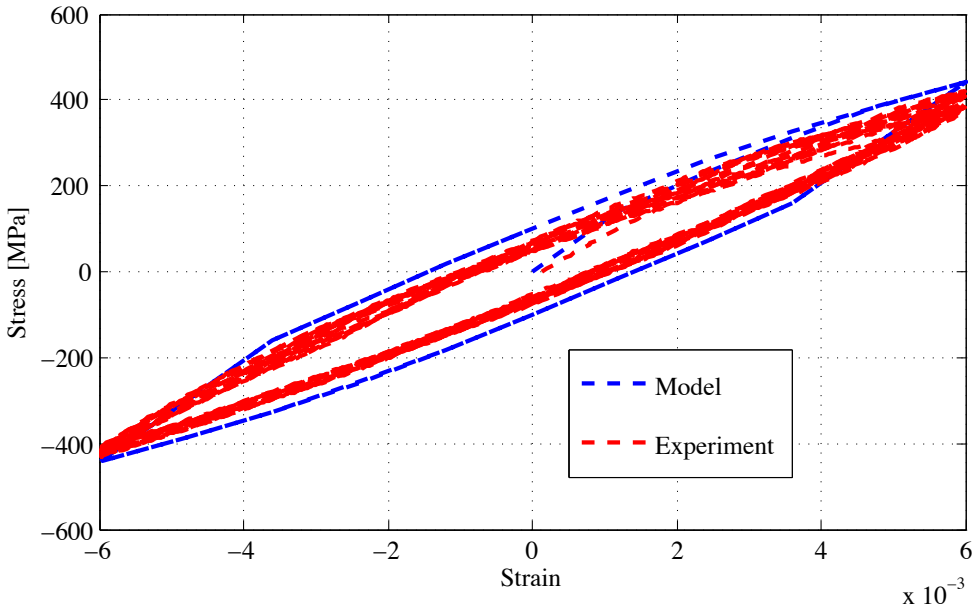

Figure 4.8: Strain controlled low cycle fatigue test at 450 ^{0}C of simulation and experiment stress vs. strain comparison.

comparison of the simulated initial hysteresis loop of stress strain curve and stress plastic strain curve are demonstrated in (d). The applied 0.6% strain also generates an approximate 2.5 % plastic strain. Eventually the stress, viscoplastic strain rate and stress strain hysteresis loop are all shifted toward the compression direction due to the given strain ratio.

The comparison of the initial experimental and simulation hysteresis loop of stress strain curve is presented in Fig. 4.10. It is clear that more yield surfaces needs to be activated for 550 ^{0}C in order to generate good match to the experimental data due to the highly nonlinear experimental curve. In this test, smaller yield surfaces are expected in high temperature and smaller values of C_m are introduced in the outer yield surfaces due to the little hardening around the peak value of the stress. The converged hysteresis loop deviates away from the initial path as a result of the asymmetry in the applied displacement, which also leads to the different peak magnitude of the stress value.

sectionConclusion

This chapter provided a multi-yield surface viscoplastic model to study the cyclic response of alloys in high temperature environment, from which the time dependent effect has

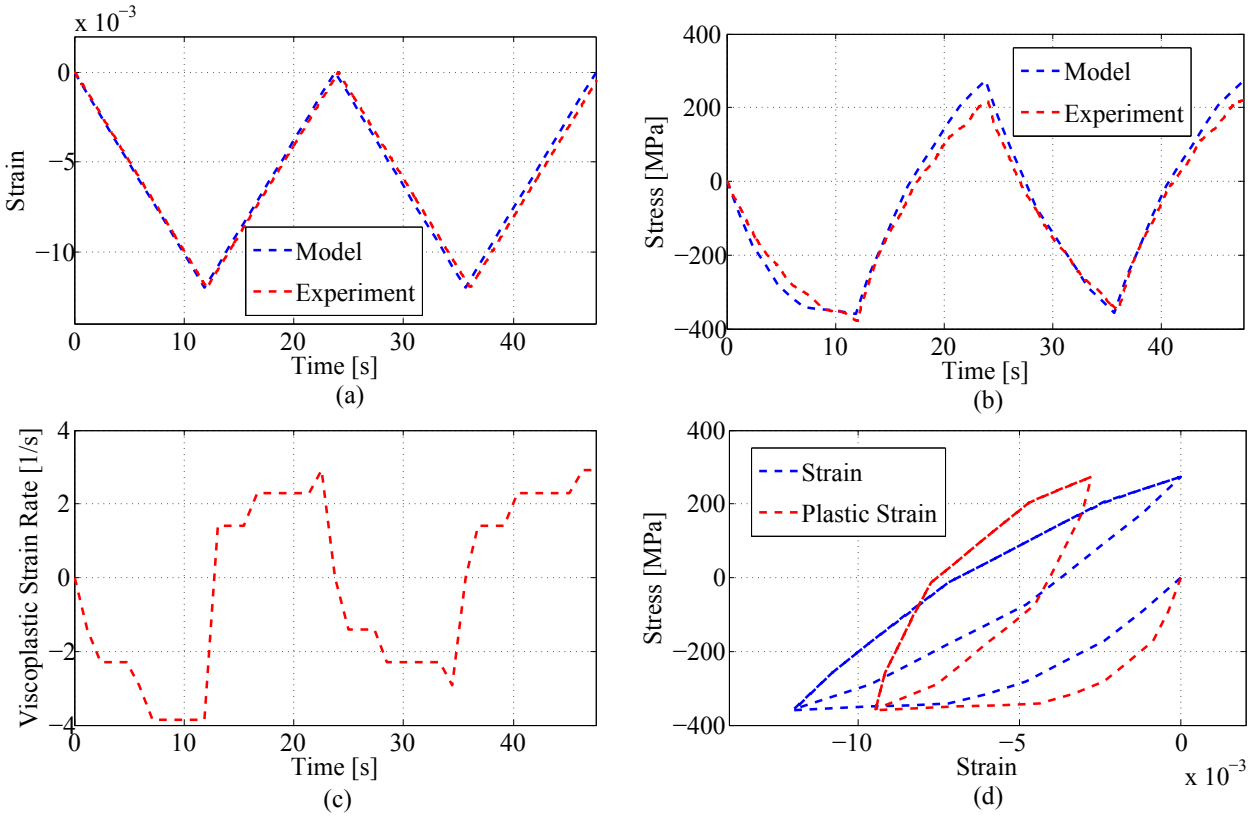

Figure 4.9: Strain controlled low cycle fatigue test at 550 ^{0}C of (a) simulation and experiment strain input history comparison; (b) simulation and experiment stress history comparison; (c) simulation viscoplastic strainrate history; (d) simulation stress vs. strain and stress vs. plastic strain comparison.

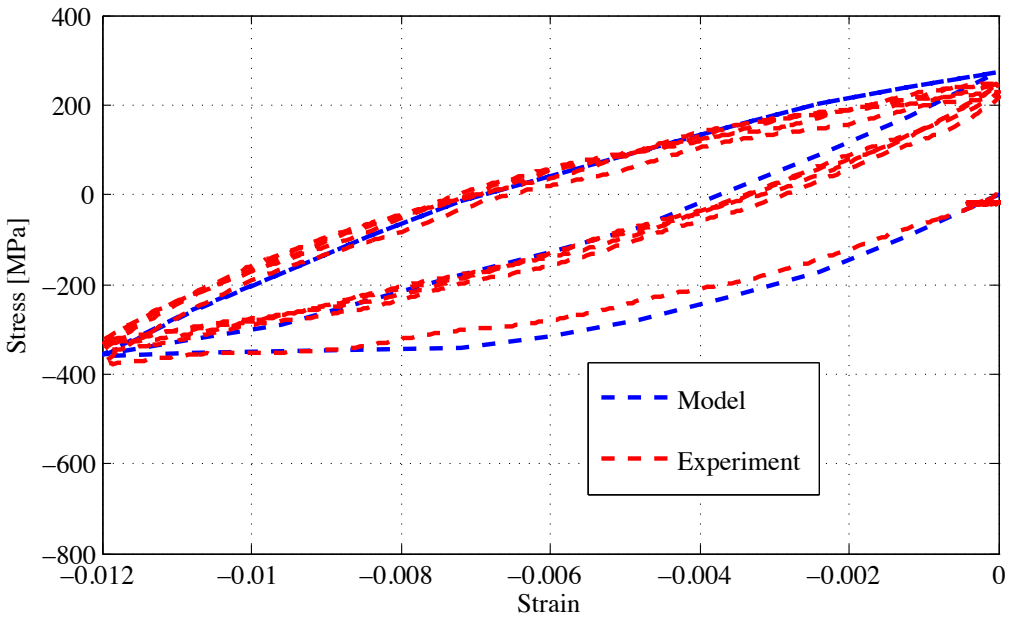

Figure 4.10: Strain controlled low cycle fatigue test at 550 ^{0}C of simulation and experiment stress vs. strain comparison.

been addressed on the backstress evolution and the Mroz assumption of collinearity rule. The computational model was verified in a parametric study and then calibrated against experiments conducted in a variety of temperatures of Ti-6242S. The proposed computational model accurately eliminates the non-smooth intersection of yield surfaces in viscoplastic regime and generates a good match of the hysteresis curve compared to the experiments.

Improvements remain to be investigated in the proposed model. One main issue is the oxygen ingress of the titanium alloy at elevated temperatures, which will affect the cyclic response as oxygen concentration increases. As a result of the embrittlement and hardening effect of the transport of oxygen[74], the yield surfaces will increase in the proposed model, which brings in the isotropic hardening component into the multi-yield surface viscoplastic model. Another challenge is the accurate characterization of localized deformation and failure that necessitates resolution of the grain scale deformation and transport processes within the boundary region, which needs multiscale computational models that can accurately incorporate such grain scale information into a structural scale problem[77].

Chapter 5

CONCLUSION AND FUTURE WORK

5.1 Conclusion

This dissertation provided a three-field computational model for coupled transport-deformation problems. The proposed model is based on a tightly coupled two-field formulation for the viscoplastic deformation response to provide accurate pressure and pressure gradient fields to a transport problem. The proposed computational model conveniently and accurately computes these fields based on the mixed finite element approach. The detailed accomplishments of this dissertation are summarized as follows.

Chapter 2 provided a three-field computational model for the evaluation of coupled transport-deformation problems. The displacement, pressure and concentration fields are evaluated as independent unknowns. The key novel contribution of the present chapter is the demonstration that the mixed finite element method, in which the pressure is treated as an independent unknown in addition to the displacement degrees of freedom, can be employed to accurately compute the pressure gradient in the deformation problem. The pressure gradient information, in turn, is employed to accurately calculate the instantaneous coefficients of the advection-reaction terms of the mass transport problem. In addition, the computational model has the following properties: (a) the mass transport problem is stabilized to accurately describe the advection-dominated transport in the presence of high stress gradients (e.g., crack and notch tips); (b) the deformation problem is evaluated using a tight-coupled two-field (displacement-pressure) formulation, whereas the transport and deformation processes are evaluated based on a staggered approach to efficiently address problems where the time scales associated with the transport and deformation processes are disparate.

Chapter 3 proposed a new coupled deformation-transport model to study the response of titanium alloys at combined environments. The proposed approach was built to account for creep and relaxation processes, which are critical to the response characterization at high temperatures. The computational model was validated against experiments conducted in combined environments. The two main novel contributions of this chapter are: (1) The proposed model accurately captures the time-dependent creep/relaxation processes through the incorporation of viscoelastic-viscoplastic mechanisms; (2) A detailed investigation of the coupling mechanisms between the oxygen ingress induced embrittlement, relaxation and the inelastic deformation is provided, including partial validation of the interaction mechanisms based on experimental data.

Chapter 4 presented a multi-yield surface viscoplastic model to study the cyclic response of alloys. The proposed approach was built to realize the rate dependent cyclic behavior of alloys in the high temperature environment. The main contribution of this chapter is to extend the multi-yield surface plasticity model to viscoplastic regime, from which the time dependence effect has to be addressed on the back stress evolution and the Mroz assumption of collinearity rule. A nonlinear stress-strain response kinematic hardening model is introduced by incorporating linear kinematic hardening and multi-yield surface plasticity, which avoids the recall terms in dynamic and static recovery and significantly simplifies the mathematical implementation of the viscoplastic kinematic hardening.

5.2 Future work

Beyond the achievement and contribution of the proposed model in this dissertation, several challenges remain. First, transport problem needs to be coupled with the multi-yield surface viscoplastic model. With the variation of oxygen concentration, the isotropic hardening term will complicate the process of the back stress evolution and viscoplastic strain rate evaluation. Second, substantial amount of researches show that during the exposure of titanium alloy in the extreme environment, a ceramic oxide layer will develop

on the surface of the structure[15], which exhibits significantly higher solubility of oxygen than the titanium alloy. Therefore, the existing transport model needs to be improved to incorporate the variability of diffusivity with respect to the local oxygen concentration, which will makes the transport model another non-linear problem. Furthermore, a multi-scale computational approach that can accurately characterize the localization deformation and failure is required to consummate the model.

BIBLIOGRAPHY

[1] www.timet.com.

[2] www.darpa.mil.

[3] C. Oskay and M. Haney. Computational modeling of titanium structures subjected to thermo-chemo-mechanical environment. *Int. J. Solids Structures*, 47:3341–3351, 2010.

[4] G.G. Eichholz. Tritium penetration through concrete. Technical report, Georgia Institute of Technology, 1988.

[5] C. Sun, J. Chen, J. Zhu, M Zhang, and J. Ye. A new diffusion model of sulfate ions in concrete. *Constr build mater*, 39:39–45, 2013.

[6] A. Krishnan and C. Oskay. Modeling compression-after-impact response of polymer matrix composites subjected to seawater aging. *J. Compos. Mater*, 46:2851–2861, 2012.

[7] H. Wipf. Solubility and diffusion of hydrogen in pure metals and alloys. *Physica Scripta*, T94:43–51, 2001.

[8] T. Ericsson. Review of oxidation effects on cyclic life at elevated temperature. *Can. Metall. Quart.*, 18:177–195, 1979.

[9] R. A. Oriani, J. P. Hirth, and M. Smialowski. *Hydrogen Degradation of Ferrous Alloys*. William Andrew Publishing/Noyes, 1985.

[10] B. Zuchowski. Predictive capability for hypersonic structural response and life prediction, phase 1 identification of knowledge gaps. technical report afrl-rb-wp-tr-2010-3069. Technical report, Air Force Research Laboratory, 2010.

[11] B. Zuchowski. Predictive capability for hypersonic structural response and life prediction: Phase ii - detailed design of hypersonic cruise vehicle hot-structure. technical report afrl-rq-wp-tr-2012- 0280. Technical report, Air Force Research Laboratory, 2012.

[12] W. J. Boettinger, M. E. Williams, S. R. Coriell, U. R. Kattner, and B. A. Mueller. Alpha case thickness modeling in investment castings. *Metall. Mater. Trans. B*, 31B:1419–1427, 2000.

[13] K. S. Chan, M. Koike, B. W. Johnson, and T. Okabe. Modeling of alpha-case formation and its effects on the mechanical properties of titanium alloy castings. *Metall. Mater. Trans. A*, 39:171–180, 2008.

[14] R. G. Keanini, G. K. Watkins, T. Okabe, and M. Koike. Theoretical study of alpha case formation during titanium casting. *Metall. Mater. Trans. B*, 38:729–732, 2007.

[15] R. N. Shenoy, J. Unnam, and R. K. Clark. Oxidation and embrittlement of ti-6al-2sn-4zr-2mo alloy. *Oxidation of metals*, 26, 1986.

[16] P. Sofronis and R. M. McMeeking. Numerical analysis of hydrogen transport near a blunting crack tip. *J. Mech. Phys. Solids*, 37:317–350, 1989.

[17] A. H. M. Krom, R. W. J. Koers, and A. Bakker. Hydrogen transport near a blunting crack tip. *J. Mech. Phys. Solids*, 47:971–992, 1999.

[18] P. W. M. Peters, J. Hemptenmacher, and C. Todd. Oxidation and stress enhanced oxidation of ti-6-2-4-2. In *Ti-2003 science and technology*, 2003.

[19] T. A. Parthasarathy, W. J. Porter, S. Boone, R. John, and P. Martin. Life prediction under tension of titanium alloys that develop an oxygenated brittle case during use. *Scripta Materialia*, 65:420–423, 2011.

[20] A. L. Pilchak, W. J. Porter, and R. John. Room temperature fracture processes of a near-α titanium alloy following elevated temperature exposure. *J. Mater. Sci.*, 47:7235–7253, 2102.

[21] Z. Liu and G. Welsch. Literature survey on diffusivities of oxygen, aluminum and vanadium in alpha titanium, beta titanium, and in rutile. *Metall. Trans. A*, 19:1121–1125, 1988.

[22] B. Sefer. *Oxidation and alpha-case phenomena in titanium alloys used in aerospace industry: Ti-6Al-2Sn-4Zr-2Mo and Ti-6Al-4V.* PhD thesis, Lule University of Technology, 2014.

[23] M. J. Donachie. *Titanium: A Technical Guide*. ASM International, 2nd edition, 2000.

[24] C. Leyens and M. Peters. *Titanium and Titanium Alloys*. Wiley-VCH, 2003.

[25] S. Ndong-Mefane, H. Kanayama, and M. F. Ogino, M. El-Amin. A stabilization method for the hydrogen diffusion model in materials. *J. Comput. Sci. Technol.*, 2:447–458, 2008.

[26] Li, Oriani, and Darken. Thermodynamics of stressed solids. *Zeitschrift fur physikalische chemie-frankfurt*, 49:271, 1966.

[27] A. L. Ruoff and R. W. Balluffi. On strain enhanced diffusion in metals. iii. Interpretation of recent experiments. *J. Appl. Phys.*, 34:2862–2872, 1963.

[28] Salganik. Transport processes in bodies with a large number of cracks. *Mekhan. Tverd. Tela*, 27:1534–1538, 1974.

[29] Krajcinovic, Basista, Mallick, and Sumarac. Chemo-micromechanics of brittle solids. *J. Mech. Phys. Solids*, 40:965–990, 1992.

[30] S. Kirkpatrick. Percolation and conduction. *Rev. Mod. Phys.*, 45:574–588, 1973.

[31] L. P. Franca, H. Guillermo, and A. Masud. Revisiting stabilized finite element methods for the advective–diffusive equation. *Comput. Methods Appl. Mech. Engrg.*, 195:1560–1572, 2006.

[32] L. P. Franca, S. L. Frey, and T. J. R. Hughes. Stabilized finite element methods: I. Application to the advective-diffusive model. *Comp. Methods Appl. Mech. Engrg.*, 95:253–276, 1992.

[33] H. P. Langtangen. *Computational Partial Differential Equations: Numerical Methods and Diffpack Programming*. Springer, 2003.

[34] T. J. R. Hughes, W. K. Liu, and A. Brooks. Finite element analysis of incompressible viscous flows by the penalty function formulation. *J. Comput. Phys.*, 30:1–60, 1979.

[35] C. Oskay. Variational multiscale enrichment for modeling coupled mechano-diffusion problems. *Int. J. Numer. Meth. Engng.*, 89:686–705, 2012.

[36] H. Yan and C. Oskay. A three-field (displacement-pressure-concentration) formulation for couled transport-deformation problems. *Finite Elem. Anal. Des.*, 90:20–30, 2014.

[37] J.L. Chaboche. Thermodynamic formulation of constitutive equations and application to the viscoplasticity and viscoelasticity of metals and polymers. *Int. J. Solids Struct.*, 34:2239–2254, 1997.

[38] R. M. Hinterhoelzl and R. A. Schapery. Fem implementation of a three-dimensional viscoelastic constitutive model for particulate composites with damage growth. *Mechanics of time-dependant materials*, 8:65–94, 2004.

[39] J. L. Shannon Jr. *Aerospace Structural Metals Handbook*. Ti-6242., 1978.

[40] K. S. McReynolds. A study on alpha case depth in Ti-6Al-2Sn-4Zr-2Mo. Technical

report, Technical Report AFRL-RX-WP-TP-2011-4294, Air Force Research Laboratory, 2011.

[41] C. Leyens, M. Peters, D. Weinem, and W. A. Kaysser. Influence of long-term annealing on tensile properties and fracture of near α titanium alloy Ti-6Al-2.75Sn-4Zr-0.4Mo-0.45Si. *Metall. Mater. Trans. A*, 27A:1709–1717, 1996.

[42] K. V. S. Srinadh and V. Singh. Oxidation behaviour of the near α-titanium alloy IMI 834. *Bull. Mater. Sci.*, 27:347–354, 2004.

[43] S. Yamanaka, H. Ogawa, and M. Miyake. Effect of interstitial oxygen on hydrogen solubility in titanium, zirconium and hafnium. *J. Less-Common Metals*, 172-174:85–94, 1991.

[44] S. Arbabi and M. Sahimi. Mechanics of disordered solids. I. Percolation of elastic networks with central forces. *Phys. Rev. B*, 47:695–702, 1993.

[45] C. D. Lorenz, R. May, and R. M. Ziff. Similarity of percolation thresholds on the HCP and FCC lattices. *J. Stat. Phys.*, 98:961–970, 2000.

[46] B. Moran T. B. Belytschko, W. K. Liu and K. I. Elkhodary. *Nonlinear Finite Elements for Continua and Structures*. Wiley, 2014.

[47] J. Fish and C. Oskay. A nonlocal multiscale fatigue model. *Mech. Adv. Materials and Structures*, 12:485–500, 2005.

[48] C. McAuliffe and H. Waisman. Mesh insensitive formulation for initiation and growth of shear bands using mixed finite elements. *Comp. Mech.*, 51:807–823, 2013.

[49] L. Sanavia H. W. Zhang and B. A. Shrefler. An internal length scale in dynamic strain localization of multiphase porous media. *Mech. Cohes.-Frict. Mat.*, 4:443–460, 1999.

[50] J. Hutchinson and Z. Suo. Mixed mode cracking in layered materials. *Adv. Appl. Mech.*, 29:63–191, 1992.

[51] E. Olsson M. D. Thouless and A. Gupta. Cracking of brittle films on elastic substrates. *Acta Materialia*, 40:1287–1292, 1992.

[52] C. Oskay. Variational multiscale enrichment method with mixed boundary conditions for modeling diffusion and deformation problems. *Comput. Methods Appl. Mech. Engrg.*, 264:178–190, 2013.

[53] D. L. McDowell. A two surface model for transient nonproportional cyclic plasticity. *J. Appl. Mech.*, 52:298–308, 1985.

[54] J. L. Chaboche and G. Rousselier. On the plastic and viscoplastic constitutive equations, parts i and parts ii. *Int. J. Pressure Vessel Piping*, 105:153–158, 1983.

[55] J. Lemaitre, A. Benallal, and D. Marquis. Lifetime prediction of structures in anisothermal viscoplasticity coupled to damage. *Nuclear Engineering and Design*, 133:345–360, 1992.

[56] E. Busso and F. McClintock. A dislocation mechanics-based crystallographic model of a b2-type intermetallic alloy. *Int. J. Plasticity*, 12:1–28, 1996.

[57] B. Klusemann and D. Kochmann. Microstructural pattern formation in finite-deformation single-slip crystal plasticity under cyclic loaload: relaxation vs. gradient plasticity. *Comp. Methods Appl. Mech. Engrg.*, 278:765–793, 2014.

[58] L. Li, L. Shen, and G. Proust. Fatigue crack initiation life prediction for aluminum alloy 7075 using crystal plasticity finite element simulations. *Mech. Mater.*, 81:84–93, 2015.

[59] W. Prager. Recent develdevelop in the mathematical theory of plasticity. *J. Appl. Phys.*, 20:235–241, 1949.

[60] P. J. Armstrong and C. O. Frederick. A mathmatical representation of the multiaxial

bauschinger effect. report rd/b/n731, cegb, central electricity generating board. Technical report, Berkeley, UK, 1966.

[61] O. Watanabe and S. N. Atluri. Constitutive modeling of cyclic plasticity and creep, using an internal time concept. *Int. J. Plasticity*, 2:107–134, 1986.

[62] Z. Mroz. On the description of anisotropic workhardening. *J. Mech. Phys. Solids*, 15:163–175, 1967.

[63] J. Prevost. Plasticity theory for soil stres-strain behavior. *J.Eng.Mech.Div*, 104:1177–1194, 1978.

[64] J. Prevost. Constitutive equations for soil media. *Proceedings NATO advanced study institute on numerical methods in geomechanics*, pages 79–102, 1981.

[65] J. Prevost. A simple plasticity theory for frictional cohesionless soil. *Soil. Dyn. Earthq. Eng.*, 4:9–17, 1985.

[66] A. Elgamal, Z. Yang, E. Parra, and A. Ragheb. Modeling of cyclic mobility in saturated cohesion soils. *Int. J. Plasticity*, 19:883–905, 2003.

[67] Q. Gu, J. P. Conte, A. Elgamal, and Z. Yang. Finite element response sensitivity analysis of multi-yield-surface j2 plasticity model by direct differentiation method. *Comp. Methods Appl. Mech. Engrg.*, 198:2272–2285, 2009.

[68] Y. F. Dafalias and E. P. Popov. Plastic internal variables formalism of cyclic plasticity. *J. Appl. Mech.*, 98:645, 1976.

[69] F. Ellyin. An anisotropic hardening rule for elastoplastic solids based on experimental observations. *J.*, 56:499–507, 1989.

[70] R. D. Krieg. A practical two-surface plasticity theory. *J. Appl. Mech.*, 42:641–646, 1975.

[71] J. C. Moonsbrugger and D. L. McDowell. A rate-dependent bounding surface model with a gerneralized image point for nonproportional cyclic plasticity. *J. Mech. Phys. Solids*, 38:627, 1990.

[72] N. Ohno and Y. Kachi. A constitutive model of cyclic plasticity for nonlinear hardening materials. *J. Appl. Mech.*, 53:395–403, 1986.

[73] J. C. Simo. Algorithm for static and dynamic multiplicative plasticity that preserve the classical return mapping schemes of the infinitesimal theory. *Comp. Methods Appl. Mech. Engrg.*, 99:61–112, 1992.

[74] H. Yan and C. Oskay. A viscoelastic-viscoplastic model of titanium structures subjected to thermo-chemo-mechanical environment. *Int. J. Solids Structures*, 56-57:29–42, 2015.

[75] T. H. Lehmann. Some remarks on a general class of yield conditions for large elastoplastic deformation. *Ing. Arch.*, 41:297–310, 1972.

[76] J. L. Chaboche. A review of some plasticity and viscoplasticity constitutive theories. *Int. J. Plasticity*, 24:1642–1693, 2008.

[77] S. Zhang and C. Oskay. Variational multiscale enrichment method with mixed boundary conditions for elasto-viscoplastic problems. *Comput. Mech.*, in press, 2015.